

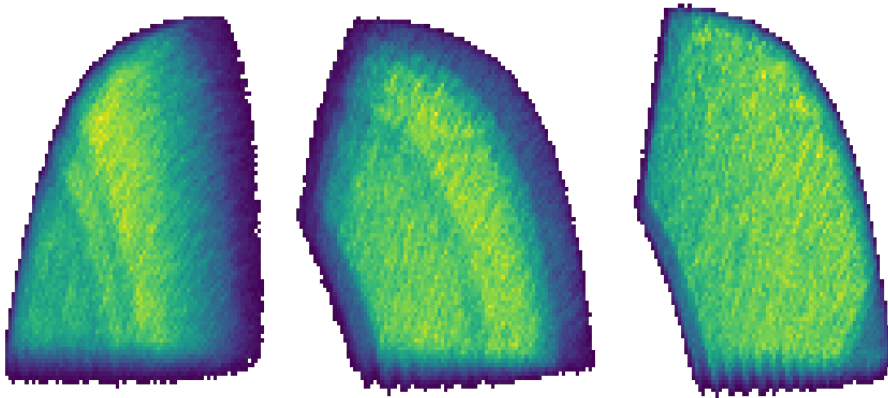
---

# Experimental study of $^{10}\text{Li}$ with low energy (d,p) reactions

Jesper Halkjær Jensen

---

---



PhD Dissertation

Department of Physics and Astronomy  
Aarhus University  
Denmark

Jesper Halkjær Jensen  
Department of Physics and Astronomy  
Aarhus University  
Ny Munkegade 120, Building 1520  
8000 Aarhus C  
Denmark

Cover image is an adaption of Figure 13.5,  
and shows the acceptance region from the three  
experiments covered in the thesis.

© Jesper Halkjær Jensen 2019  
Revision f79dc05 dated 2019-10-25.

# Experimental study of $^{10}\text{Li}$ with low energy (d,p) reactions

A Dissertation Presented to the  
Faculty of Science and Technology of Aarhus University  
in Partial Fulfillment of the Requirements  
for the PhD Degree

by  
Jesper Halkjær Jensen  
August 2019



---

# Contents

<b>Contents</b>	<b>i</b>
<b>Abstract</b>	<b>v</b>
<b>Resumé</b>	<b>vii</b>
<b>Acknowledgments</b>	<b>ix</b>
<b>List of Publications</b>	<b>xi</b>
<b>1 Introduction</b>	<b>1</b>
1.1 Nuclear structure . . . . .	2
1.2 Models . . . . .	4
1.3 Reactions . . . . .	6
1.4 Exotic nuclei . . . . .	7
1.5 $^{10}\text{Li}$ and $^{11}\text{Li}$ . . . . .	8
1.6 Experimental approach . . . . .	13
1.7 The timeline and structure of thesis . . . . .	14
<b>2 Kinematics</b>	<b>17</b>
2.1 Two-body kinematics . . . . .	18
2.2 Kinematic compression . . . . .	19
<b>3 Experimental technique</b>	<b>25</b>
3.1 ISOLDE . . . . .	27

3.2	Detectors . . . . .	30
3.3	$\Delta E - E$ telescope . . . . .	31
<b>4</b>	<b>Beam diagnostics</b>	<b>35</b>
4.1	Old method . . . . .	36
4.2	New method . . . . .	36
4.3	Angle determination . . . . .	37
4.4	Setup and simulation . . . . .	38
4.5	Analysis . . . . .	39
4.6	Conclusion . . . . .	52
<b>5</b>	<b>AUSALib</b>	<b>55</b>
5.1	Geometry . . . . .	55
5.2	Energy loss . . . . .	58
5.3	Analysis pipeline . . . . .	59
<b>6</b>	<b>Data acquisition</b>	<b>65</b>
6.1	Triggers and acquisition control . . . . .	66
6.2	Analogue chain . . . . .	68
6.3	Readout . . . . .	69
6.4	Multicrate . . . . .	70
6.5	Dead time ratio . . . . .	71
6.6	Pulsed beam . . . . .	74
6.7	Backend . . . . .	75
6.8	DaqC . . . . .	77
6.9	RunDB . . . . .	79
6.10	Real time monitoring . . . . .	79
6.11	Future upgrades . . . . .	81
<b>7</b>	<b>IS367</b>	<b>83</b>
7.1	Experimental conditions . . . . .	83
7.2	Data analysis . . . . .	84
7.3	Intensity . . . . .	89

<b>8 IS561A</b>	<b>95</b>
8.1 Setup . . . . .	96
8.2 Calibration and beam properties . . . . .	98
8.3 Data analysis . . . . .	102
<b>9 IS561C</b>	<b>107</b>
9.1 Setup . . . . .	108
9.2 Deuteron target . . . . .	108
9.3 Tritium target . . . . .	111
<b>10 Acceptance</b>	<b>121</b>
10.1 Differential cross section . . . . .	121
10.2 Monte Carlo . . . . .	123
10.3 Rutherford estimation . . . . .	125
<b>11 Scattering theory</b>	<b>129</b>
11.1 General scattering . . . . .	129
11.2 Optical potential . . . . .	132
11.3 Coupled-channels method . . . . .	133
11.4 CDCC . . . . .	135
<b>12 Population of <math>^{10}\text{Li}</math></b>	<b>139</b>
12.1 Structure of $^{10}\text{Li}$ . . . . .	139
12.2 Transfer reaction . . . . .	141
12.3 Alternative reaction mechanisms . . . . .	142
<b>13 Results</b>	<b>145</b>
13.1 Elastic scattering . . . . .	145
13.2 Neutron transfer to $^{10}\text{Li}$ . . . . .	154
<b>14 Summary and outlook</b>	<b>169</b>
14.1 Upgrades to the experimental setup . . . . .	170
14.2 Better intensity measurements . . . . .	171
14.3 Final words . . . . .	172

<b>Abbreviations</b>	<b>173</b>
<b>Bibliography</b>	<b>175</b>



---

# Abstract

In this thesis, I present the results from three experiments studying the structure of  $^{10}\text{Li}$  through neutron transfer reactions at different beam energies. All three experiments were performed at the ISOLDE facility at CERN with a radioactive  $^9\text{Li}$  beam impinging on deuterated plastic. The results of the elastic channels are compared with OM and CDCC calculations. The result of the neutron transfer reactions is compared with CDCC calculations using a novel structure model of  $^{10}\text{Li}$ .

The first experiment was carried out at 2.68 MeV/A in 2005 and give evidence for the existence of a virtual  $s_{1/2}$  state in  $^{10}\text{Li}$ . Furthermore, it confirms the position of a  $p_{1/2}$  resonance close to 0.5 MeV. Coincidences between protons and  $^9\text{Li}$ , from the break up of  $^9\text{Li}$ , provides evidence for a sequential reaction model, however, the applied model can not account for the magnitude of the measured cross sections.

In the second and third experiment at 6.72 MeV/A and 8.0 MeV/A, respectively, there are indications for a higher-lying  $d_{5/2}$  resonance, however, this result is more speculative. The model also struggles to reproduce the absolute cross sections at these energies.

Besides the results from the experiments, I present some of the technical methods that have been used and developed during the experiments and data analysis. This includes the data acquisition system and a general-purpose library for experiments with silicon detectors, **AUSALib**.

Moreover, the kinematic considerations that go into both the design and the analysis phase are discussed. Two techniques to determine beam properties are discussed. One is based on coincidences and mainly discussed

through simulations whereas the other is based on only the ejectile of a two-body reaction. A Monte Carlo method for transforming measurements into absolute cross sections presented as well.

---

# Resumé

I denne afhandling, præsenterer jeg resultaterne fra tre eksperimenter, med formål at studere strukturen af  $^{10}\text{Li}$  gennem neutron-transfer reaktioner ved forskellige energier. Alle tre eksperimenter blev gennemført ved ISOLDE-faciliteten på CERN, ved at kolliderer radioaktive  $^9\text{Li}$ -kerner med et deutereret plastikfolie. Resultaterne fra de elastiske stød er efterfølgende sammenlignet med OM og CDCC beregninger. Resultatet fra neutron-transfer-reaktionerne bliver sammenlignet med CDCC-beregninger, der inkluderer en model for  $^{10}\text{Li}$ .

Det første eksperiment blev gennemført ved 2.68 MeV/A i 2005 og gav evidens for en virtuel  $s_{1/2}$ -tilstand i  $^{10}\text{Li}$ . Desuden bekræftede det positionen af en  $p_{1/2}$ -resonans tæt på 0.5 MeV. Koincidenser mellem protoner og  $^9\text{Li}$  fra opbruddet af  $^{10}\text{Li}$  giver ydermere evidens for en sekventiel reaktionsmekanisme. Den anvendte model kan dog ikke forklare størrelsen af det målte tværsnit.

I det andet og tredje eksperiment ved henholdsvis 6.72 MeV/A og 8.0 MeV/A, er der indikationer for en højtliggende  $d_{5/2}$ -resonans. Dette resultat er dog mere spekulativt. Modellen har også problemer med at reproducere tværsnittets størrelsesorden ved disse energier.

Ud over de tre eksperimenter, præsenterer jeg de tekniske metoder der blev brugt og udviklet i og under både eksperimenterne og dataanalysen. Dette inkluderer bl.a. dataopsamling og analysesoftware.

Desuden bliver de kinematiske overvejelser, der er vigtige for både design af eksperimenterne samt den efterfølgende analyse, diskuteret. To teknikker til at beregne egenskaberne ved den indkommende fordeling af  $^9\text{Li}$  bliver

desuden præsenteret. Den ene er baseret på koincidenser, hvorimod den anden er baseret på detektionen af enkelte lette reaktionsprodukter. Sidst præsenteres en Monte-Carlo-metode til at transformere de eksperimentielle data til absolutte tværsnit.

---

# Acknowledgments

First and foremost, I would like to thank my supervisor Karsten Riisager and my de facto co-supervisor Hans Fynbo. Your impressive knowledge and passion for nuclear physics have been a great inspiration. In particular, I would like to thank Karsten for always keeping your door open for a quick answer or a lengthy discussion, something I have greatly appreciated.

It has been a great pleasure to work in the subatomic group and I would, therefore, like to thank Michael Munch, Oliver Kirsebom, Jacob Johansen, Andreas Gad and Jonas Refsgaard for a strong collegial community.

I will, in particular, like to thank Michael for teaching me a lot about software and data acquisition as well as helping me with the technical aspects of the experiments. For the data acquisition, I also owe Håkon Johansson thanks for being helpful and cooperative.

Thanks to ISOLDE operators, the MAGISOL collaboration and in particular Olof Tengblad and Angel Perea for making the experiments possible. Also thanks to the theoretical help from Antonio M. Moro and Mario Gómez Ramos I got while visiting them.

I would also like to thank Jeppe Christiansen, Jonatan Midtgaard, Søren Møller and Niels Jakob Søe Loft for memorable lunch discussions, dinner nights and proofreading of parts of this thesis.

Lastly, a big thank to my friends and family for being very supportive while patiently listening to details about lithium-isotopes.

*Jesper Halkjær Jensen,  
Aarhus, October 25, 2019.*



---

# List of Publications

The following paper form part of this thesis

1. M. Munch, **J. H. Jensen**, B. Löher, H. Törnqvist and H. T. Johansson *VME readout at and below the conversion time limit*. IEEE Transactions on Nuclear Science, 66, 2 (2019), p. 575-584, DOI: 10.1109/TNS.2018.2884979

Other papers not included in this thesis

1. J. J. W. H. Sørensen, M. K. Pedersen, M. Munch, P. Haikka, **J. H. Jensen**, T. Planke, M. G. Andreasen, M. Gajdacz, K. Mølmer, A. Lieberoth and J. F. Sherson *Exploring the quantum speed limit with computer games*. Nature, 532(7598) (2016), p. 210–213. DOI: 10.1038/nature17620 ARXIV: 1506.09091
2. O. S. Kirsebom, O. Tengblad, R. Lica, M. Munch, K. Riisager, H. O. U. Fynbo, M. J. G. Borge, M. Madurga, I. Marroquin, A. N. Andreyev, T. A. Berry, E. R. Christensen, P. D. Fernández, D. T. Doherty, P. Van Duppen, L. M. Fraile, M. C. Gallardo, P. T. Greenlees, L. J. Harkness-Brennan, N. Hubbard, M. Huyse, **J. H. Jensen**, H. Johansson, B. Jonson, D. S. Judson, J. Konki, I. Lazarus, M. V. Lund, N. Marginean, R. Marginean, A. Perea, C. Mihai, A. Negret, R. D. Page, V. Pucknell, P. Rahkila, O. Sorlin, C. Sotty, J. A. Swartz, H. B. Sørensen, H. Törnqvist, V. Vedia, N. Warr and H. De Witte *First Accurate Normalization of the  $\beta$ -delayed  $\alpha$  Decay of  $^{16}\text{N}$  and Implications*

- for the  $^{12}\text{C}(\alpha, \gamma)^{16}\text{O}$  Astrophysical Reaction Rate. *Physical Review Letters* 121, 142701 (2018). DOI: 10.1103/PhysRevLett.121.142701
3. O. S. Kirsebom I. Alonso T. Berry M. J. G. Borge E. R. Christensen D. Doherty P. Fernandez M. Flores H. O. U. Fynbo M. Gallardo N. Hubbard **J. H. Jensen** H. Johansson B. Jonson R. Lica M. V. Lund A. Martines M. K. Munch K. Riisager O. Sorlin J. A. Swartz O. Tengblad V. Vedia *Improved experimental determination of the branching ratio for  $\beta$ -delayed  $\alpha$  decay of  $^{16}\text{N}$* . EPJ Web Conf. 165 01031 (2017). DOI: 10.1051/epjconf/201716501031
  4. M.V. Lund M.J.G. Borge J.A. Briz J. Cederkäll H.O.U. Fynbo **J.H. Jensen** B. Jonson K.L. Laursen T. Nilsson A. Perea V. Pesudo K. Riisager O. Tengblad *Systematic trends in beta-delayed particle emitting nuclei: The case of  $\beta p \alpha$  emission from  $^{21}\text{Mg}$* . *Physics Letters B*, 750, (2015) p. 356-359. DOI: 10.1016/j.physletb.2015.09.044
  5. M. V. Lund M. J. G. Borge J. A. Briz J. Cederkäll H. O. U. Fynbo **J. H. Jensen** B. Jonson K. L. Laursen T. Nilsson A. Perea V. Pesudo K. Riisager O. Tengblad *Beta-delayed proton emission from  $^{21}\text{Mg}$* . *Eur. Phys. J. A* 51 113 (2015). DOI: 10.1140/epja/i2015-15113-1



---

# Introduction

The field of nuclear physics has researched the atomic nucleus for more than a century. The current understanding is a deceptively simple model, where the atomic nucleus consists of neutrons and protons, which in turn are made up of three fundamental quarks. After a century of research, we can describe a large number of different nuclei, that is different configurations of neutrons and protons, with remarkable accuracy. This does, however, not mean that we have established a simple set of equations that describes all aspects of every atomic nucleus we may stumble upon. At least not at the level of practical usage.

The discovery of the Higgs boson[1, 2] completed the very successful Standard Model, which describes the fundamental particles and their interactions, including the quarks. Since the nucleus is made up of multiple quarks (we need three quarks for each nucleon) and the interaction is governed by three out of the four natural forces, a direct application of the Standard Model is simply too difficult for most nuclei. Instead, we must rely on different models to describe different aspects of the nuclear structure.

Nuclear physics is in that sense still a field in motion. New aspects keep appearing as we study more and more nuclei and our current models can not always account for these. Whether we one day will crack the code and develop a set of equations to describe the nucleus as elegantly as Maxwell's equations describe electromagnetism is hard to say.

The knowledge of atomic nuclei has nonetheless important ramifications. Medicine and energy production have in particular benefitted from our understanding of radioactivity and nuclear reactions. A lot of nuclear

research is, however, basic science and does not have direct applications. Instead, it leads us to a deeper understanding of nature, which both have an inherent value and may very well be applicable in the future.

This thesis will investigate a particular set of nuclei, namely neutron-rich Li isotopes. They serve as a proxy system for the behavior of nuclei that has an extreme ratio between neutron and protons. If we can describe these systems, it paves the way of understanding a large number of atomic nuclei which is currently a challenge for state-of-the-art theoretical models.

## 1.1 Nuclear structure

When E. Rutherford fired  $\alpha$  particles on a gold foil in 1911 he observed some of the  $\alpha$  particles being reflected backwards[3]. He concluded that the atom must have a compact core, thereby discovering the atomic nucleus. This led to the further discovery of the two building blocks of the nucleus, firstly the proton and finally the neutron (collectively referred to as nucleons) by James Chadwick in 1932[4]. Later it was discovered that the nucleons were in fact not fundamental, and they consisted the fundamental quarks, as described in the Standard Model. The internal structure of the nucleons is, however, rarely necessary to consider to describe nuclear phenomena.

The nucleus is made up of a number of protons,  $Z$  and a number of neutrons,  $N$ . The total number of nucleons is often denoted  $A$ . The protons carry an electric charge whereas the neutrons are neutral. The protons thus give the atom its chemical properties, and a particular number of protons defines the element. A single proton is known as hydrogen, whereas 79 protons are known as gold. An element can have different numbers of neutrons, and this is referred to as isotopes. A famous example is  $^{12}\text{C}$ , which is an essential element for organic material. It has an isotope with two extra neutrons,  $^{14}\text{C}$ , which is used for dating organic material due to its *radioactivity*.

The different combinations of protons and neutrons make up all the atomic nuclei we know. This is conveniently compiled into the nuclear chart shown in Figure 1.1. There are currently over 3000 known isotopes and

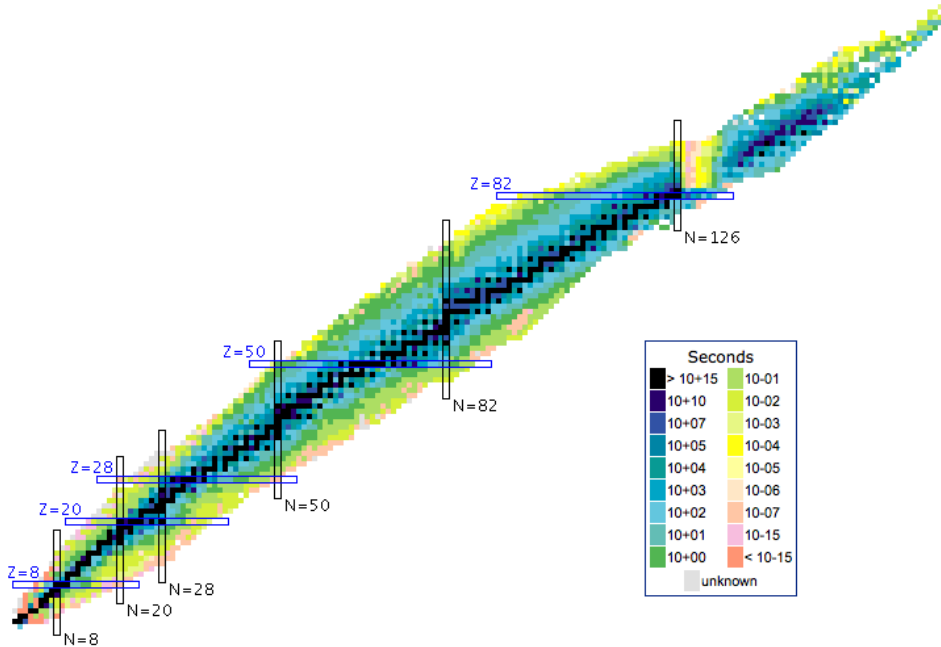


Figure 1.1: The nuclear chart. The number of neutrons is on the x-axis and the number of protons is on the y-axis. The stable isotopes are marked with black. The magic numbers are indicated for both neutrons and protons. Illustration taken from [https://www.meta-synthesis.com/webbook/33\\_segre/segre.html](https://www.meta-synthesis.com/webbook/33_segre/segre.html).

elements up to  $Z = 118$  has been synthesized in laboratories even though there are less than 350 naturally occurring isotopes.

The isotopes marked with black are stable isotopes. These configurations are favored by nature and will not decay. They have roughly the same number of protons and neutron, with a slight overweight of neutrons at the heavier systems. The black line in the nuclear chart is often referred to as the valley of stability.

If the balance gets skewed the isotopes become radioactive and will

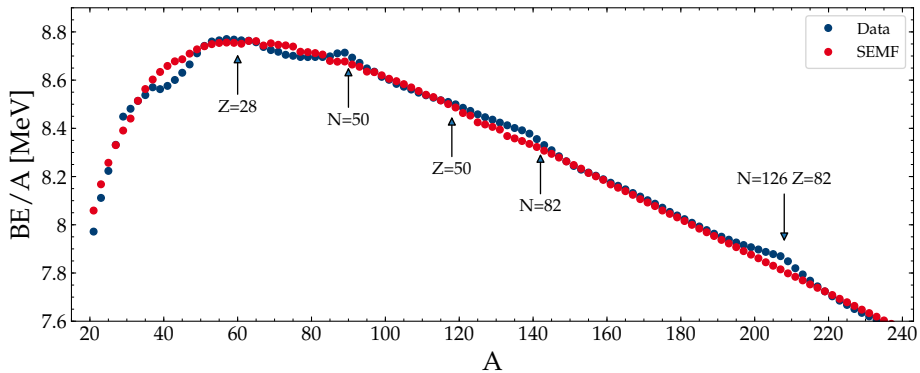


Figure 1.2: Binding energy per nucleon. Notice the areas where the data-points have higher binding energy than SEMF. They correspond to isotopes where either the number of protons, neutrons or both are magic.

eventually decay. This phenomenon was discovered by H. Becquerel in 1896 before the nucleus itself was discovered. There are several decaying mechanisms with  $\alpha$ ,  $\beta$  and  $\gamma$  being the most famous. With the development of quantum theory, these mechanisms were understood theoretically. The  $\alpha$  decay was described by Gamow in 1928 as quantum-mechanically tunneling and the  $\beta$  decay was first described by Fermi in 1934[5] and has since been understood in terms of the weak interaction.

When the ratio between neutron and protons becomes too extreme the nuclei begin to decay by emitting either a proton or a neutron. This is the so-called drip lines and marks the edge of the nuclear chart.

## 1.2 Models

The large domain of nucleon compositions poses a great challenge for a combined description of all nuclei. It has not been achieved yet, and we use multiple models to describe different aspects of the nucleus.

One very successful model is the *liquid drop model*. It was observed that the strong nuclear force was short-ranged and a nucleon would only interact with its nearest neighbors. This is analogous to a drop of molecules in a regular fluid. The liquid drop model, therefore, treats the atomic nucleus as a drop of an incompressible fluid. This model successfully described collective features such as deformations and was the basis for the first detailed fission calculations in 1939. This semi-classical picture also led to the development of the Semi-Empirical Mass Formula (SEMF), which accurately describes the masses and binding energies of many isotopes as shown in Figure 1.2.

### 1.2.1 Shell model

Some isotopes have a significantly higher binding energy, much like the noble gasses are very inert. This was noticed by Mayer and Jensen [6, 7]. They found that this occurs at certain numbers of nucleons and these numbers were denoted *magic numbers*. Experimentally it was  $N = 8, 20, 28, 50, 82, 126$ .

This apparent problem was solved with the *shell model*. The idea is inspired by the way the electrons occupy different orbitals in the central Coulomb potential from the nucleus. Inside the nucleus, however, there is no central potential. The potential that keeps the nucleons together arises from the nucleon-nucleon interaction. Instead, the nucleus is thought to make up an effective mean-field potential. The nucleons fill the orbitals arising from this effective central potential, much like the electrons in the atom.

It turns out that the magic numbers correspond to large energy gaps between certain orbitals. The shape of the central potential, is, however, essential to reproduce these energy gaps at the correct numbers. Remember that this effective potential is phenomenological by nature. It turns out that the magic numbers can be described by a Woods-Saxon-potential with a spin-orbit term

$$V(r) = \frac{-V}{1 + e^{(r-R)/a}} + V_{\text{ls}}(r)\vec{l} \cdot \vec{s}, \quad (1.1)$$

and the spin-orbit term turned out to be crucial to predict the correct numbers as compared to the electronic shells.

During the last 50 years, the study of isotopes far away from stability has shown, however, that these magic numbers break down. As the composition becomes more extreme the core potentials change accordingly. The imbalance between neutrons and protons shifts the core potential as well as introduce deformations. This leads to the closing of existing magic numbers and opening of new ones, often referred to as *shell evolution*. The neutron-rich  $^{24}\text{O}$  has for instance a new shell gap at  $N = 16$ [8]. On the contrary is the gap at  $N = 20$  closed in the region around  $^{32}\text{Mg}$ , the so-called Island of Inversion[9]. Krücken provides a nice overview of the existence of new magic numbers in [10].

### 1.3 Reactions

The nucleus was discovered through a reaction experiment, and this technique remains one of our key tools to study the interior of the atom, even a century later. The detection systems, data acquisition systems, and accelerator technology have, of course, improved immensely and we can study a much wider range of isotopes at many different energies.

Reaction studies remain important due to several reasons. With a beam, we can introduce more energy into the system, largely limited by the size of our accelerator. By tuning the energy correctly we can study many aspects of the nucleus. Different types of reactions are sketched in Figure 1.3.

Peripheral reactions that merely touches the surface is an excellent tool to study the behavior of the single-particle states in the shell model. Single nucleons can be transferred or knocked out, probing the individual levels in the nuclei. These are often referred to as direct reactions.

In a more head-on collision, the target and projectile fuse to form a *compound nucleus*, where the energy is shared among all the nucleons, eventually sending out a single nucleon or even a cluster. This happens on a much longer time scale as the newly formed nucleus first settles in an equilibrium.

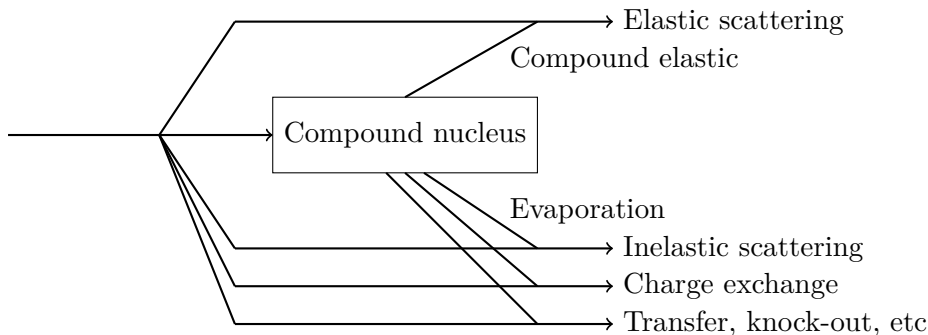


Figure 1.3: Different reaction mechanisms in a nuclear experiment.

An important breakthrough was the development of radioactive ion beams (RIB), and the ISOLDE facility at CERN is one of the facilities that can provide such radioactive beams. An excellent review of the state-of-the-art RIB facilities is given in [11]. Before this, only naturally occurring isotopes was known and studied. With this new technology, radioactive isotopes could suddenly be studied and many new isotopes were discovered leading to the nuclear chart as we know it today.

## 1.4 Exotic nuclei

When we move away from the valley of stability, the isotopes start to exhibit structures that are very unlike the stable ones. This gave rise to the notion of *exotic* nuclei.

One important feature is weakly bound valence nucleons. In particular, when moving close to the driplines, the binding energy of the valence nucleons can get very close to the threshold. This gives rise to the phenomena called *halo* nuclei. They are characterized by one or two nucleons which are loosely bound to a more compact core. This leads to a large spatial distribution and the halo nucleons spends a significant amount of time outside the classically allowed region. An excellent discussion of halos is given in [12].

These structural differences lead to shell evolution. The large spatial distributions, in particular, leads to large spin-orbit effects. This results in a change in the ordering of the energy levels from the standard shell model. This is not limited to halo nuclei, but the halos turn out to be a good proxy for studying such effects.

Both proton and neutron halos have been observed. A famous example, which is also part of the motivation for this thesis, is the two neutron halo  $^{11}\text{Li}$ , which was among the first to be discovered. Another example is  $^6\text{He}$ [13], which can be considered two neutrons orbiting an  $\alpha$  core. With only a single valence neutron  $^{11}\text{Be}$ [13] constitutes one of the most studied one neutron halos, both due to its particular first excited state, but also because of the  $\beta$ -decay from  $^{11}\text{Li}$ . Another one neutron halo which is interesting, not only for its halo structure but also its involvement in the astrophysical CNO cycles is  $^{15}\text{C}$ [14]. The one proton halo in  $^8\text{B}$  has also caught a lot of attention due to its astrophysical implications [15].

## 1.5 $^{10}\text{Li}$ and $^{11}\text{Li}$

The motivation for this thesis is the investigation of  $^{11}\text{Li}$  and its subsystem  $^{10}\text{Li}$ . The study of  $^{11}\text{Li}$  was unfortunately unsuccessful due to experimental issues. We will, however, briefly touch upon it in this section, as a part of the motivation for studying  $^{10}\text{Li}$ .

The first evidence for  $^{11}\text{Li}$  being a two neutron halo was presented in 1985 by Tanihata *et al.* [16]. They had measured the *rms* radii of several light nuclei and discovered a major increase in the spatial distribution of  $^{11}\text{Li}$  compared to other Li isotopes. The result is shown in Figure 1.4. The halo nature of  $^6,8\text{He}$  is also clearly seen, compared to stable  $^4\text{He}$ .

The interpretation is two loosely bound neutrons orbiting a compact  $^9\text{Li}$  core with  $S_{2n} = 369.15(65)$  keV [17] as illustrated on the right in Figure 1.4. This picture fits nicely into the shell model picture with its compact core. Simply filling up the shells, the two neutrons should occupy the  $1p_{1/2}$  state, see the left side of Figure 1.5. The experimental evidence, however, suggests that the ground state is, in fact, an almost equal mixing of the



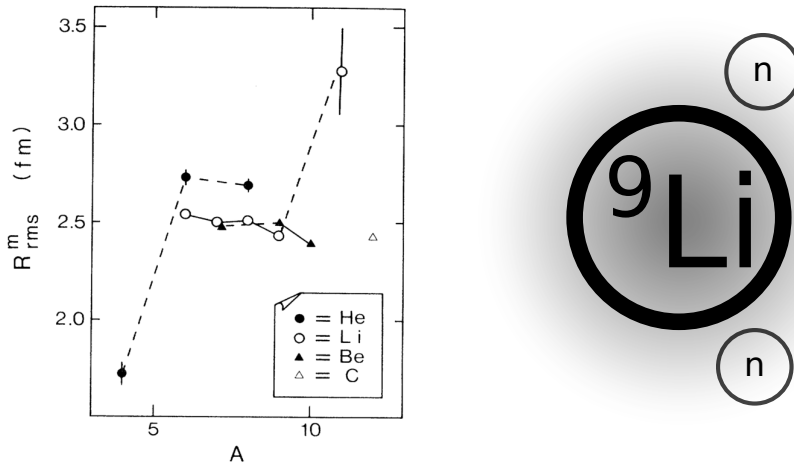


Figure 1.4: **Left** The mass distributions as measured by Tanihata *et al.* [16]. Notice, in particular, the large increase from  $^9\text{Li}$  to  $^{11}\text{Li}$ . **Right** The interpretation of  $^{11}\text{Li}$  as two neutrons orbiting  $^9\text{Li}$ .

$1p_{1/2}$  and  $2s_{1/2}$  states[18, 19].

The mixture of states has been observed in both  $\beta$ -decay experiments[20], fragmentations experiments[21] and a low energy transfer reaction experiment[22]. The discrepancy from the simple shell model can be explained as a shift in the  $2s_{1/2}$  state, as shown in Figure 1.5. This shift effectively closes the shell gap among light  $N = 7$  and  $N = 8$  isotones[13, 23].

The breakdown is further supported by neighboring isotopes, in particular, the parity of the  $^{11}\text{Be}$  ground state[19, 24, 25]. The simple shell model predicts the valence neutron to occupy a p-state, but the measured spin and parity are  $\frac{1}{2}^+$ , corresponding to a s-state. Also the ground state of  $^{15}\text{C}$  is  $\frac{1}{2}^+$ , suggesting that the  $2s_{1/2}$  has moved below the  $1d_{5/2}$  orbital. A good discussion of this is found in [23].

Another feature of  $^{11}\text{Li}$  is its *borromean* nature. The Borromean rings consist of three rings, where no pair is connected if you remove the third

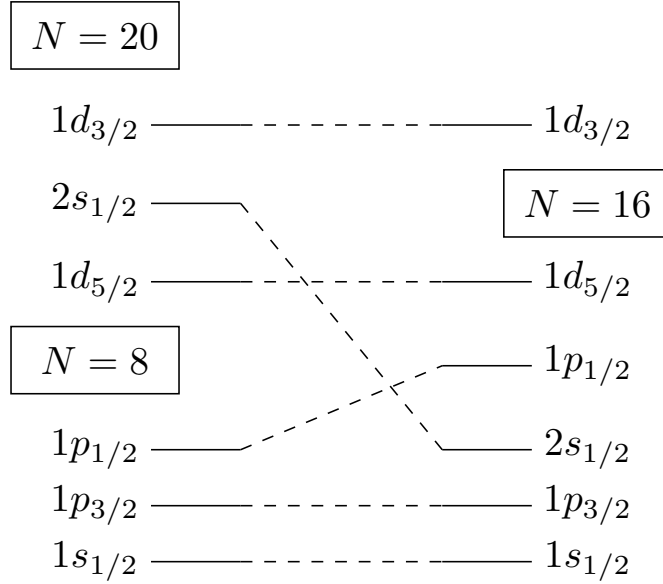


Figure 1.5: Energy levels in the shell model. On the left is the simple shell model shown. On the right is the closing of the  $N = 8$  shell shown as a shift in the  $2s_{1/2}$  orbital.

ring. Similarly, every pair in  $^{11}\text{Li}$  is unbound, both  $nn$  and  $n^9\text{Li} = ^{10}\text{Li}$ . The study of  $^{10}\text{Li}$  is, however, of great importance to theoretically understand  $^{11}\text{Li}$ . Furthermore, it sheds light on the  $s_{1/2}$  intruder state among the  $N = 7$  isotones. Such a virtual state should cause a parity inversion for  $^{10}\text{Li}$ , since the last neutron would occupy an  $s_{1/2}$ -orbital instead of a  $p_{1/2}$ -wave. If the neutron occupy the  $s_{1/2}$  it gives rise to two negative parity resonances, whereas the coupling to  $p_{1/2}$  gives rise to two positive parity resonances

$$\begin{aligned}
 (l \otimes s_n ; j_n) \otimes J_{9\text{Li}}^p &= J_{10\text{Li}}^p \\
 (0 \otimes 1/2; s_{1/2}) \otimes 3/2^- &= 1^-, 2^- \\
 (1 \otimes 1/2; p_{1/2}) \otimes 3/2^- &= 1^+, 2^+
 \end{aligned}$$

where  $l$  is the orbital angular momentum between  $^9\text{Li}$  and the neutron,  $s_n$  is the spin of the neutron and  $j_n$  is the total angular momentum.

Numerous experiments have been performed, to piece together the current consensus which is as follows[23, 26]. The ground state is the coupling of a low-lying virtual neutron  $s$ -wave to the  $^9\text{Li}$  ground state, with one being resonant below 50 keV as well as a  $p$  resonance close to 0.5 MeV. It is not clear if there are one or two resonant  $p$  states.

This is an experimental result since there are theoretical predictions for both an  $s_{1/2}$ -wave coupling and a  $p_{1/2}$ -wave coupling to the  $^9\text{Li}$  ground state being lowest in energy [27, 28]. The  $p_{1/2}$  would couple to two states as well, a  $1^+$  and a  $2^+$ , however, the current experimental data can not distinguish two  $p$  states, leaving no consensus about the ordering.

The existence of a virtual  $s$ -wave was crucial to explain the results from two reaction experiments at GSI[21, 29] both studying  $^{10}\text{Li}$  as a subsystem of  $^{11}\text{Li}$ , see Figure 1.6 (A) and (B) respectively. In particular, the momentum distribution is too narrow to be purely  $p$ .

A different reaction experiment interpreted their measurement as a low-lying  $s$ -wave and a  $p$ -wave at  $E = 0.566 \pm 0.014$  MeV[33]. These results are in good agreement with both another neutron knockout experiment[34] as well as a neutron transfer experiment[35], see Figure 1.6 (C), the predecessor to the experiments in this thesis.

A more recent experiment from TRIUMF reports a large contribution from the  $p$ -wave but no substantial  $s$ -wave contribution [30], see Figure 1.6 (D). It should, however, be noted that this experiment only covers a small angular range at very forward angles, where the contribution from an  $s$ -wave is expected to be small.

There have been several theoretical approaches to describe the  $^{10}\text{Li}$  system. A Faddeev approach was carried out by Garrido *et al.*, finding the current picture consistent with experimental data[36]. They could, however, not give determine any ordering of the resonances.

Moro *et al.* has attempted to reconcile the results from the two mentioned (d,p) experiments, [35] and [30] (C and D in Figure 1.6) in a recent paper [32] with a transfer-to-continuum framework. Both experiments were analyzed with the same structure model and the same reaction framework and they

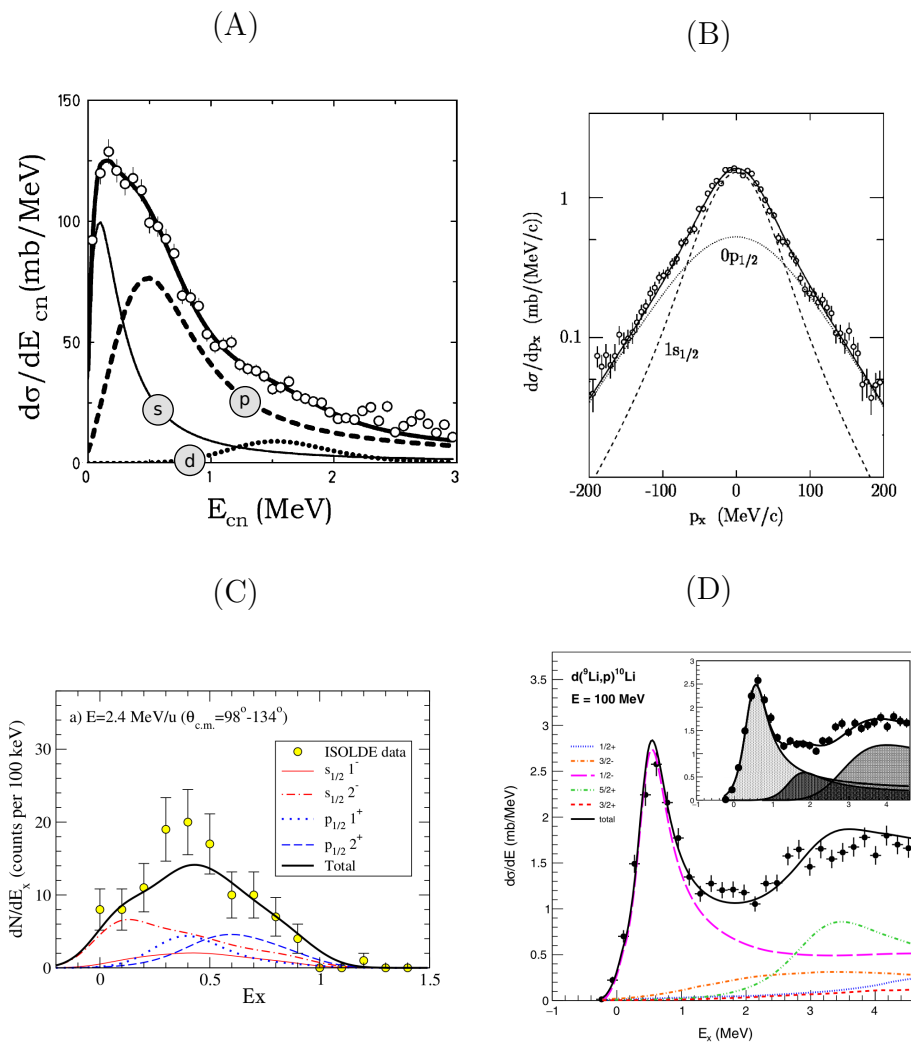


Figure 1.6: Previous experimental results for  $^{10}\text{Li}$ . (A) Excitations spectrum from [29]. (B) The transverse momentum distribution of  $^{10}\text{Li}$  from [21]. (C) The results from [30]. (D) The results from [31] with the theoretical work from [32].

conclude that the two data sets are in fact consistent. Notice that an  $s$ -wave contribution is consistent with both data sets. I will adapt this theoretical approach to describe the results of our experiments.

Another theoretical approach came to the same conclusion based on a renormalized field theory [37].

A more controversial contribution is that of a  $d_{5/2}$  orbital from  $l = 2$ . Such a state was reported in [34] at  $\approx 1.5$  MeV and supported by theoretical work by [38]. A contribution at  $\approx 2.9$  MeV in [30] is also interpreted as a significant  $d_{5/2}$  contribution.

Despite the theoretical advancements, more experiment data is still required to confirm the  $s$ -wave contribution with better statistics, to settle the number of resonant  $p$ -states and lastly to shed more light on the controversial  $d$ -wave contribution.

## 1.6 Experimental approach

To study the structure and in particular the shell inversion in  $^{10}\text{Li}$  and  $^{11}\text{Li}$ , we need to probe the single-particle states. An excellent and well-proven technique is transfer reactions. In particular, the (d,p) reaction is a common technique[39], where a neutron is transferred from a deuteron to  $^9\text{Li}$ . Similarly, we can use tritons and transfer two neutrons to produce  $^{11}\text{Li}$ , a (t,p) reaction. A nice discussion of the advantages of transfer reactions is given by W. Catford in [40].

It is not trivial to make reactions with  $^9\text{Li}$  due to its half-life of 172 ms[26]. If used as the target, it will decay much faster than the experiment can be performed. Instead, the experiments must be performed with a  $^9\text{Li}$  beam and a target containing deuterons or triton.

$^{11}\text{Li}$  has been studied in many experiments[34, 41–43] but always starting from the  $^{11}\text{Li}$  ground state. This has sparked a debate whether the indications for a resonance at 1.3 MeV was actually due to the reaction mechanism or not[44]. To contribute to this debate, the goal was to start from  $^9\text{Li}$  and reach the resonance via a two neutron transfer.

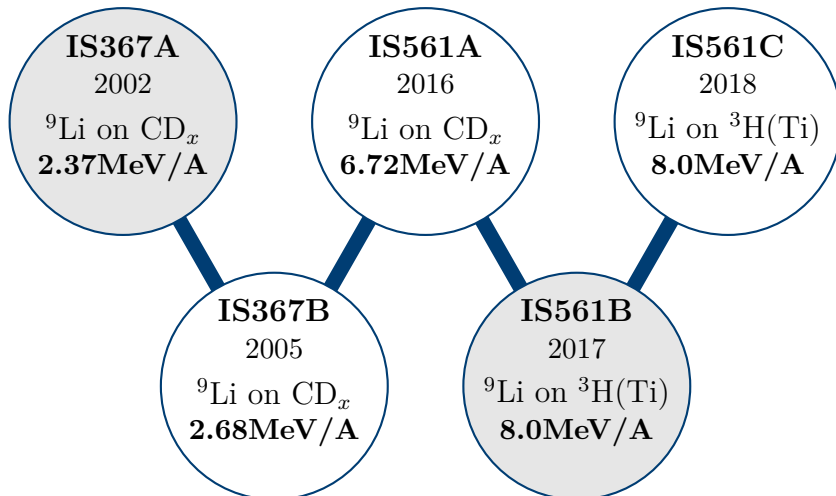


Figure 1.7: An illustration of the timeline of the experiments. The two experiments that are greyed out (IS367A and IS561B) are not included in this thesis.

ISOLDE has a history of providing good  ${}^9\text{Li}$  beams, and we can contribute with experiments with better statistics and in a slightly different kinematical region than earlier experiments. Compared to previous energies ISOLDE provides lower beam energies, but with the newly upgraded HIE-ISOLDE facility can we reach up to 8 MeV/A.

## 1.7 The timeline and structure of thesis

The experimental campaign for this thesis started before I joined. An outline is presented in Figure 1.7.

The first (d,p) experiment, IS367A, was carried out in 2002 at REX-ISOLDE, the predecessor of HIE-ISOLDE, and was followed up in 2005 with an improved setup, IS367B. The ISXXX nomenclature stems from the catalog number of a given experiment from ISOLDE. The ABC-suffix is

used to differentiate different parts of the same experiment. I will continue with this naming throughout the thesis. The results from IS367A were published in a series of papers by Jeppesen and collaborators [31, 35, 45], but the majority of the data from IS367B was never published. I started my project by analyzing this data. Since I did not take part in IS367A or have worked with the data, I will refer to IS367B simply as IS367.

In 2016 we got beam time as the first experiment at HIE-ISOLDE and carried out another (d,p) experiment at 6.72 MeV/A and with a newly designed setup. In 2017 this experiment was followed by an attempt to perform a two neutron transfer to  $^{11}\text{Li}$ . We did, however, have multiple issues with the beam and setup and I have chosen not to include this experiment in this thesis. In the fall of 2018, we were lucky enough to get another attempt. The triton target was, unfortunately, faulty in this experiment and we reverted to a deuterated target instead. I have therefore focused my analysis of  $^9\text{Li}(d,p)^{10}\text{Li}$  at three different energies.

I will begin the remaining of the thesis with a discussion of the kinematic considerations that goes into these types of experiments, followed by several chapters about the technical aspects of the experiments and the data analysis, which were common for all three experiments. This includes ISOLDE, detectors, calibration, beam diagnostics, data acquisition, and analysis software. I will then describe the three experiments in detail, and present some initial analysis for each.

To evaluate the results, I will present a method to correct for acceptance of the kinematics of the experiment and the geometry of the setup, which in turn produces absolute differential cross sections. This is followed by a description of the scattering theory I will use to interpret the results, as well as a description of the  $^{10}\text{Li}$  model I will use. After this, I will compare the data to theoretical calculations.

Finally, I will summarize and discuss some future improvements to our methods.

In accordance with GSST rules, parts of this thesis were also used in the progress report for the qualifying examination.





---

# Kinematics

We can say a lot about the outcome of a reaction experiment before actually performing the experiment with simple considerations about energy and momentum conservation – the *kinematics* of the reactions. The kinematics reveals many important features of a reaction experiment, even when the aim is to study an unknown aspect of one or more reaction products. Some angular regions may be completely unfeasible and detector coverage is wasted, whereas other regions might require increased resolution.

The final analysis also depends on kinematical calculations. The excitation of a fragment can usually be deduced by the missing energy in the system and therefore the kinematics.

Typically experiments are designed to be as simple as possible and two-body reactions are an excellent choice. If the reaction populates unbound states the two-body description is not sufficient due to breaking up into multiple constituents. We are, however, still able to learn something from a simple two-body picture, especially close to the threshold for the breakup.

In this chapter, I will discuss the main features of the two-body reaction and discuss the challenges of using a beam of particles that are heavier than the target, so-called *inverse kinematics*. Treatments of basic kinematics can be found in most text books on nuclear physics such as [46, 47]. I will therefore not go into all the details, but highlight the results that are important for this thesis.

Since our experiments are carried out at relatively low energies, the treatment of the kinematics will be purely classical.

## 2.1 Two-body kinematics

Consider a beam particle  $A$  impinging on a target particle  $a$  with kinetic energy  $T_A$  in the laboratory frame. The target is assumed at rest and has no kinetic energy,  $T_a = 0$ . They interact in some way and produce a recoil  $B$  and an ejectile  $b$

$$A + a \rightarrow B + b. \quad (2.1)$$

If both the projectile and the target are initially in the ground state, conservation of energy dictates

$$T_A = T_B + T_b + E_B^* + E_b^* - Q, \quad (2.2)$$

where  $E_b^*$  is the excitation energy of the ejectile,  $E_B^*$  is the excitation energy of the recoil and

$$Q = (m_A + m_a - m_B - m_b)c^2. \quad (2.3)$$

The available energy for the reaction, the *channel energy*, is

$$E_{ch} = \frac{m_a}{m_a + m_A} T_A \quad (2.4)$$

Linear momentum conservation gives

$$\vec{p}_A = \vec{p}_B + \vec{p}_b, \quad (2.5)$$

where  $\vec{p}_i = \sqrt{2T_i m_i} \hat{n}_i$  and  $\hat{n}_i$  is the unit vector in the direction of motion.

With the initial conditions of  $A$  and  $a$  Eq. (2.2) and Eq. (2.5) can be rearranged to calculate the relationship between the energy of the ejectile angle  $\theta_b$  and its kinetic energy  $T_b$ , called the *kinematic curve* [46]

$$T_b^{1/2} = \frac{\sqrt{m_A m_b T_A} \cos \theta_b \pm \sqrt{m_A m_b T_A \cos^2 \theta_b + (m_B + m_b)[m_B \tilde{Q} + (m_B - m_A)T_A]}}{m_B + m_b}, \quad (2.6)$$

where  $\tilde{Q} = Q - E_B^* - E_b^*$ .

The naming of the particles is in principle arbitrary, and Eq. (2.8) can calculate the kinematic curve for both the projectile and recoil by simply changing the labels  $B \leftrightarrow b$ .

If the beam energy is below a certain threshold there are no solutions, and the reaction can not occur due to energy conservation. Above the threshold, however, it is quadratic and can have one or two solutions

Examples of both single valued and double valued kinematic curves can be seen in Figure 2.1 (B) for elastic scattering of  ${}^9\text{Li}(d,d){}^9\text{Li}$ .

Due to energy and momentum conservation, a measurement of the ejectile can uniquely infer the kinematics of the recoil and vice versa. If the ejectile stays in the ground state (which is reasonable in the case of deuterons and tritons since they would be unbound otherwise) the excitation energy of the recoiling nucleus is given by Eq. (2.2) and Eq. (2.5)

$$\begin{aligned} E_B^* &= T_A - T_B - T_b + Q \\ &= T_A - T_b - \frac{(\vec{p}_A - \vec{p}_b)^2}{2m_B} + Q, \end{aligned} \quad (2.7)$$

where  $T_A$ ,  $\vec{p}_A$  and  $Q$  are known and  $T_b$  and  $\vec{p}_b$  are measured.

## 2.2 Kinematic compression

If the mass of the beam is heavier than the target, the kinematics changes accordingly. There is, as such, no new physics involved, but our intuition may need a slight adjustment. A heavy beam leads a *kinematic compression*. There is a nice discussion in [40] to gain a better intuition about how to think about transformations between LAB and CM in inverse kinematics. We will, however, calculate the kinematic curves for different reactions to get a better understanding. The concrete reactions from the experiments will guide this discussion, that is  ${}^9\text{Li}(d,t){}^8\text{Li}$ ,  ${}^9\text{Li}(d,d){}^9\text{Li}$  and  ${}^9\text{Li}(d,p){}^{10}\text{Li}$ .

Consider elastic scattering  ${}^9\text{Li}(d,d){}^9\text{Li}$ . In this case, the projectile and the heavy recoil have the same mass,  $m_B = m_R$ , and  $\tilde{Q} = 0$ . The kinematic

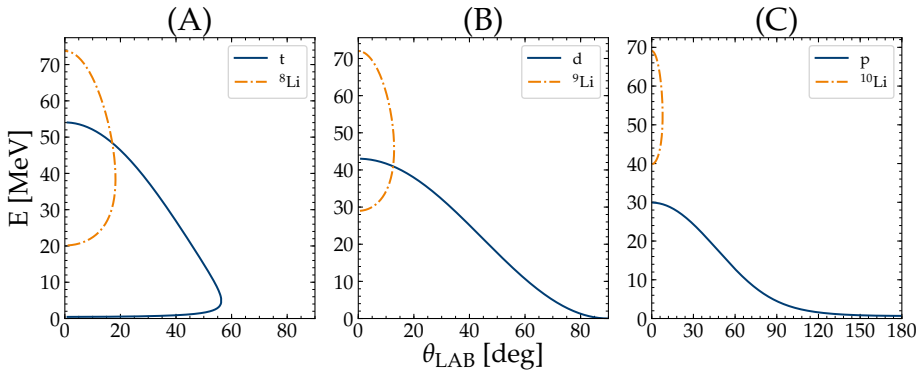


Figure 2.1: Kinematic curves of ejectile and recoil from the reactions  ${}^9\text{Li}(d,t){}^8\text{Li}$ ,  ${}^9\text{Li}(d,d){}^9\text{Li}$  and  ${}^9\text{Li}(d,p){}^{10}\text{Li}$  at 8.0 MeV/A shown in (A), (B) and (C) respectively.

curve reduces to

$$T_b^{1/2} = \frac{\sqrt{m_A m_b T_A} \cos \theta_b \pm \sqrt{m_A m_b T_A \cos^2 \theta_b}}{m_B + m_b}, \quad (2.8)$$

which vanishes when  $\theta \geq 90^\circ$ . The resulting kinematic curves for the ejectile and the recoil is shown in Figure 2.1 (B).

All the deuterons are scattered in the first  $90^\circ$  in LAB, effectively compressing the full angular range in CM to only  $90^\circ$  in LAB.

The heavy recoil is focused at small LAB angles since it eventually bends back toward  $0^\circ$ . This has two important implications. First, it requires the setup to cover the angles close to the beam axis. Secondly, the angular resolution suffers close to the turning points, since a lot of CM-angles are compressed into a small angular range of the LAB frame.

If a nucleon is transferred, the  $Q$ -value of the reaction changes and the reaction mechanism determines the resulting kinematics. A neutron transfer to the target behaves differently than a neutron transfer to the beam.

Figure 2.1 (B) shows the kinematic curves for  ${}^9\text{Li}(d,p){}^{10}\text{Li}$ . The ejectile is single-valued all the way to  $180^\circ$ . The energy at backward angles is,

however, much lower. The proton energy can be increased by increasing the beam energy. An experimental setup will have some threshold that determines how low energy protons it can detect. It is thus necessary to increase the beam energy enough to be able to actually measure the protons in the backward directions if desired. This asymmetric energy distribution is important to consider when designing the setup.

The recoil is scattered even closer to the beam axis, and coincidence measurements requires coverage even closer to the beam axis than in the case of elastic scattering. Moreover, the angular resolution will be even worse, especially at the region around the maximally scattered recoils.

The kinematic curves for  ${}^9\text{Li}(d,t){}^8\text{Li}$  are shown in Figure 2.1 (A). In this case even light ejectile, the triton, bends back. Notice, however, that the recoil scatters further from the beam axis, making this situation better for coincidence measurements.

### 2.2.1 Detector coverage

When designing an experiment it is important to consider which angles the detectors should cover, for instance, the ones favored by the reaction.

In the previous section, we discussed how inverse kinematics compresses the angular resolution at the forward LAB angles. This means that the angular resolution will be different across the angular range if similar detectors are used. Take for instance the case of  ${}^9\text{Li}(d,p){}^{10}\text{Li}$ . The angular resolution,  $d\theta_{\text{CM}}/d\theta_{\text{LAB}}$ , at 2.68 MeV/A is shown in Figure 2.2 (B). A better angular resolution is required at forward angles compared to backward angles to obtain comparable CM resolution in both regions. The required resolution, however, also depends on how fast the angular distributions are expected to vary. If the distribution is rather flat, there is no need for a high resolution.

This dependence on the angles is even more significant in terms of the solid angle transformation. If the LAB angles are focused in the forward angles, they are stretched in the backward angles. To cover a comparable CM solid angle the setup should thus cover a larger area at the backward LAB angles compared to the forward LAB angles. We can quantify this with

the Jacobian that transforms angular cross sections from CM to LAB[48]

$$\frac{d\sigma}{d\Omega_{\text{LAB}}} = J(\theta_{\text{CM}}) \frac{d\sigma}{d\Omega_{\text{CM}}}, \quad (2.9)$$

where

$$J(\theta_{\text{CM}}) = \frac{(1 + \gamma^2 + 2\gamma \cos \theta_{\text{CM}})^{3/2}}{|1 + \gamma \cos \theta_{\text{CM}}|}, \quad (2.10)$$

and

$$\gamma = \frac{m_A m_a}{m_B m_b} \sqrt{\frac{E_{\text{ch}}}{E_{\text{ch}} + Q}}. \quad (2.11)$$

The Jacobian transformation is shown in Figure 2.2 (C). It exhibits a strong enhancement in the forward angles and equally strong suppression in the backward LAB angles. More coverage at backward LAB angles is thus required to get a reasonable integrated cross section.

A real experiment requires a certain amount of statistics to extract the physics. The so-called  $\sin \theta$  effect must thus also be taken into account. This effect is due to the fact that a differential solid angle is given as  $d\Omega = \sin \theta d\theta d\phi$ . Going away from  $\theta = 90^\circ$  there is thus a further suppression due to the  $\sin \theta$  factor. Considering  $J(\theta) \sin \theta$  instead the transformation is shown in panel (D).

When designing an experiment, it is important to keep in mind that the number of measured particles is heavily suppressed in backward directions when working in inverse kinematics. As shown in panel (D), there is a suppression of several orders of magnitude between the maximum close to  $50^\circ$  and a backward angle such as  $150^\circ$ .

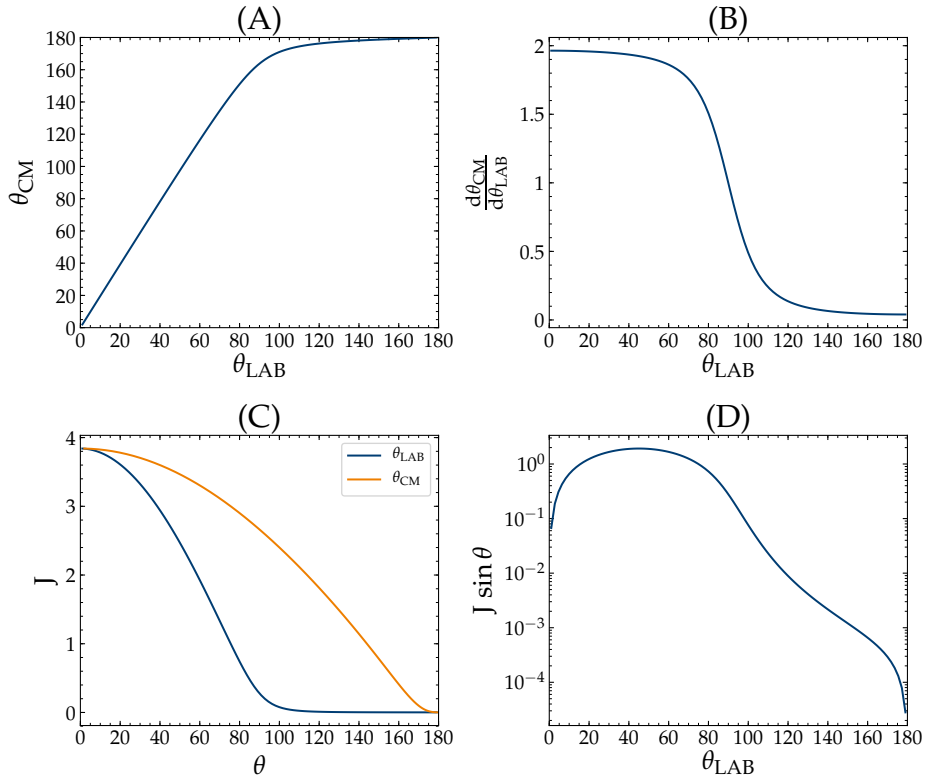


Figure 2.2: Kinematic effect on angular resolution and solid angle coverage. All the plots correspond to a proton from  ${}^9\text{Li}(d,p){}^{10}\text{Li}$  at 2.68 MeV/A. (A) The relation between the scattering angle in LAB and CM. (B) The differential, which gives a measure of the angular resolution in LAB needed to recover a given angular resolution in CM. (C) The Jacobian that transforms from CM to LAB plotted. Since there is a 1-1 correspondence between  $\theta_{\text{CM}}$  and  $\theta_{\text{LAB}}$  it is plotted as a function of both. (D) The Jacobian times  $\sin \theta$  plotted as a function of  $\theta_{\text{LAB}}$ .





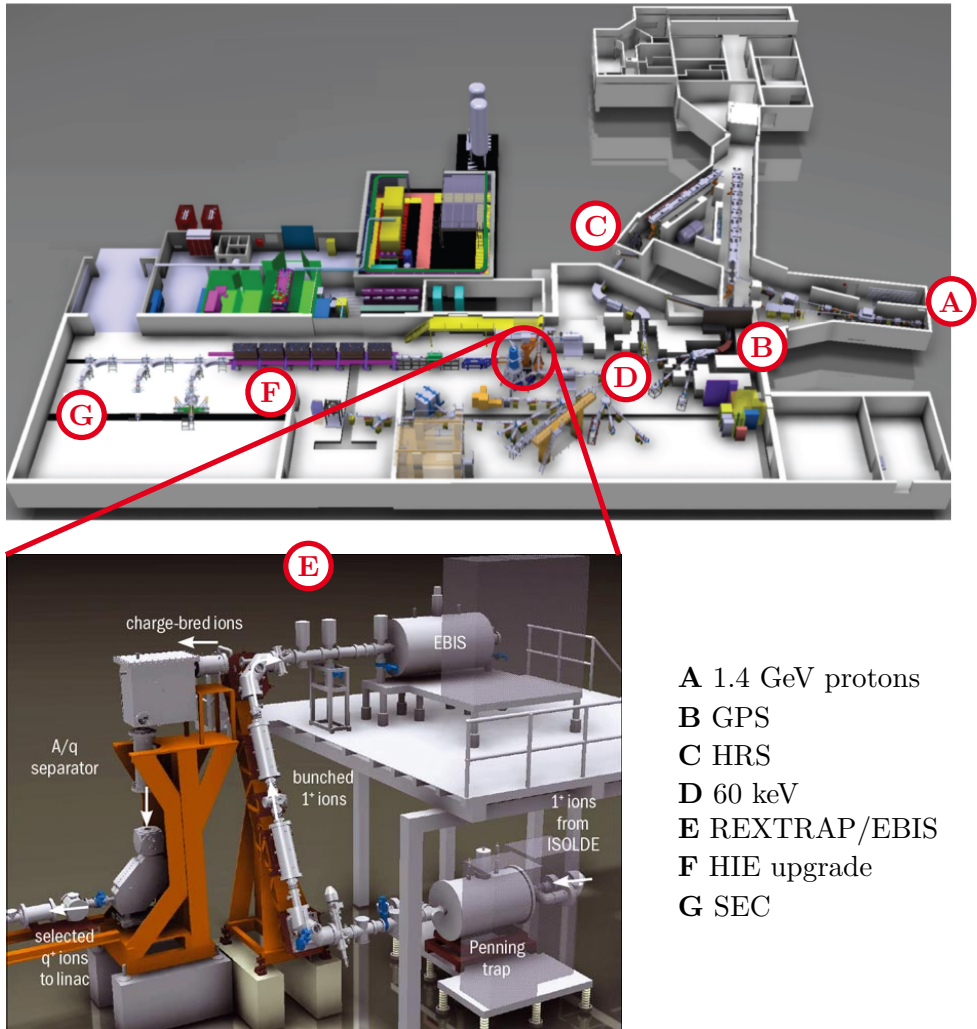
---

## Experimental technique

In this chapter, I will discuss some technical topics that are common for all three experiments. There has been a variety of upgrades to the techniques and equipment between the experiments, but the main concepts remained the same.

Performing experiments with highly unstable isotopes is no trivial task due to their very short lifetime. In the case of  ${}^9\text{Li}$  there is just  $t_{1/2} = 178.3(4)$  ms[26] to perform the experiment before half the nuclei has decayed. This can not be done in with  ${}^9\text{Li}$  as the target. Instead, it can be reversed and use a radioactive ion beam (RIB) of  ${}^9\text{Li}$  impinging on hydrogen isotopes. Deuterons can easily be implanted in a plastic foil, taking the place of protons. A small percentage of the protons will remain, giving rise to a contamination that must be assessed in the analysis. Tritium can, on the other hand, be absorbed in titanium. Several RIB-facilities across the world exists but the experiments of this thesis were all performed at the ISOLDE facility at CERN, in Switzerland. Between IS367 and IS561A there was a major upgrade of the facility, the HIE-ISOLDE upgrade, which increased the available beam energies.

The charged particles were detected with standard silicon detectors. The data acquisition system will be described in Chapter 6. As I did not take part in the IS367 experiment I will not discuss the data acquisition system from this experiment.



- A 1.4 GeV protons
- B GPS
- C HRS
- D 60 keV
- E REXTRAP/EBIS
- F HIE upgrade
- G SEC

Figure 3.1: Schematic overview of ISOLDE. The PS Booster delivers 1.4 GeV protons (A) impinging on a heavy primary target. This produces fragments which are separated in either the GPS (B) or the HRS (C). The resulting beam is 69 keV (D). To further accelerate this, it is trapped and further ionized with an electron beam in the EBIS (E). After another separation stage, it is accelerated through the superconducting cavities of the HIE-upgrade (F) and finally delivered at the experiment station, the SEC (G). See the main text for more details. Images from [49].

### 3.1 ISOLDE

The radioactive beams at ISOLDE are produced using the isotope separation on-line (ISOL) method[50]. An overview of the ISOLDE facility is shown in Figure 3.1. A pulse of 1.4 GeV protons from the PS Booster impinges on a primary target of a heavy element (**A**), for instance,  $\text{UC}_x$  or Tantalum. This produces a wide array of different isotopes through fragmentation, spallation, and fission. The target is heated to temperatures between  $700^\circ$  to  $2000^\circ$  which makes the products evaporate and diffuse into the ion source. Inside the ion source, they are laser ionized by either RILIS or a plasma ion source and subsequently accelerated to  $\approx 60$  keV. They are sent to one of the two mass separators GPS (**B**) or HRS (**C**). The GPS (General purpose separator) have a single bending magnet and the HRS (High resolution separator) have two bending magnets. The mass separators separate the particles according to their masses and the isotope of interest can be sent to one of the experiments.

The beam has an energy of 60 keV after the separators (**D**). This is not enough to do reaction studies and a post-acceleration stage is required. The first installation to perform post-acceleration of the beam was REX-ISOLDE and it was installed between 2001 and 2005. The beam particles are trapped, cooled down and bunched in a Penning trap, the REXTRAP (**E**). A buffer gas is used in the cooling process. These bunches are continued into an electron beam ion source (EBIS). Inside the EBIS the beam is highly ionized before it is sent through another separator, which separates according to  $A/q$  to get rid of the buffer gas residues. In our experiments,  ${}^9\text{Li}$  was fully ionized to  ${}^9\text{Li}^{3+}$ . Since it is separated according to  $A/q$ , we had to be aware of contaminations such as  ${}^{12}\text{C}^{4+}$  and  ${}^{18}\text{O}^{6+}$ . After the separator, the beam is sent into a linear accelerator which can accelerate them up to  $\approx 3$  MeV/A.

The REX-ISOLDE was used for post acceleration in IS367. In the decade following this experiment, a series of superconducting cavity modules were installed to increase the post acceleration capabilities. This was part of the HIE-ISOLDE upgrade, which aims to provide **H**igh **I**ntensity and **E**nergy[51, 52]. The superconducting cavities were parts of the energy upgrade and were completed with the seventh module in August 2018 (**F**). In 2016 only

two of the modules were installed, and 6.72 MeV/A was the highest energy that was reached until then. After the post-acceleration stage, the beam is delivered to our experimental setup at the Scattering Experiments Chamber (SEC) (**G**).

### 3.1.1 TEBIS and TPROTON

The protons from the PS Booster are delivered across the CERN facility. Since multiple facilities are running simultaneously only a fraction of these protons reach ISOLDE. They are delivered in bunches with a period of 1.2 s, the so-called *super cycle*. Typically the average beam current is 1  $\mu$ A-2  $\mu$ A. The delivery time for each proton pulse on the primary target is, however, timestamped and recorded in the data stream. This provides the time since proton impact for the measured events in the setup. We refer to this time as the **TPROTON**.

Due to the large timescale of the supercycle, it clearly shows the decay characteristics of the beam. This provides good evidence on the beam composition and thus whether the beam is indeed  $^9\text{Li}$ . Figure 3.2 (A) shows the **TPROTON**-spectrum for  $^9\text{Li}$  induced reactions. The clear steps in increments of 1.2 s correspond to the supercycle. The fast rise, in the beginning, is the production, extraction and acceleration time, before they end up in the chamber. This is followed by an exponential slope, which corresponds to the decay of  $^9\text{Li}$ , the key indication of the  $^9\text{Li}$  component in the beam.

**TPROTON** can also be used to limit background contributions. Backgrounds from the buffer gases would be uncorrelated with **TPROTON** and give a flat contribution. By restricting the **TPROTON** to the first 3-4 lifetimes, we can omit a considerable amount of background, however, we will also discard some false negatives. This will, however, be a small fraction since most of the  $^9\text{Li}$  arrives in the first second or so.

A better constraint can be achieved from the EBIS release. The trap releases a bunch with a well-defined repetition frequency (typically around 30 Hz) and each of these "spills" have a well-defined length. The beginning of each spill is timestamped when the trap is opened, providing with the

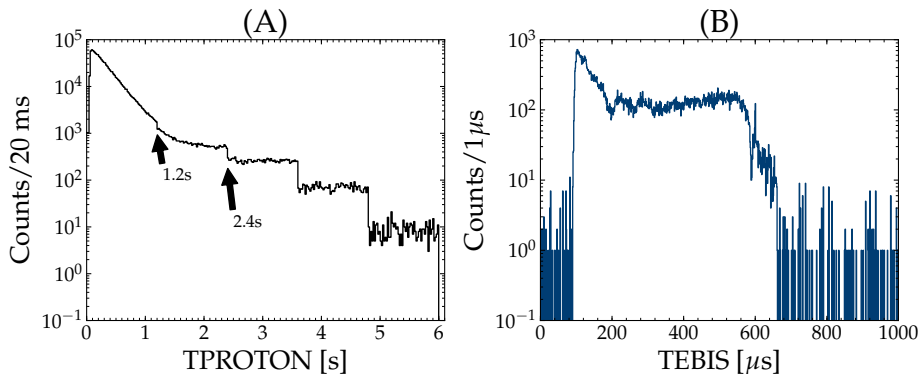


Figure 3.2: (A) A TPROTON spectrum for  $^9\text{Li}$  impinging on deuterated plastic from IS561A. (B) A TEBIS spectrum for  $^9\text{Li}$  impinging on deuterated plastic from IS561A.

time between the beginning of the spill and a given event. We refer to this time as TEBIS, and a spectrum is shown in Figure 3.2 (B). The events are nicely contained to a region of  $\approx 700 \mu\text{s}$ , corresponding to the release time. We can thus exclude background components by gating on this window. Background sources such as noise are in general uniformly distributed and can be suppressed significantly.

Since the EBIS release is relatively short and the release curve is concentrated in the first  $100 \mu\text{s}$ , the instantaneous rate is effectively very high. With a repetition rate of 30 Hz and a release of  $\approx 600 \mu\text{s}$  the beam arrives in only  $700 \mu\text{s} \cdot 30 \text{ Hz} = 21 \text{ ms}$  of each second. This means that the average intensity during a release will be two orders of magnitude larger than the reported intensity. It will be even larger at the beginning of the release. This put extra requirements on the data acquisition system in order to keep up.

## 3.2 Detectors

The main workhorse for charged particle spectroscopy is silicon detectors. The silicon detectors work as a  $pn$ -junction in reverse bias. When a charged particle traverses the detector an electron-hole pair is created[53]. By applying a bias across the detector, we can collect and digitize these charges. We generally use two types of silicon detectors.

To get position information we use *double sided silicon strip detectors* (DSSD). An example is shown in Figure 3.3. The electrodes that read out the charges are segmented into a number of strips. On one side of the detector, these strips are oriented horizontally and on the other side, they are oriented vertically. When a particle hit the detector, ideally the charge is split evenly between a strip on each side (electrons goes to one side, holes to the other side) and we get a signal in two orthogonal strips. This lets us determine which *pixel*, i.e. which small area that overlaps with both strips that were hit.

The second kind of detectors are the simpler unsegmented detectors. They consist of is a single silicon wafer, and we do not have any positional information from these. We will refer to these as a *pad*.

DSSDs comes in many different sizes and geometries, and I will shortly describe the kinds we use. I will refer to their unique product names.

**W1** Square DSSD with 16 strips on each side. This gives 256 pixels. Each strip has a width of 3 mm and an interstrip region of 100  $\mu\text{m}$ . They come in different thicknesses, but during these experiments, we used 60  $\mu\text{m}$ .

**BB7** Another square DSSD but with 32 strips on each side. This gives us a greater angular resolution compared to the W1. The strip width is 2 mm and the interstrip region is 100  $\mu\text{m}$ .

**S3** A round DSSD with a hole in the middle. The front side consists of 32 radially oriented strips (spokes) and the backside consists of 24 rings. Each ring is 886  $\mu\text{m}$  wide and each radial spoke covers  $11.25^\circ$ . The radius of the



Figure 3.3: Picture of a W1 detector. The segmentation of the silicon is orthogonal on the two sides, effectively creating a number of pixels.

inner hole is 11 mm. This detector was used in two of the experiments, and was 1 mm thick.

### 3.3 $\Delta E - E$ telescope

We can use a combination of two silicon detectors to distinguish between different particle types. If a particle has enough energy it will penetrate the detector and only deposit a part of its energy in the detector. If there is a thick pad detector behind the DSSD which stops the particle, the correlation between the energy deposited in the front detector and the back detector uniquely identifies the particle while still measuring the full energy. We call such a setup for a  $\Delta E - E$  telescope.

An example of the correlation is shown in Figure 3.5 (A). The energy

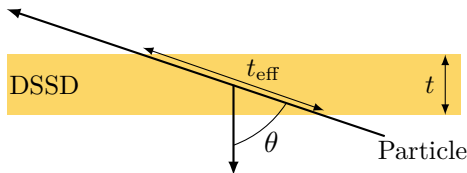


Figure 3.4: The angle,  $\theta$ , between the normal of the detector and the particle determines the actual length  $t_{\text{eff}}$  the particles travel in the detector.

in the front DSSD is shown as a function of the energy in the backing pad. The upper feature corresponds to  $\alpha$  and the lower feature corresponds to hydrogen isotopes. The hyperbolic shape is described by the Bethe-Bloch formula.

The energy deposited in the front detector, however, depends on the distance traveled and thus on the incoming angle,

$$t_{\text{eff}} = \frac{t}{\cos \theta}, \quad (3.1)$$

where  $t_{\text{eff}}$  is the distance traveled,  $t$  is the thickness of the detector and  $\theta$  is the angle shown in Figure 3.4. Each particle, depending on the angle, will thus deposit a different amount of energy even if they are identical. This smears out the features, effectively making the hydrogen isotopes hard to distinguish. This can, however, be corrected for.

Assume that the energy loss is constant through the front detector. The energy deposited in the front detector will then be proportional to the thickness,

$$\Delta E = \frac{dE}{dx} \cdot t. \quad (3.2)$$

For a particle incident at  $\theta$ , this translates to a larger energy loss

$$\Delta E = \frac{dE}{dx} \cdot t_{\text{eff}} = \frac{dE}{dx} \cdot \frac{t}{\cos \theta} = \frac{\Delta E'}{\cos \theta}, \quad (3.3)$$



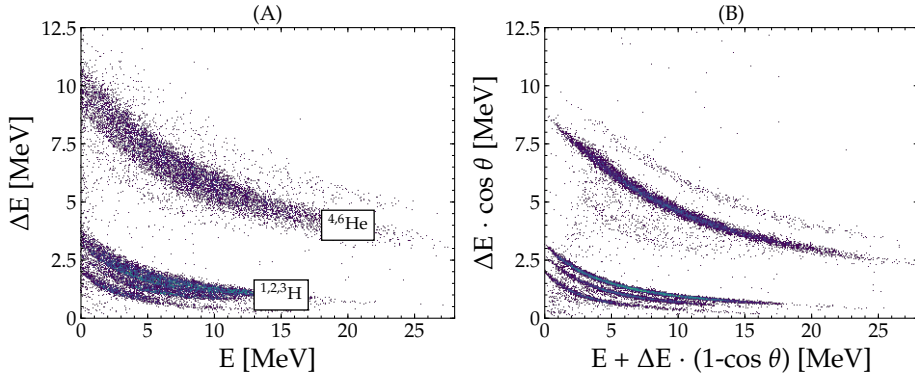


Figure 3.5: Energy correlation plots for a silicon telescope. Panel (A) shows the energy deposited in the thin detector versus the energy in the back detector. Panel (B) shows have made the geometrical correction described in Eq. (3.4) to obtain a better resolution.

where  $\Delta E'$  is the corresponding energy loss if the particle had entered the front detector orthogonally. With this correction, we get an improved  $\Delta E - E$  spectrum.

The remaining energy is deposited in the back detector, and the total correction is

$$\begin{aligned} dE' &= dE \cdot \cos \theta \\ E' &= E + dE \cdot (1 - \cos \theta), \end{aligned} \quad (3.4)$$

where  $E$  is the measured energy in the back detector and  $dE$  is the energy measured in the front detector and  $\theta$  is the angle between the particle and the normal of the detector. Figure 3.5(B) shows the corrected spectrum. Notice how the three particles types in the lower regions are much better resolved.



---

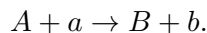
# Beam diagnostics

It is often assumed that ion beams are point-like and incident in the target at a well-known position. This is, however, rarely the case. Minimizing the emittance of the beam is a major challenge in the design and operations of accelerator facilities.

In the analysis of the experimental data, and in particular single event measurement, the energy is deduced based on the assumption that we know the geometrical profile and energy distribution of the beam. When this is not the case we introduce a bias in the analysis leading to an unnecessary decrease in resolution of excitation spectra and angular distributions.

In this chapter, I will propose a method to deduce the beam's properties from coincidence measurements of two-body reactions. The method is partly based on [54] and is developed in collaboration with Jacob. G. Johansen and K. Riisager. It has the advantage that it can be applied directly on the primary experiment of scientific interest if their coincidences are measured.

Firstly, I will present a short review of the method described in [54] followed by a description of the new method. Both are based on the same kinematical conditions as described in Section 2.1 with a beam,  $A$ , impinging on a target  $a$ , producing a beam-like recoil,  $B$  and a target-like ejectile  $b$



Lastly I will demonstrate with simulations of the reaction  ${}^9\text{Li}(\text{d,t}){}^8\text{Li}$  using a 5 MeV/A beam.

## 4.1 Old method

The azimuthal angle of the two outgoing particles is given as

$$\tan(\phi) = \frac{y}{x}. \quad (4.1)$$

In the center-of-mass frame, the two particles will move back to back, due to momentum conservation, i.e.

$$|\phi_b - \phi_B| = \pi. \quad (4.2)$$

The azimuthal angle is invariant under the transformation along the  $z$ -axis. Combining Eq. (4.1) and Eq. (4.2) yields

$$\frac{y_b}{x_b} = \frac{y_B}{x_B}, \quad (4.3)$$

which holds as long as the beam is incident in  $(0,0)$ . If it is displaced and hits in  $(x_A, y_A)$  instead, Eq. (4.3) changes to

$$\frac{y_b - y_A}{x_b - x_A} = \frac{y_B - y_A}{x_B - x_A}.$$

The offset is expected to be as small as possible, that is the minimum value of  $x_A^2 + y_A^2$ . This results in the following two relations (note that there is a sign error in the last parenthesis in [54])

$$x_A = \frac{x_b y_B - x_B y_b}{(y_b - y_B)^2 + (x_b - x_B)^2} (y_B - y_b)$$

$$y_A = \frac{x_b y_B - x_B y_b}{(y_b - y_B)^2 + (x_b - x_B)^2} (x_b - x_B)$$

## 4.2 New method

The new method calculates the momentum of the beam particles from momentum conservation in the LAB frame (the target is at rest)

$$\begin{aligned}
\bar{p}_A &= \bar{p}_B + \bar{p}_b \\
&= m_B \sqrt{\frac{2T_B}{m_B}} \hat{v}_B + m_b \sqrt{\frac{2T_b}{m_b}} \hat{v}_b \\
&= \sqrt{2T_B m_B} \hat{v}_B + \sqrt{2T_b m_b} \hat{v}_b,
\end{aligned}$$

where  $m_i$  is the mass of the particles,  $T_i$  is the measured energy of the particle in the detector and  $\hat{v}_i$  is the direction of the movement of the particles given as

$$\hat{v}_i = \frac{(x_i - x_A, y_i - y_A, z_i - z_A)}{\sqrt{(x_i - x_A)^2 + (y_i - y_A)^2 + (z_i - z_A)^2}}$$

The energy of the incoming beam is given as

$$T_A = \frac{p_A^2}{2m_A} \quad (4.4)$$

$$\begin{aligned}
&= \frac{1}{2m_A} (2T_B m_B + 2T_b m_b \\
&\quad + 2\sqrt{4T_B m_B T_b m_b} \hat{v}_B \cdot \hat{v}_b). \quad (4.5)
\end{aligned}$$

Due to energy conservation, the measured energies of the two outgoing particles should be equal to  $T_A + Q$ , i.e.

$$T_A = T_B + T_b - Q. \quad (4.6)$$

Subtracting (4.6) from (4.5) should thus equal zero. The position can be found by numerical minimization of the difference.

### 4.3 Angle determination

With the estimated displacement of the beam, using either method, we can estimate the angle. The azimuthal and polar angles are given as

$$\tan(\theta_A) = \frac{\sqrt{p_{A,x}^2 + p_{A,y}^2}}{p_{A,z}} \quad (4.7)$$

$$\tan(\phi_A) = \frac{p_{A,y}^2}{p_{A,x}^2}, \quad (4.8)$$

with projections onto the x and y-axes

$$\theta_x = \theta_A \cos(\phi_A) \quad (4.9)$$

$$\theta_y = \theta_A \sin(\phi_A). \quad (4.10)$$

## 4.4 Setup and simulation

The methods are investigated by applying them to Monte Carlo simulations done with the **simX** package[55]. To be comparable to the experiments, the simulated reaction is  ${}^9\text{Li}(d,t){}^8\text{Li}$  at 5 MeV/A. The target is modelled as deuterons in a 1 mg/cm<sup>2</sup> polyethylene target (CD<sub>2</sub>).

The setup is shown in Figure 4.1. The symmetry in the azimuthal angle  $\phi$  allows a showcase of some important features of the method which will become clear in the later sections. The DSSDs are all W1s in a telescope configuration with a pad detector.

We will refer the axis that connects the center of the two detectors for the *primary axis* of the detector pair. The reason for this will also become clear in the discussion of the results. The axis orthogonal to this axis will be called the *secondary axis*. In this setup, there are four primary axes (of interest), each pairing the central DSSD with one of the peripheral DSSD's.

As discussed in Section 2.2, the kinematic compression means that the  ${}^8\text{Li}$  is emitted at mostly  $\theta \approx 20^\circ$ . The central detector is thus mainly to measure the heavy fragments.

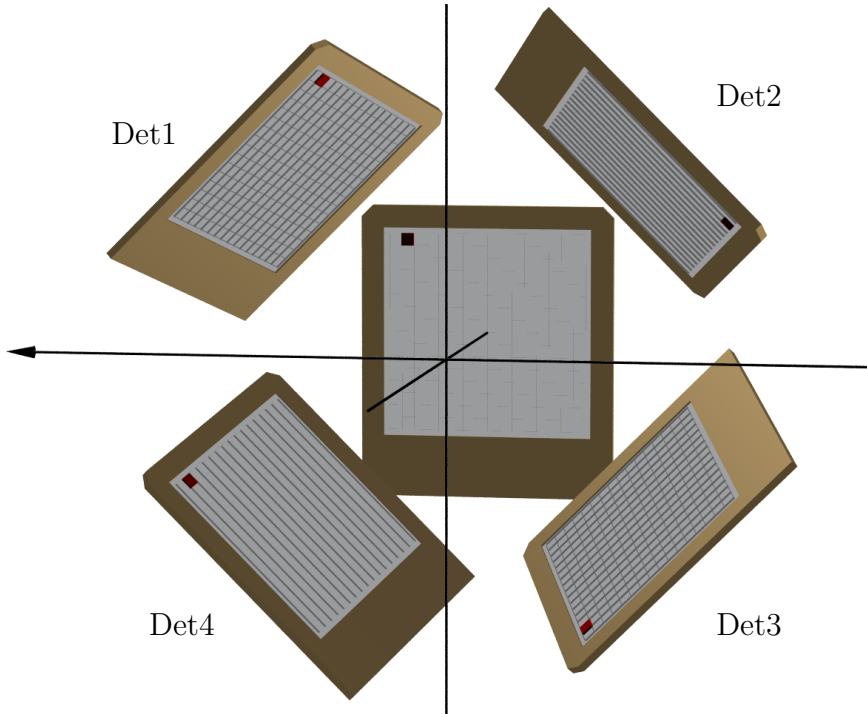


Figure 4.1: The setup used in the simulations. The four peripheral detectors are W1 types and are facing (0,0).

## 4.5 Analysis

With the new method, the offset is found for each identified coincidence by minimizing

$$0 = E_B + E_b - Q - \frac{p_A^2}{2m_A}. \quad (4.11)$$

From the offset, the corresponding angles are calculated using Eq. (4.9) and Eq. (4.10).

We start with an ideal beam and restrict us to the position estimate. After this, we continue to look at an angled beam. In real situations, the beam is both displaced and angled beams, so we will finally investigate a combination of both displacement and angling. To assess the geometrical dependencies we will then look at some of the factors that determine the accuracy. Finally, we will discuss energy distribution.

### 4.5.1 Beam position

This position estimate for an ideal beam is shown in Figure 4.2 (A). Notice that the setup structure is really pronounced. Moreover, the distribution is rather broad, it extends to approximately 15 mm in both directions, even though our target is only 10 mm in both directions. This can, however, be enhanced by noticing that Eq. (4.11) is quadratic in  $p_A$ . There may thus be one, two or zero solutions. One solution is ideal. If there is no solution it is ignored since it can not reproduce our conditions. If there are two solutions, we choose the one closest to the z-axis, assuming the displacement is as close to the z-axis as possible.

Disregarding the coincidences with no solution to Eq. (4.11) confine the estimates within approximately 10 mm, see Figure 4.2 (B). Figure 4.2 (C) shows the projections on the x-axis and y-axis, respectively. The distributions are centered around (0 mm, 0 mm) but they are so broad that it is hard to tell whether the centers of the distributions are shifted slightly.

Let us consider what is actually happening in the reaction. Each reaction spans a *reaction plane*, defined by three points: the reaction position (i.e. the beam position) and the two detected particle positions. The method estimates one of these points, namely the reaction position, based on a measurement of the two others. Ideally, the solution is the intersection of all these planes coming from all detector pairs. This is, however, not feasible since it would require an infinite resolution. Instead, we average over ensembles of measurements. We do this by defining specific planes of interest, namely the primary axes of the detector pairs, and make an averaged estimate from each of these. The intersection in the target plane will then be our estimate of the beam position.



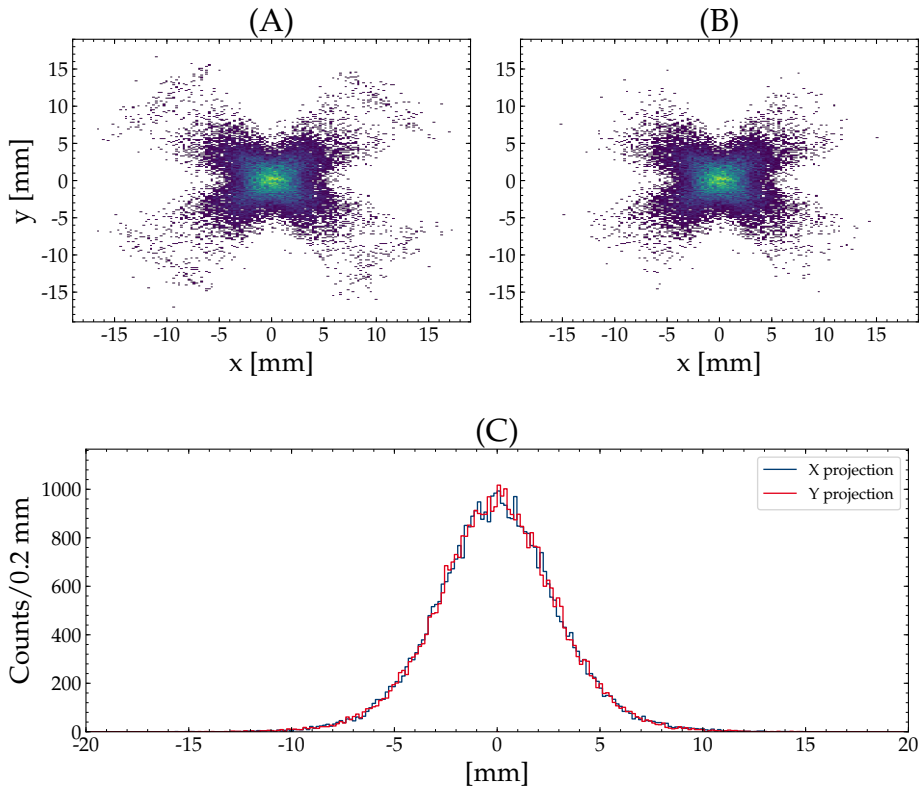


Figure 4.2: The total position distribution for all coincidence measurements is shown in (A). The total position distribution for all coincidence measurements with a solution to Eq. (4.11) is shown in (B). The projection of position distribution for all coincidence measurements with a solution to Eq. (4.11) is shown in (C).

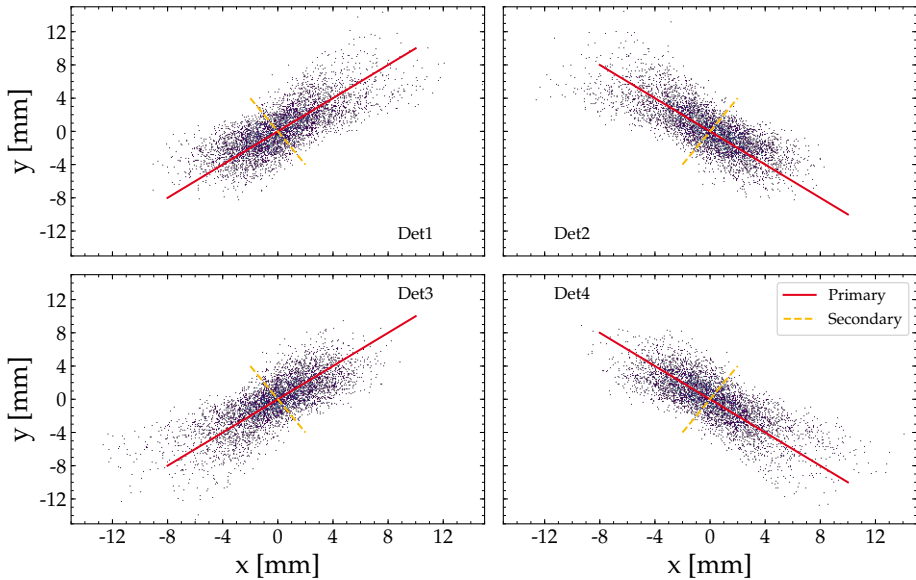


Figure 4.3: The position distributions for coincidence measurements in the central W1 and each of the surrounding W1's. The primary and secondary axes are indicated on top of the spectra.

More specifically, we plot the position estimates from the method for each detector pair separately. This is shown in Figure 4.3. Notice that the best estimate is given along the secondary axis of the two detectors. The reason for this is twofold. It is partly because of the geometry of the detector. There is "more detector" along the primary axis than perpendicular to it. The second reason is the method itself. There is much more freedom to match momenta in the reaction plane than its perpendicular plane. This is due to the minimization criterion. A projection onto the primary axis and the secondary axis shows this effect, see Figure 4.4.

To make an averaged estimate over the ensemble, we fit a straight line with a fixed slope (the primary axis) for each of the pairs. This gives an

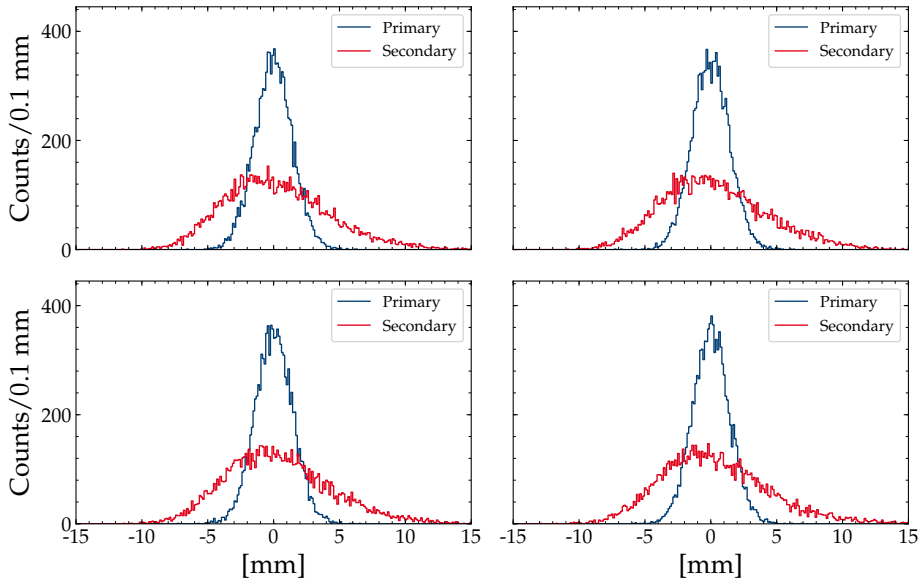


Figure 4.4: Projections of the position distributions for coincidence measurements in the central W1 and each of the surrounding W1's. The projection is on to the primary and secondary axis.

estimate of the displacement along the secondary axis and constitutes the first estimate; the reaction took place somewhere on that line in the targets xy-plane. Repeating this for each detector pair, it is evident that their intersection is very close to the origin, see Figure 4.5 (A). The intersection thus estimates the position of the beam can is found by minimizing the sum of the square of the distances to each line, yielding (0.02 mm, 0.01 mm).

The result of a displaced beam, (1 mm, 1 mm), is shown in Figure 4.5 (B). The displacement is estimated to be (0.99 mm, 0.98 mm). The method thus gives a good estimate of the displacement.

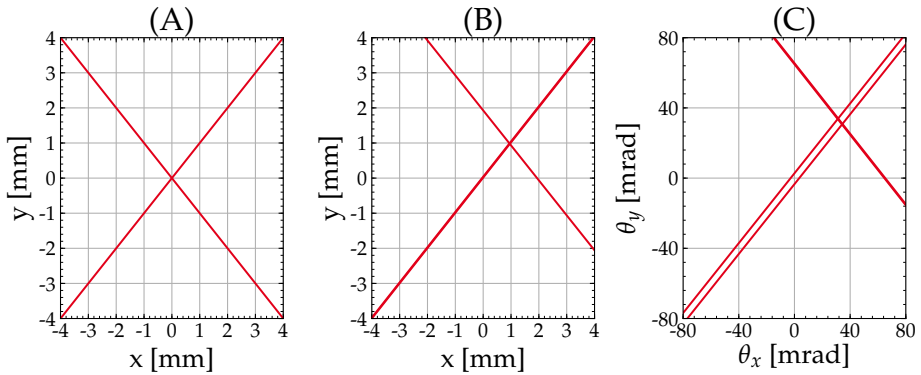


Figure 4.5: The position estimate for a beam incident in (0,0) and (1,1) is shown in (A) and (B) respectively. The angle estimate of a point beam incident in (0mm,0mm) but angled ( $\theta_x = 35.3 \text{ mrad}$ ,  $\theta_y = 35.3 \text{ mrad}$ ) is shown in (C).

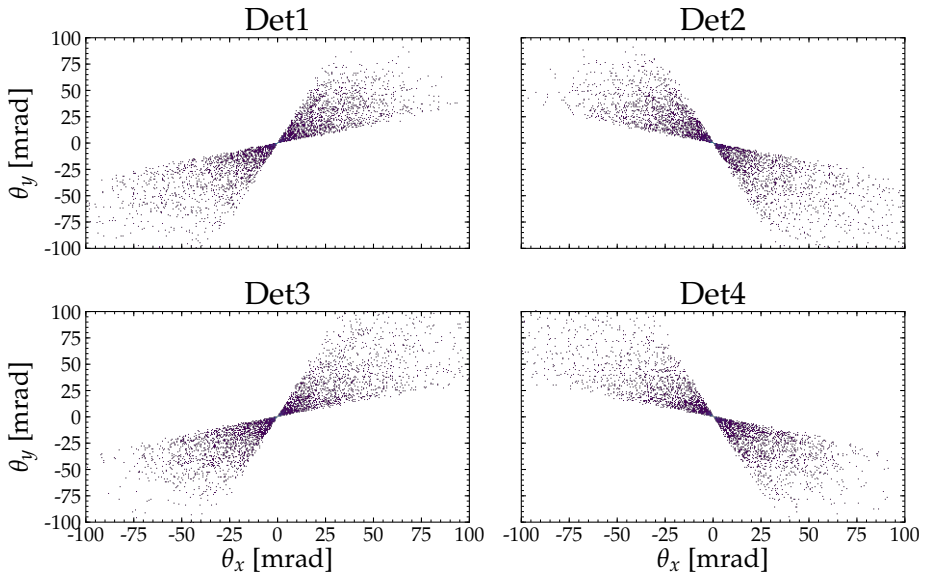


Figure 4.6: The angle distributions from the new method. There are many counts in (0,0), meaning the method is rather insensitive to coincidences angled in the reaction plane. This means we should use the angle relative to the inferred reaction plane, i.e.  $\theta_x$ .

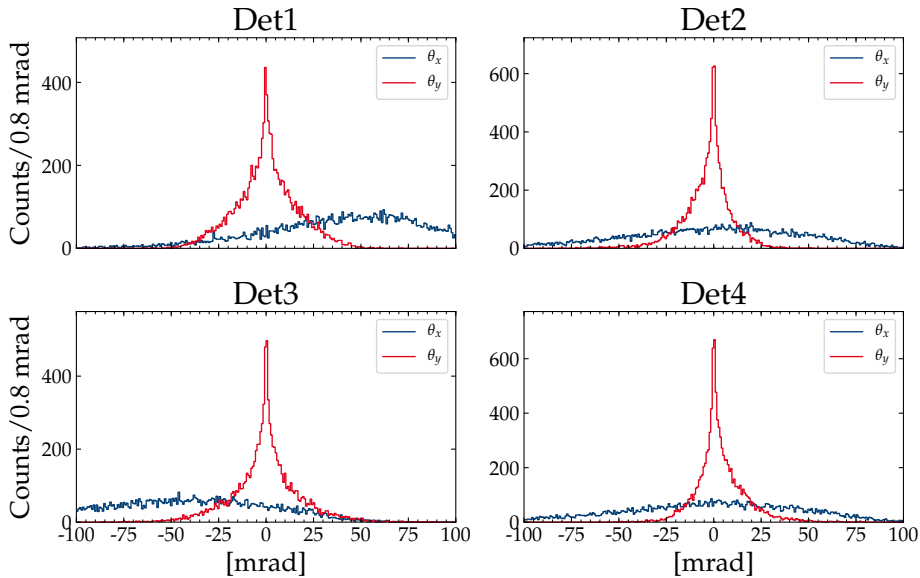


Figure 4.7: Projection of the angle distributions from the new method on an angled beam. The x-projection shifts, and can thus be used to estimate the angle of the beam.

### 4.5.2 Angled beam

As described, the angle of the beam can be calculated from from the estimated beam position and conservation of momentum. For this analysis we also isolate each detector pair. Figure 4.6 shows the angle spectrum from the detector pairs of a beam angled  $\theta = 50$  mrad and  $\phi = 45^\circ$ , i.e.  $\theta_x = 50 \text{ mrad} \cdot \cos(45^\circ) = 35.3 \text{ mrad}$  and  $\theta_y = 50 \text{ mrad} \cdot \sin(45^\circ) = 35.3 \text{ mrad}$ . Notice that many counts are located in (0,0). The method is thus insensitive to coincidences angled in the inferred reaction plane, essentially the same effect from the position estimate. This means we must look at the angle relative to the reaction plane, i.e. the angle with the local x-axis,  $\theta_x$ .

In Figure 4.7, the projections onto the primary and secondary axes are

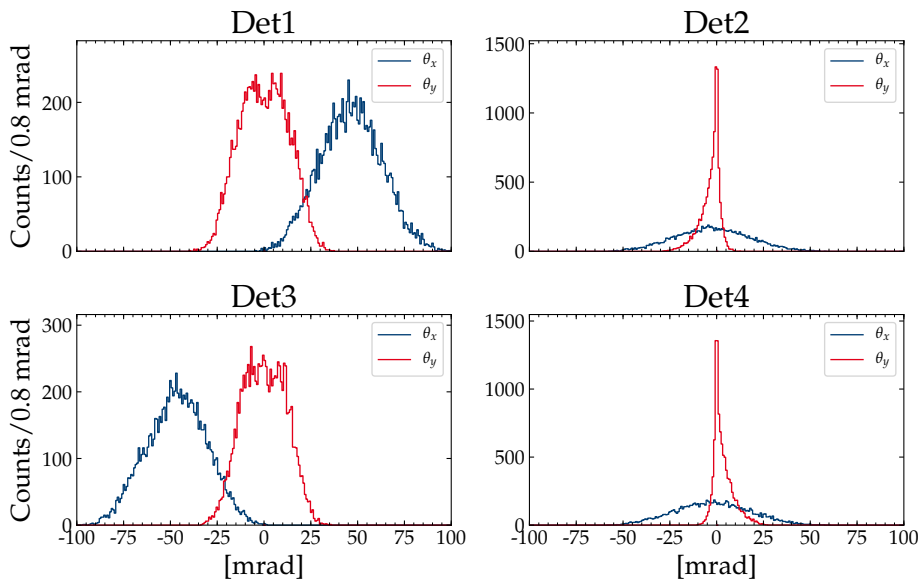


Figure 4.8: The projection of the angle distributions using the old method. We see that the x-projection shifts and we can thus use that for our angle estimate.

shown. Notice that the y-projections are mainly peaked in zero, whereas the x-projections show the same behavior as with the displacement analysis. That is, they are shifted and we can once again fit a line. This time it is, however, the axis orthogonal to the primary axis. We also note that the distributions are very broad. Gaussian fits to the x-axis give a  $\sigma$  in the order of  $\approx 45$  mrad. This is, however, expected due to the resolution of the detectors, and will be discussed in more detail later.

The old method, however, gives improved angular distributions, see the projections showed in Figure 4.8. In this case, was the displacement found using the old method, and the angles were subsequently calculated.

The x-projections are, in particular, more well defined. Fitting a straight

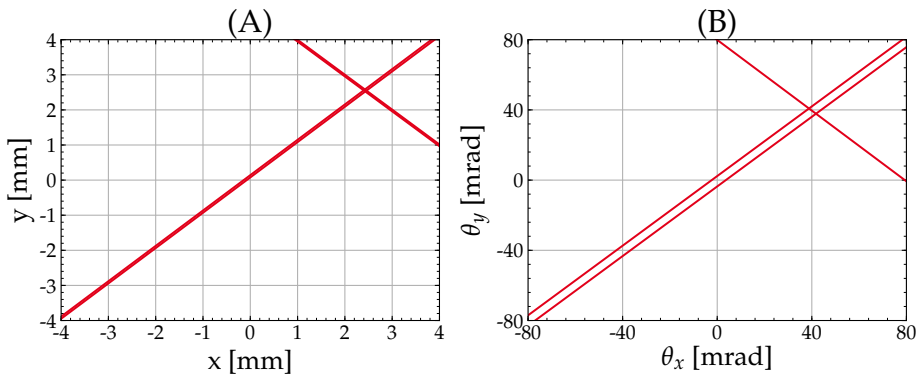


Figure 4.9: Position estimate **(A)** and angle estimate **(B)** of a beam which was both displaced and angled. We do not recreate the correct values. The method is thus biased when both effects are present.

line to these spectra instead gives an estimated intersection at (32.8 mrad, 33.0 mrad), see Figure 4.5 (C), which is a slight underestimation of the simulated value 35.3 mrad.

### 4.5.3 Combined displacement and angling

In a real experiment the beam is most likely both angled and displaced. The beam is therefore now angled with  $\theta = 25$  mrad and  $\phi = 45^\circ$ , resulting in  $\theta_x = \cos(45^\circ) \cdot 25$  mrad  $\approx 17.6$  mrad and  $\theta_y = \sin(45^\circ) \cdot 25$  mrad  $\approx 17.6$  mrad. The beam originates from  $(0, 0, -100)$  mm and thus hits the target at  $x = \tan(17.6 \text{ mrad}) \cdot 100$  mm  $\approx 1.77$  mm and  $y = \tan(17.6 \text{ mrad}) \cdot 100$  mm  $\approx 1.77$  mm.

Repeating the described analysis, using the new method to estimate the position and the old method to estimate the angle and gives the result shown in Figure 4.9. The estimates for position and angle are respectively (2.49 mm, 2.53 mm) and (40.6 mrad, 40.3 mrad).

The method can thus not distinguish between the two effects completely.

We clearly see that the beam is off, but we can not quantify it directly with good accuracy. There is thus bias in the method. In order to correct for this bias, one has to do simulations of the particular setup. By simulating different beam configurations it should be possible to converge towards the results of the analysis of the actual experiment. The beam configuration from the simulations is thus the best estimate.

#### 4.5.4 Broad beam

Typically a beam is also spatially distributed. The exact shape is due to various accelerator effects and therefore very complex. We will, however, simulate a simple spatial distribution to see how our method responds. Figure 4.10 shows the distribution of one detector pair using a beam with a radius of 2.5 mm. The position distributions get slightly broader on the secondary axis, and the angle distribution is slightly elongated on the primary axis and the methods are thus not sensitive to the beams spatial distribution. It does, however, not affect the results of the position and angle estimates. This may, however, also be due to the detector resolution.

#### 4.5.5 Resolution and spread in ensembles

As mentioned earlier, the method, in reality, analyzes possible reaction planes for each coincidence. This is what leads to the conclusion that it is most sensitive in the secondary axis when estimating position and angles. We can thus try to make the analyzed pairs "thinner". This can be done by looking at slices of the segmented detectors. That could, for instance, be only looking at the center strips of the surrounding DSSD's in the setup. In this way, we should narrow the spread in the estimates from the coincidences.

Another limiting factor is the resolution of the detectors. They can only detect particles within one pixel. This gives a positional resolution in the order of the pitch and an angular resolution in the order of  $2 \cdot \tan^{-1}(\frac{p}{2d})$ , where  $p$  is the pitch and  $d$  is the distance from the target. For the DSSD's in our setup the positional resolution is  $\approx 3.1$  mm and the angular resolution



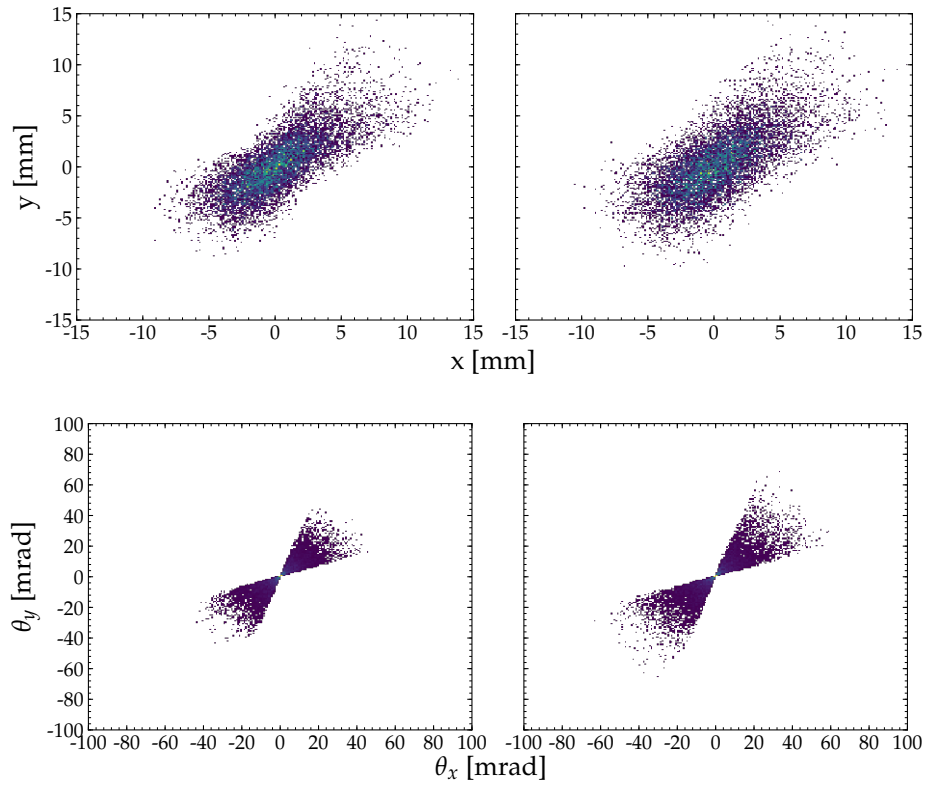


Figure 4.10: The top panel shows the position estimate for an ideal beam (left) and a broad beam (right). The corresponding angular estimates are shown in the lower panel.

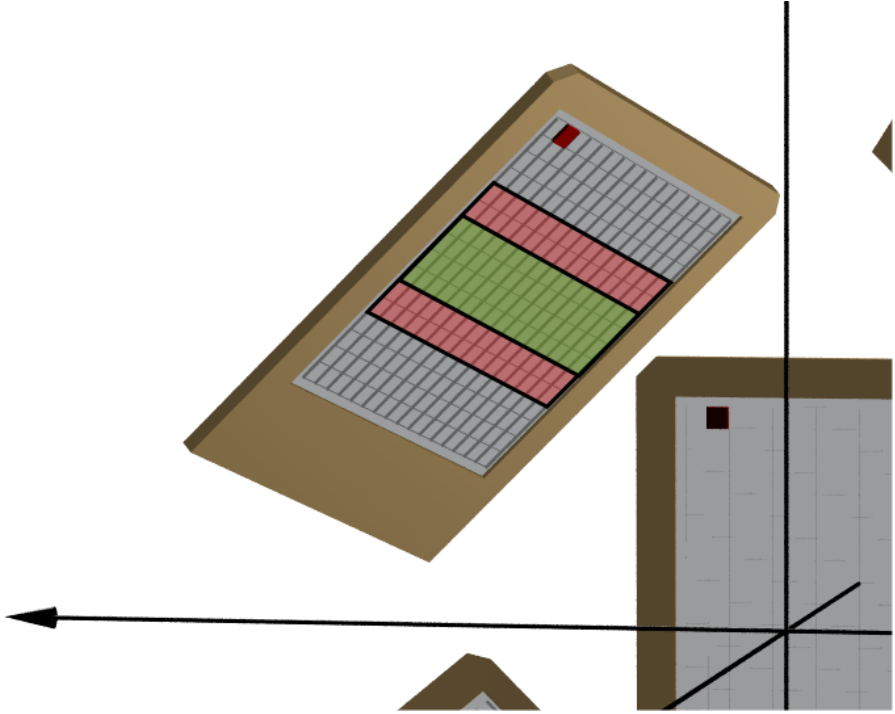


Figure 4.11: We can look narrower slices by only considering the center half (the red and green area) or the center fourth (the green area).

is  $\approx 100$  mrad. Detectors with a better resolution should give a lower the spread in the estimates.

To investigate the effect of looking at narrower slices, we perform the analysis only using the center half and the center quarter of the back strips of the surrounding detectors as sketched in Figure 4.11.

To investigate the effect of better resolution, the simulation and analysis is repeated with a setup with DSSDs detector with 2 mm pitch and 32x32 strips. The results are given in Table 4.1.

An increased resolution is in particular preferred since it decreased the spread in both position and angle. Looking narrower slices decreases the

		$\sigma_{\theta,\text{new}}$	$\sigma_{\theta,\text{old}}$	$\sigma_{xy}$
W1	Full	42.9 mrad	15.8 mrad	1.38 mm
	Half	46.7 mrad	16.0 mrad	1.15 mm
	Fourth	49.9 mrad	15.5 mrad	1.10 mm
BB7	Full	28.6 mrad	9.96 mrad	1.01 mm
	Half	31.2 mrad	10.5 mrad	0.79 mm
	Fourth	32.9 mrad	10.6 mrad	0.70 mm

Table 4.1: The sample deviation of a coincidence measurement, using either the whole outer detector, only the center half or only the center fourth. The first column shows the results for angle estimates based on the new method. Second column shows the angle estimates with the old method. The third columns shows the result from the position estimates using the new method. Furthermore, this is tested with two types of detectors with different resolution. The main improvement is due to higher resolution detector.

position, but not as much. We do, however, see that the spread in angle increases. This means we need to do slices in the other direction if we want it to narrow the angle interval.

#### 4.5.6 Energy distribution

The energy distribution of the beam can be calculated from the position and angle estimate. For each coincidence, the energy is calculated using Eq. (4.5). Figure 4.12 shows the results for a point beam, a gaussian shaped energy distribution with  $\sigma = 250$  keV and a gaussian shaped energy distribution  $\sigma = 1$  MeV, respectively. Applying a Gaussian fit get the results in Table 4.2. They are very close to the simulated values. We can thus accurately determine the beam energy distribution from coincidence measurements.

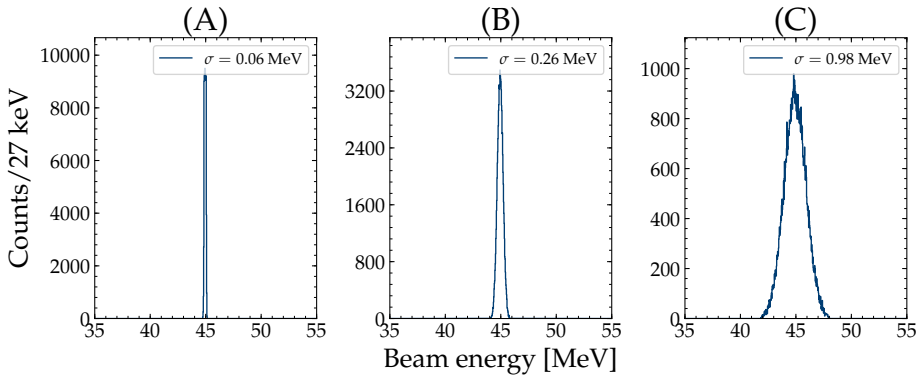


Figure 4.12: Energy resolution for an ideal beam (A), a beam with  $\sigma = 250$  keV (B) and  $\sigma = 1$  MeV (C).

	$\mu$	$\sigma$
Point	44.9 MeV	0.06 MeV
$\sigma = 250$ keV	44.9 MeV	0.26 MeV
$\sigma = 1$ MeV	44.9 MeV	0.98 MeV

Table 4.2: The deduced energy distributions of three beams with different energy distributions.

## 4.6 Conclusion

The proposed method can estimate a beam's properties and in particular estimate a displacement and angling of a beam using coincidence measurements in segmented detectors. The method can not, however, distinguish between the effects. One can, however, use simulations of the setup to find the beam that yields the same results as the analysis of the actual experiment. In order to get the best intersection estimates, we need multiple different primary axes. The setup should thus cover multiple directions in the azimuthal angle. Four detectors are for instance sufficient.

In IS367 the detector coverage was not sufficiently good to use the methods. The methods was, however, important to guide the design for IS561A and IS561C, but due to low statistics it was ultimately not applied.



---

# AUSALib

The Aarhus subatomic group is involved in many experiments, both in house and at various international facilities such as ISOLDE, MSU, and Jyväskylä. The experimental setups are typically similar with multiple DSSDs, pads and telescope configurations. The initial steps of an analysis are therefore also similar.

Firstly, the raw data files are *unpacked* into a more suitable data format, with ADC and TDC values mapped to the corresponding detectors. An energy calibration is then applied and a *matching* step is performed for the double-sided detectors that pair hits in the front and backside of the detector. The geometry of the detectors in a global coordinate system must be laid out, in order to calculate positions and angles for the individual hits.

These are some of the tasks that every analysis starts with. To streamline this process and make it less error-prone, a common analysis library has been developed to perform some of these tasks, the Aarhus University Subatomic library (**AUSALib**). It is written in C++ and is built on top of ROOT [56]. The development began before I started working in the group by M. Munch, O. Kirsebom and A. Howard. During my PhD I contributed substantially to the development of this project.

## 5.1 Geometry

A core feature of **AUSALib** is the generalization of geometrical properties of the detectors. When a particle hits a double-sided detector, the front strip and the back strip is recorded in the data stream. This translate to a

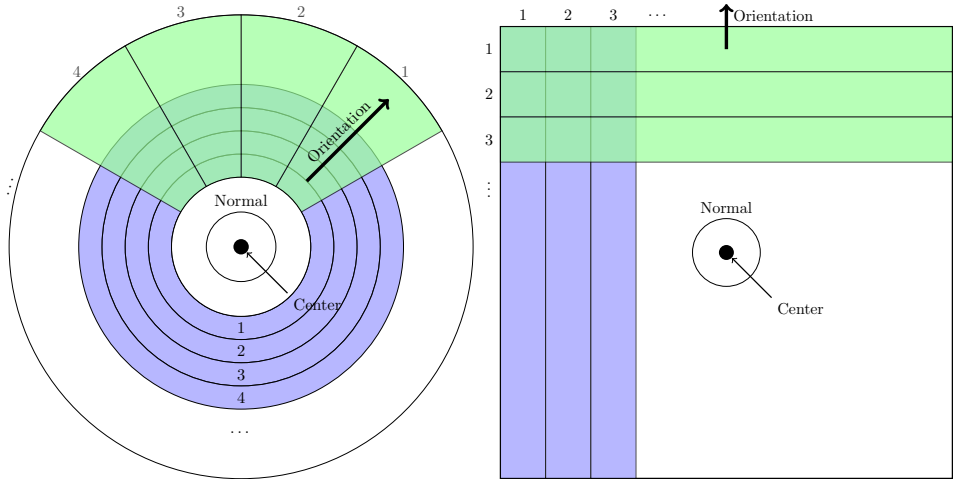


Figure 5.1: Geometry for a round DSSD and a square DSSD. Each type have orthogonal front and back strips. Figure courtesy by M. Munch[57].

position in space, but the transformation depends on the specific geometry and position of the DSSD.

Figure 5.1 shows two very different geometries that can still be described with orthogonal front and back strips. The interface in the analysis is thus the same - given a front strip and a back strip, calculate a position. A single superclass can thus expose the interface for many types of DSSDs, and concrete implementations, such as the round DSSD, can specify the exact transformation. For the experiments in this thesis, we can use the square DSSD class to describe both the **W1** and the **BB7**, whereas we can describe the **S3** with the round DSSD class.

Even more general is the position and orientation in space. This is required for all types of detectors, segmented or unsegmented, in order to place them in a global coordinate system and rotate them correctly. This leads to a class hierarchy as shown in Figure 5.2.

This approach has two main advantages. Firstly the data is decoupled from the geometry in the sense that a hit only specify the segments that were



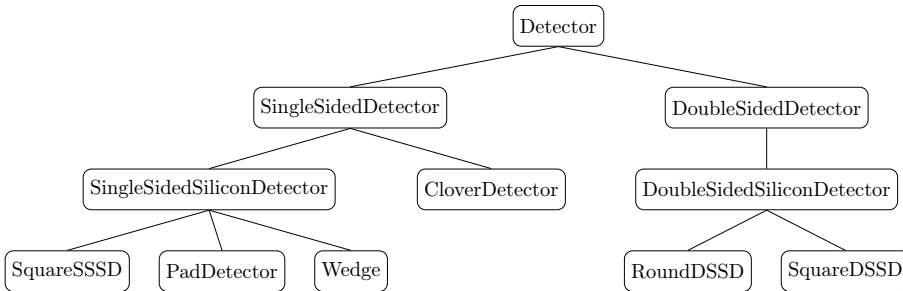


Figure 5.2: Detector hierarchy in **AUSALib**. Figure courtesy by M. Munch[57].

hit, i.e. the strips. Then it is up to the concrete detector implementation to calculate what position this corresponds to. Secondly is it easy to add new detectors. It just a matter of implementing the correct transformation, and then it can be used in an existing analysis through the common interface. This favors code reuse and modifications are done by addition, keeping the codebase backward compatible.

### 5.1.1 Setup file

For a given experiment the position and type of the different detectors must be specified to the analysis. To ease this process, **AUSALib** uses a *setup file*. This file contains all the geometry specific details for each detector, as well as which detectors are included in a telescope configuration. It is written in a human-readable format **JSON** and is therefore easy to modify. An example of the description of a detector is shown in Figure 5.3. Each detector has a name. The "**file**" contains details such as detector type (from the detector hierarchy), number of strips, dead layer thickness, etc. The "**calibration**" file contains calibrations for each strip. The "**position**", "**normal**" and "**orientation**" specify the position and orientation in the global coordinate system. The data mapping to the unpacked files are described in "**frontmapping**" and "**backmapping**".

Once such a file is written, typically during the setup of an experiment, it can be used throughout the analysis and even in the online analysis. **AUSALib**

```
1 {
2   "name": "Det1",
3   "file": "DSSD1.json",
4   "calibration": "Det1.cal",
5   "position": {"x": "-4mm", "y": "-42.0mm", "z": "39.0mm"},
6   "normal": {"x": "0.0mm", "y": "1.0mm", "z": "0.0mm"},
7   "orientation": {"x": "0.0mm", "y": "0.0mm", "z": "1.0mm"},
8   "frontMapping": {
9     "multiplicity": "DET1F",
10    "segment": "DET1FI",
11    "adc": "DET1F_E",
12    "tdc": "DET1F_T"
13  },
14  "backMapping": {
15    "multiplicity": "DET1B",
16    "segment": "DET1BI",
17    "adc": "DET1B_E",
18    "tdc": "DET1B_T"
19  }
20 }
```

Figure 5.3: An example of a detector description in an **AUSALIB** setup file. It describes properties such as the global position and orientation, the data mapping as well as the location of the calibration file.

simply loads this file making it easy to make changes without having to recompile a large analysis codebase. Moreover, the full geometrical details are contained in a few files that can easily be shared with collaborators.

## 5.2 Energy loss

From the reaction site to the detection site, a particle may lose energy in inactive material such as dead layers or target components. These energies are not measured, so they must be corrected for. Such energy losses have

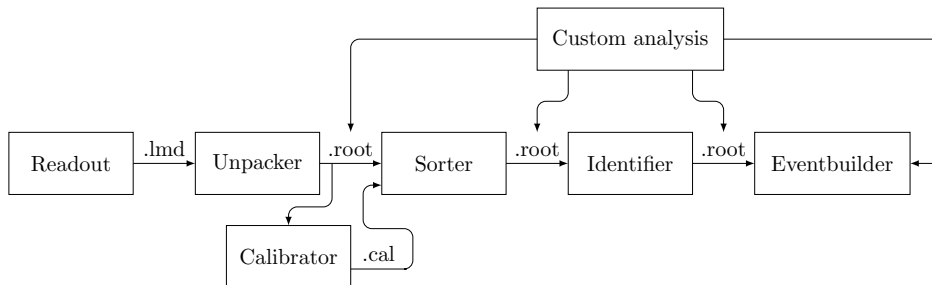


Figure 5.4: The analysis pipeline for **AUSALib**. The data are unpacked from the readout and are sent through several steps of increased sophistication. Between each step, it is possible to perform custom analysis.

been tabulated for a large number of charged particles in different materials and **AUSALib** includes tables from GEANT[58], ICRU[59] and SRIM[60].

### 5.3 Analysis pipeline

A key operating principle in **AUSALib** is the idea of an analysis pipeline. The data starts out as raw data and the is piped through a series of steps which increases the level of abstraction. The data is thus transformed from ADC and TDC values to observables quantifying physical events.

The pipeline is shown in Figure 5.4 and the steps will be described in more detail in the following. Each step outputs **ROOT** files with **TTree** objects that can be investigated directly in **ROOT** or via custom written analysis program using the **AUSALib** infrastructure. This is useful to make consistency checks along the way. The **setup**-file is used in every step of the pipeline. This keeps the geometry and detector specifications consistent throughout the pipeline.

### 5.3.1 Unpacking

The data acquisition (DAQ) saves the files in a GSI list mode format (.lmd). The first step is to convert these files to ROOT files that can be read into the rest of the **AUSALib** pipeline. This is done with **ucesb** [61]. The user is required to make a precise specification of which modules are used, how the data is laid out in the data stream as well as the mapping from the individual ADC channels to the detector segments. Typically this is done during the setup of the DAQ, such that it can be used during the experiment and in the subsequent analysis. One major strength of **ucesb** is that it checks that every single bit in the data is consistent with the data layout of the modules. If the file unpacks, the data is not corrupt.

### 5.3.2 Energy calibration

The first task after the unpacking is to energy calibrate the detectors. In the ISOLDE experiments we used an  $\alpha$ -source with  $^{244}\text{Cm}$ ,  $^{241}\text{Am}$ ,  $^{239}\text{Pu}$  and  $^{148}\text{Gd}$  which all give well defined nearly monoenergetic peaks. The source is placed in a well-known position. The energy response in a silicon detector is highly linear. The relationship can be found by fitting a linear relationship between the ADC channel corresponding to the centroid of the peak and the well known tabulated energy. There are, however, a few small corrections required to get a better calibration.

#### Deadlayer

There is a small dead layer on both sides of a silicon detector. This is a small layer of inactive material. The  $\alpha$ -particle loses energy, but the created electron-hole pairs are not collected. This means the measured energy is slightly lower than the actual energy

$$E' = E_\alpha - \frac{dE}{dx} \frac{\Delta t}{|\cos \theta|}, \quad (5.1)$$

where  $\Delta t$  is the thickness of the dead layer,  $\theta$  is the angle shown in Figure 3.4 and  $E_\alpha$  is the tabulated  $\alpha$  energy. The dead layer is assumed to be

so small that the energy loss is constant. It is thus important that the geometry of the detector as well as the source position is known, so  $\theta$  is calculated properly.

### Shift calculation

Each segment is calibrated individually but extends over many angles. The measured energies should, therefore, be averaged over the full surface of the segment. Since the positional resolution is limited by the pixels the average can be approximated with a weighted average weighted by the solid angle of each pixel

$$E' = E_\alpha - \sum_{\text{pixel}} \frac{dE}{dx} \frac{\Delta t}{|\cos \theta_{\text{pixel}}|} \frac{\Omega_{\text{pixel}}}{\Omega_{\text{strip}}}, \quad (5.2)$$

where  $\theta_{\text{pixel}}$  is the angle at the center of the pixel.

Since there are many strips that have to be calibrated, **AUSALib** provides a calibration tool, the **Calibrator**[62]. It implements a peak-finding algorithm to find peaks, perform the correction from (5.2), perform a linear fit and display the result to the user. The user can then quickly browse through and check the calibrations. If the algorithm misidentified a peak, the user can easily specify which peaks correspond to the different energies for that specific segment and redo the calibration. This significantly reduces the time to calibrate several hundred segments.

### 5.3.3 Sorting

The sorting step has two main jobs and is performed by a general-purpose tool, the **Sorter**[63]. Firstly it applies energy calibrations. These can come from the **Calibrator** as described above, or other means of calibration. However, only linear calibrations are implemented.

Secondly, it performs *matching* to determine which pixels were hit by a particle. When a particle hits a DSSD a signal is detected in both sides. If there is only one hit in the backside and one hit in the front side they must match. If, however, there are more than one hit in one or both sides

it must be decided which pairs that match. There might also be noise that only shows up on one side.

The *Sorter* implement a greedy algorithm that computes the difference between all pairs. The pair with the smallest difference is selected as the first pair and those hits are excluded from the pool of candidates. The next pair is now the pair with the smallest energy difference from the remaining hits. This continues until there are no more pairs with an energy difference below a certain threshold.

The majority of hits will hit a strip in both the front and the back, but a minor part will hit in an interstrip region. This results in a *sharing* of the energy between two strips. It is also possible that multiple particles hit the same front strip but different backstrip and we see a *summing* of the energies. Neither of these situations can be handled by the basic greedy algorithm, but they can mostly be recovered by a more sophisticated algorithm that considers all pairs and tries to reconstruct both normal hits, sharing and summing.

### 5.3.4 Identification

After the sorting, the energy and the position of the hits are determined. This enables the next step, which is trying to identify what particle a given hit corresponds to. There are different techniques to perform this identification. When the detectors are organized as telescopes the  $\Delta E - E$  method is very useful to separate the different isotopes. If the energy is too low to penetrate the  $\Delta E$  detector, it may be possible to exclude some particle types simply based on how much energy they lost in the detector. This is, however, not unambiguous, and a hit can have several candidate identifications. Based on each of these identifications, the energy is corrected for energy loss in dead layers and the target.

The identification and energy loss is performed by another tool, the **Identifier**[64]. It requires details on the target and the particles to look for, which are supplied either as a command-line argument or through simple text files.

### 5.3.5 Eventbuilding

From the files with identified particles, the event building stage attempts to reconstruct physical events from the detected hits. It requires one or more final states to look for or reconstruct. Consider elastic scattering of deuterons on  ${}^9\text{Li}$ . If an event contains an identified deuteron as well as a hit that is consistent with a  ${}^9\text{Li}$ , the four-momentum for both is computed based on the position of the hit and the energy in the detector. If only a deuteron is detected it can try to reconstruct the four-momentum of the  ${}^9\text{Li}$  based on the initial four-momentum of the beam and the target.

A user-supplied analysis can subsequently perform the final analysis based on the four-momentum and particle identifications. This includes extraction of excitation energies, CM angles, particle correlations, etc.





---

# Data acquisition

The data acquisition system (DAQ) is an essential part of any experiment. The DAQ is loosely speaking the set of electronic modules and software that converts the incoming signals from the detectors to files on a computer that can be analyzed. We will divide the description into two main parts, the backend, and the frontend. A schematic overview of the essential parts in the DAQ is shown in Figure 6.1.

The frontend handles amplification and digitizing of the analog signals from the detectors as well as for deciding which signals are worth saving (discrimination).

The backend receives the digitized data and is first and foremost responsible for storing the data. Moreover, the software should give the operators of the experiment some degree of control and monitoring such as a preliminary online analysis.

The bridge between the two is the readout that extracts the data from the modules and transfers it to the backend. The different components will be described in more detail in the following sections.

During my Ph.D. I took part in the setup of the DAQ in IS561A and set up the majority of the DAQ for IS561B and IS561C. With guidance and help from M.Munch and H.T Johannson, I designed and implemented a two-crate system for IS561C. During the development of such a system, I contributed proportionally to the paper "VME Readout at the conversion limit" [65]. In this chapter, I will discuss the main principles of the data acquisition system. For more details and a quantitative description of the performance, the reader is referred to the paper.

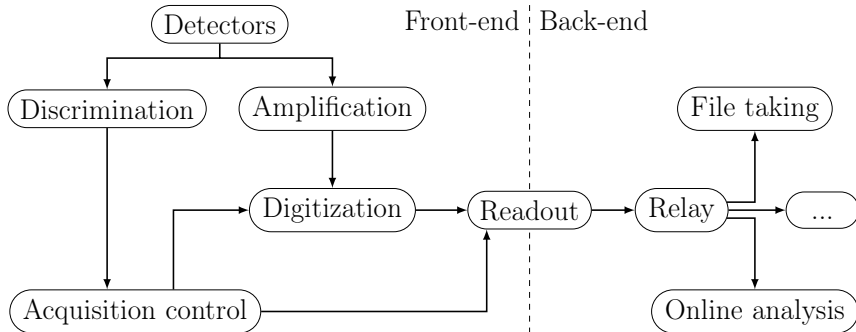


Figure 6.1: A schematic overview of the components in the DAQ. The frontend consists of the hardware and electronics which is partly inside the chamber or close by. The backend consists of the components that handle the file taking and the interface to the operators. Figure courtesy by M. Munch[66].

## 6.1 Triggers and acquisition control

In a nuclear physics experiment, the reactions happen randomly and we do not know precisely when to look to capture the result. Instead, the decision must happen as the reaction happens, i.e. the detection system should *trigger* on signals of interest. This is typically implemented based on the amplitude of incoming signals. For now, we will limit our discussion to the simplest mode of operation, the *single cycle* mode. We will discuss more sophisticated readout modes in.

When a trigger arrives, the acquisitions must digitize the signal and transport it to storage. Our DAQ runs in a synchronized mode, meaning that when a trigger arrives, no matter which module generated it, the whole DAQ starts digitizing, and are subsequently emptied to storage. During this time, the system is *busy*. This means that it can *not* accept new triggers. We will refer to the time period where it is busy as the dead time (DT) and the time where it can accept new triggers the live time (LT).

With an experimental setup that easily has  $\geq 200$  channels, it is impor-

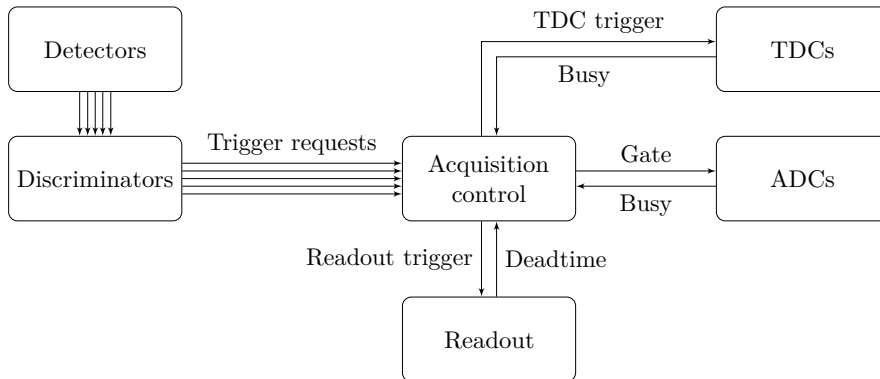


Figure 6.2: A schematic overview of the AcqC. It receives trigger requests from the input sources and generates a **MS**, **GATE** and **TDC trigger**. When the system is busy or the readout is in **DT** it rejects new trigger requests. Finally, does it periodically issue a readout trigger to the readout. Figure adapted from M. Munch[66].

tant to keep track of which state the DAQ is in, so it does not accept new triggers while busy. The digitization process must only be started when it is ready, otherwise, it must reject the trigger. This *acquisition control* (AcqC) is implemented with a VULOM 4b module[67] running the TRLO II firmware[68]. A schematic overview of the AcqC is shown in Figure 6.2.

The AcqC gets trigger requests from all input sources, i.e. the detectors. If the DAQ is ready, the AcqC generates a **MASTER START (MS)** that is sent to the digitizing modules. This is a logical signal that tells the digitizing module to start digitization. During this process, they assert a logic **BUSY** signal which is monitored by the AcqC.

As long as any module has asserted **BUSY**, the AcqC will not accept new triggers. The readout software also requires time periods to check that all modules agree on the number of events they have digitized. If they disagree, there is a fatal flaw somewhere that needs to be addressed immediately. During these times, the DAQ can also not accept new triggers.

After the digitization process has finished, the event is stored in the

modules. Before the DAQ is ready for the next trigger, the readout reads the event from the module and transfer it to storage.

Notice that emptying the module after every event is only done in single cycle mode. Most modules have an internal buffer and can store multiple events before the readout needs to empty the module. This saves some overhead time and thus reduce the DT. An even more sophisticated method is gradually emptying the modules while the readout is otherwise idle. These different modes, are described in Section 6.5.

## 6.2 Analogue chain

The ionization from a charged particle creates a small signal in a silicon detector. A 9 MeV particle will, for instance, give rise to a charge of 0.3 pC. This charge production is converted into a voltage signal in a pre-amplifier which, as the name suggests, amplifies the signal. This amplification is done close to the detector to minimize noise pickup. The amplified signal has a fast rise time with a long exponential tail and is sent into a second combined amplifier and signal discriminator. The signal is further amplified and bandwidth limited, producing an approximately gaussian signal with FWHM=1  $\mu$ s – 2  $\mu$ s. The discriminator produces a logic signal if the signal passes a certain condition. We use both *constant fraction* and simple *leading edge* modules. For each channel, a shaped energy signal is produced and sent to an ADC. The logical discriminator signal from each channel is sent to the TDC. Furthermore, the logical **OR** from blocks of 16 channels is produced, and this is used by the trigger logic.

### 6.2.1 ADC

To measure the energy we use peak sensing Analog-to-Digital converters. They charge a capacitor internally to capture the maximum peak. This integration period is, however, decided externally. In our experiments, this is done by the AcqC that sends a logical **GATE** signal. After this period the module converts the capacitor value and stores it in a buffer. During this time it asserts its **BUSY** to tell the AcqC to wait. If the buffer gets full it can

not accept new events and will assert its **BUSY** while waiting to be emptied. The **GATE** should be wide enough to capture the peak of the signal. For charged particles in a silicon detector, the width of the shaped signals is a few  $\mu\text{s}$ , and the **GATE** is adjusted accordingly.

Both IS561A and IS561B was implemented with CAEN 785[69]. They have a  $7\ \mu\text{s}$  conversion time and 32 event buffer. In the IS561C they were exchanged with MESYTEC MAD32[70] from two different revisions. Both have a faster conversion time of  $1.2\ \mu\text{s}$ . The newer revision has a significantly deeper buffer with a worst-case capacity of 170 events whereas the older version could only store 21 events.

### 6.2.2 TDC

The leading edge from the discriminators is sent to a Time-to-Digital converter which timestamps the arrival time. For each channel, it keeps the timestamp from all leading edges it received within some time period. When it receives a TDC trigger from the AcqC it saves all channels that fired within some predefined time window.

## 6.3 Readout

The readout is responsible for reading the data from the modules, move them over the network and save to it a physical disk. The DAQ is VME-based in all cases meaning that all the modules that acquired data are housed in a VME crate [71] and the communication with the modules was via the VME bus. To empty the modules in an orderly fashion, the readout must communicate with the AcqC. When a readout is required, a readout trigger is sent to the readout and the readout reports DT while emptying the modules. The transport of the data, as well as the communication with AcqC, is handled by available DAQ frameworks and we used MBS[72] for IS561A and drasi[73] for IS561B and IS561C. The user has the following responsibilities

- Configure the modules at startup.

- Empty the module buffers when the AcqC requests it
- Verify the integrity of the data. If the data is corrupt, something is most likely very wrong.
- Check module synchronizity by comparing the module event counters with the AcqC.

These tasks are handled by the Nustar Readout Library [74] and the readout code runs on Single Board Computer (SBC), located in the VME-crate, more specifically a CES RIO4-8072 [75].

## 6.4 Multicrate

As the number of detectors increases, so does the required number of ADC channels. At one point a single VME-crate can not house enough modules and we have to use one more. This introduces the complexity of having two crates, two SBC and two AcqC to communicate. The single crate design, however, scales nicely and it is rather easy to extend to two crates running in a master/slave configuration.

Both the master and the slave crate is more or less identical to the single crate setup. Figure 6.3 shows an illustration of such a system. The trigger logic is only handled by the master. The master propagates the generated **MASTER START** to the slave crate, much like if the slave was just a module. The readout trigger is also propagated. The slave adheres to this, however, the master must respect the busy and DT from the slave. If the master crate generates a **MASTER START** while the slave crate is busy, the modules would get out of sync.

By design, the readout in each crate does not know about the other, and an event builder collects the events and merge them. The events are tagged with a crate number.

This multicrate design was used in IS561C.

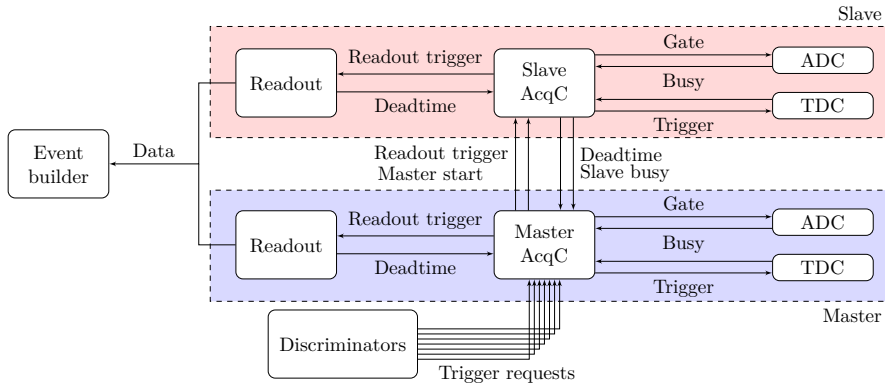


Figure 6.3: Schematic implementation of a two-crate system. One crate acts a slave and one acts as the master. Each crate is almost identical to a single crate. The master generates a **MS** and sends it to the slave. The slave reports its **BUSY** and **DT** back to the master. The data is merged in an event builder. Figure courtesy by M.Munch[66].

## 6.5 Dead time ratio

To normalize the results of an experiment, it is necessary to know the fraction of rejected events. The life time ratio  $\mathcal{L}$  is the ratio of accepted triggers to the total number of incoming trigger and the dead time ratio is the ratio of rejected triggers to the total number of incoming triggers

$$\mathcal{L} = \frac{N_{\text{acc}}}{N_{\text{tot}}}, \quad (6.1)$$

where  $N_{\text{acc}}$  is the accepted number of triggers and  $N_{\text{tot}}$  is the total incoming number of triggers. These numbers are recorded by the AcqC for each trigger input which in all three experiments corresponded to one detector. Throughout the analysis, this is used to correct for dead time, by dividing the actual count number in a given detector by  $\mathcal{L}$ .

If a stream of Poisson distributed trigger the life time ratio can also be

evaluated analytically [76]

$$\mathcal{L} = \frac{1}{1 + f_r \Delta t}, \quad (6.2)$$

where  $f_r$  is the request frequency and  $\Delta t$  is the dead time per event.

Depending on the operational mode of the readout,  $\Delta t$  can be estimated and we will briefly discuss the basics of three such modes. The first mode is the one outlined in Section 6.1 and the two latter were used during the experiments in this thesis. The reader is referred to [65] for detailed calculations.

**Single cycle mode** When the DAQ receives a trigger it issues a **MS**. After the **GATE**, the ADC's converts the data and the readout empties the buffer and checks synchronicity. The main contributions to the total dead times are the sum of the gate, conversion time and readout time. On top of this, there is some readout overhead that adds up to a significant amount.

**Multi event mode** The readout overhead can be reduced by using the internal buffers in the modules. If we wait until the buffers are full we can effectively split the readout overhead across many events. The deeper the buffers, the bigger the advantage. The DAQ ran in this mode in IS561A and IS561B.

**Shadow readout mode** Depending on the experiment and the setup, there may be times where the readout is completely idle. Instead of sitting idle the readout could continuously request data from the modules to keep the buffers as empty as possible. If the events come in at a slower pace than the readout can empty the buffers, a continuous readout effectively removes the dead time associated with readout, including the overhead. This was implemented by M. Munch after the idea of H. T. Johansson [77] and was used in IS561C.



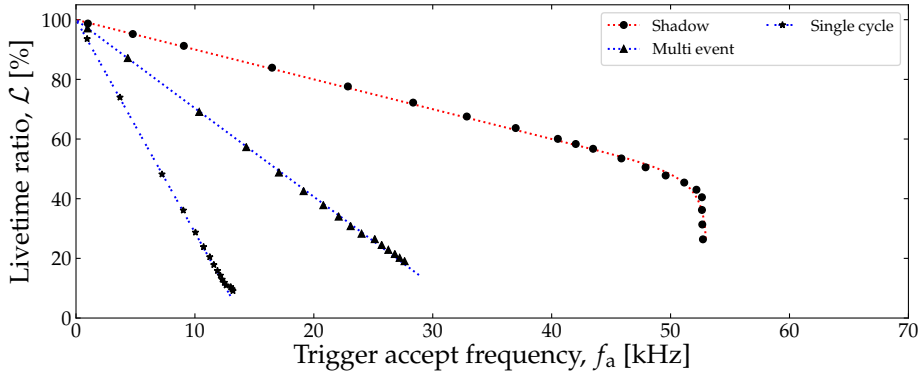


Figure 6.4: Live time ratios shown for three different readout modes. The shadow readout mode can handle much larger accept frequencies than the two others, resulting in more data. This is a simplified version of Figure 9 from [65].

In particular, the last scheme gives large improvements of  $\mathcal{L}$ , and in particular for large trigger frequencies. A simplified figure from [65] is shown in Figure 6.4. The three different schemes are calculated with Eq. (6.2) for a crate with six CAEN V785s and a RIO4 SCB. The reader is referred to the paper for the technical details. The data points are generated with a Poisson distributed pulser. The shadow readout mode performs significantly better, especially for large request frequencies. Close to 55 kHz the curve drops - this is the data bandwidth limit. The DAQ can simply not move data faster over the VME bus. For a typical ISOLDE reaction experiment, the rate is much lower. At 20 kHz the accepted trigger rate is increased by roughly 30 %, which is not an unrealistic rate in a down stream detector where Rutherford scattering dominates.

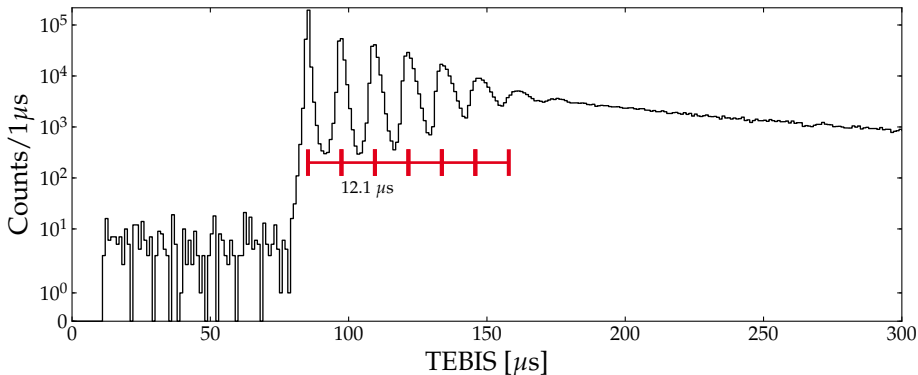


Figure 6.5: **TEBIS** spectrum from a downstream detector in IS561B. The time period between the peaks corresponds to the effective DT of the DAQ. The main contribution is the **GATE** and conversion time.

## 6.6 Pulsed beam

The major source of DT in IS561A and IS561B was the combined **GATE** and conversion time. With CAEN ADC's this adds up to  $\approx 12 \mu\text{s}$ . The challenge with a pulsed beam is, however, that the majority of our events comes in a rather short timespan. As discussed in Section 3.1.1 the EBIS releases the majority of its events in the first  $100 \mu\text{s}$ . The **GATE** and conversion thus take 10% of the time. This leads to a significant  $\Delta t$ . At high rates, the DT increases due to conversion. Figure 6.5 shows an EBIS time spectrum from a measurement with a high rate  $^{12}\text{C}$  beam, and it has very clear dips with a spacing corresponding to the effective conversion time. During the experiment, we monitored  $\mathcal{L}$  regularly.

For IS561C the CAEN ADC's were exchanged with MESYTEC ADC's to reduce the conversion time from  $7 \mu\text{s}$  to  $1.6 \mu\text{s}$ . The deeper buffers also made sure the DAQ could accept a full EBIS release without having to be emptied. To be sure that the modules were mostly empty at the beginning of an EBIS release, a readout trigger was produced at a fixed time interval

before the EBIS pulse. With a 30 Hz release cycle there is approximately 30 ms between each release which is plenty of time to empty the buffers.

With the lower intensity  $^9\text{Li}$  beam we experienced no major issues with the dead time. In the detectors of interest we had a dead time ratio in the order of 5 %-10 % in IS561A and it was reduced to 1 %-2 % in IS561C.

## 6.7 Backend

When the data has been extracted from the modules, it is sent across the network to be stored on a physical disk (file taking) as well as online analysis. The file taking is naturally the most essential feature. The online analysis is, however, very important to continuously monitor the different detectors, but it is not essential to be up at all times. There might also be other services that monitor the data in real-time which are not essential.

The majority of the backend services runs on a desktop computer that is connected to the same network as the readout node. To decouple these services, there is a *relay* service between the readout and the consumption of the data.

### 6.7.1 Relay

The relay is implemented as an `ucesb` [61] instance that connects to the readout data stream from and fans the data out to two streams. One data stream is in "weak-hold" mode, which means that if a client can not keep up with the data it blocks the acquisition. However, if no client is connected it will *not* hold. This is used by the file taking.

The second stream is in "no-hold"-mode and does not require the clients to consume all data. This is used for the online analysis.

The relay has the additional feature that it validates the data on the fly. This means we do not have to save data and unpack it to detect corrupt data.

### 6.7.2 File taking

The file taking is another `ucesb` instance that connects to the relay and writes the data to a file. It saves the data in the GSI list mode (`.lmd`) format [72]. It is furthermore compressed with `gzip` which also adds checksums making it easy to check a file for bit rot.

To ease the subsequent analysis, the files are written in chunks of typically 100 MB. In case of a failure, it also makes recovery easier, since all the data from a measurement are not in the possibly corrupted file.

### 6.7.3 Online analysis

The online analysis presents the incoming data to the people on shift. This is handled by the `go4cesb` project, which combines `ucesb`, `G04` [78] and `AUSALib`. `G04` provides an advanced user interface that lets the operator interact with different spectra produced by the analysis routines. The data is piped from the relay to a `ucesb` process which performs the unpacking of the data. This process is spawned by `go4cesb` and the unpacked data is subsequently piped back into `G04` as an event stream.

This design has two main advantages. The unpacker only has to be written once for both offline analysis and online analysis. Secondly, the unpacked data have the same `AUSALib`-friendly format, so it is trivial to apply `AUSALib` analysis routines in the online analysis.

The simplest analysis includes mapping the ADC channels to detector strips, applying calibrations and matching. Since this is built into `AUSALib`, this can automatically be applied to the unpacked data. More sophisticated analysis such as  $\Delta E - E$  spectra and kinematic curves can be implemented by the user, but since everything is in the `AUSALib` format, it is easy to reuse analysis components across different experiments. Such analysis components can be turned on and off in a simple configuration file.

Most of the work combining the three services was done by M. Munch, and when I started preparing for the experiments I refactored and extended the online analysis significantly, in particular with analysis plots that were for the three ISOLDE experiments.

## 6.8 DaqC

To have a fully functional DAQ all the described components must be running and continuously monitored. Since a typical experiment spans several days, non-experts should also be able to start, operate and even recover the DAQ. To ease this, we developed **DaqC**.

Internally it consists of an interface to start, stop and monitor all the different services. It implements the correct startup order and keeps track of dependencies between the different services. When started the startup sequence is executed. When all services are up and running, the internal watchdog monitors each service to check that is up and healthy. If a service crashes it tries to revive it.

When running, a user can interact via a simple web interface, as shown in Figure 6.6. It provides controls to all services managed by **DaqC** as well as a simple status report. Panel (A) shows the status shown for the different components. In panel (B) is a control panel for the trigger logic. The user can quickly include or exclude detectors in the global trigger between measurements. Panel (C) shows a simple overview of previous measurements.

Panel (D) provides a button to start measurements, i.e. start the file taking. When a new measurement is started, the user is prompted with a form to fill in a run sheet with information about the target, beam, people on shift, etc. This is saved in log file and effectively compiles a detailed measurement log. Furthermore, when a measurement is started and stopped, **DaqC** dumps the configuration of all the ADCs, TDCs, amplifiers as well as other available metadata. This is saved together with the data files. Both the data and the log files are continuously backed up to a remote storage facility in case of hardware failure.

I developed **DaqC** together with M. Munch after IS561A. It has been used for IS561B, IS561C and multiple other ISOLDE experiments and it is the current control program for the DAQ at the 5 MeV accelerator at Aarhus University.

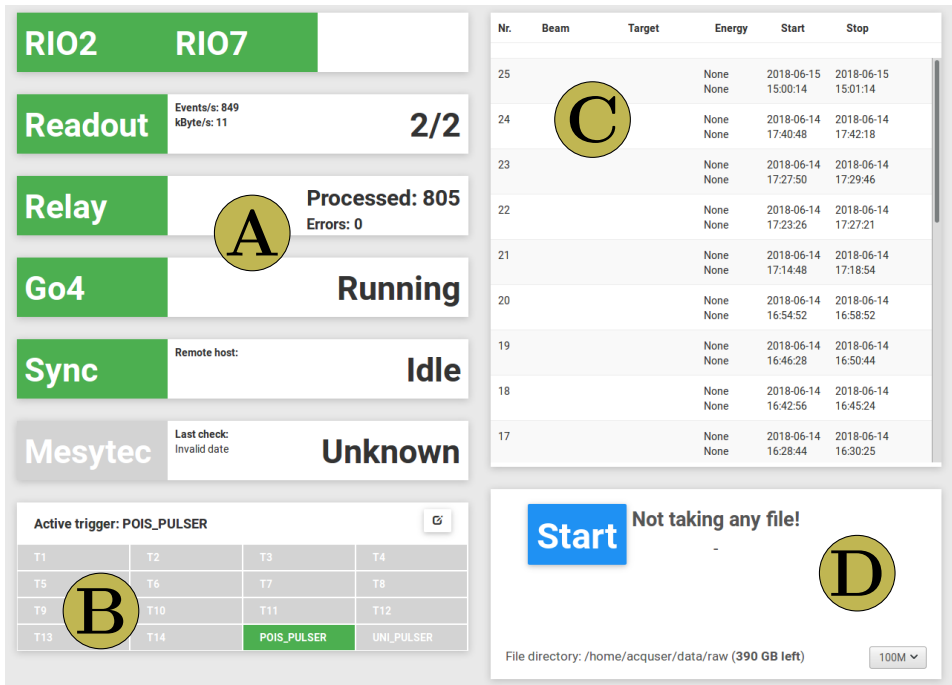


Figure 6.6: The graphical interface of DaqC. Panel (A) shows the status of the different running services. Panel (B) shows the current trigger logic. Panel (C) shows a log of previous runs. Panel (D) gives the user control of the file taking process.

## 6.9 RunDB

The information from the run sheet is essential for the subsequent analysis of the data, both during the experiment and after the experiment. Traditionally this has been written by hand in a paper log by the people on shift when a measurement has been started and stopped. With the implementation of **DaqC**, it was natural to automatically log and compile this data in a database. This led to the development of RunDB, which stores the meta data and file location of the data in a SQL database.

RunDB thus provides an easy way of browsing through the different measurement configuration and in particular the time spent. The automated upload of the run sheet has moreover reduced the number of errors in the log such as wrong time stamps or target configurations.


A web interface makes it easy to search for specific targets, time periods, etc. The interface is shown in Figure 6.7.

## 6.10 Real time monitoring

During an experiment, the running conditions will change. The beam intensity will fluctuate, a detector may pick up some electronic noise or the accelerator may experience a short failure, resulting in no beam at all. While the online analysis is essential to monitor the physics going on in the detector, it does not provide a good overview of such conditions.

The typical way of dealing with this has been to allocate one or two shift people to continuously perform yield estimates on the incoming data, however, this process can largely be automated.

We have implemented this using two open-source projects called **InfluxDB**[79] and **Grafana**[80]. InfluxDB is a time-series database and is thus excellent at storing data with a timestamp. During an experiment, we feed all kinds of data to this database, such as trigger rates, dead time ratio, leakage current from the detectors, pressure in the vacuum chamber, status from the accelerator and even results from simple automated analysis-scripts. This can be done on a second-timescale.



The screenshot shows the RunDB graphical user interface. On the left is a 'Search Filter' panel with fields for Facility (ISOLDE), Experiment (IS561C), Type, Run nr, Beam, Beam Energy, Target, People on shift, and Time interval. A search button is at the bottom of the filter. The main area is a table with the following columns: Nr., Facility, Experiment, Type, Beam, Energy, Target, Start, Duration, #Files, Shifters, Comments, Bad, and More. The table lists various runs with their respective parameters.

Nr.	Facility	Experiment	Type	Beam	Energy	Target	Start	Duration	#Files	Shifters	Comments	Bad	More
402	ISOLDE	IS561C	Pulser				2018-12-05 15:...	00:56:20	76	1			
401	ISOLDE	IS561C	Pulser				2018-12-05 15:...	00:06:34	6	1			
400	ISOLDE	IS561C	Pulser				2018-12-05 15:...	00:05:46	5	1			
399	ISOLDE	IS561C	Pulser				2018-12-05 15:...	00:02:52	4	1			
311	ISOLDE	IS561C	Calibration		4 -alpha source	4-alpha	2018-11-05 16:...	04:47:30	42	1			
310	ISOLDE	IS561C	Run	12C	8 MeV/A	+20 = "good p...	2018-11-05 10:...	02:45:02	22	1			
309	ISOLDE	IS561C	Run	12C	8 MeV/A	+30 = "Fe"	2018-11-05 09:...	00:31:52	5	1			
308	ISOLDE	IS561C	Run	12C	8 MeV/A	+10 = "glue"	2018-11-05 09:...	00:29:04	9	1			
307	ISOLDE	IS561C	Run	9LI	8 MeV/A	The best posit...	2018-11-05 07:...	01:23:38	7	1			
306	ISOLDE	IS561C	Run	9LI	8 MeV/A	The best posit...	2018-11-05 06:...	01:15:30	7	1			
305	ISOLDE	IS561C	Run	9LI	8 MeV/A	The best posit...	2018-11-04 23:...	06:09:46	31	1			
304	ISOLDE	IS561C	Run	9LI	8 MeV/A	3H + 30 steel	2018-11-04 21:...	02:58:16	19	1			
303	ISOLDE	IS561C	Run	9LI	8 MeV/A	3H + 10 glue	2018-11-04 18:...	02:39:04	14	1			
302	ISOLDE	IS561C	Run	9LI	8 MeV/A	DPE	2018-11-04 17:...	00:43:37	4	1			
301	ISOLDE	IS561C	Run		8 MeV/A	DPE	2018-11-04 17:...	00:18:60	2	1			
300	ISOLDE	IS561C	Run	9LI	8 MeV/A	DPE	2018-11-04 14:...	02:56:42	15	1			
299	ISOLDE	IS561C	Run	9LI	8 MeV/A	TI	2018-11-04 12:...	01:55:30	10	1			
298	ISOLDE	IS561C	Run	9LI	8 MeV/A	PE	2018-11-04 09:...	02:48:08	15	1			
297	ISOLDE	IS561C	Run	9LI	8 MeV/A	H3	2018-11-04 09:...	00:06:04	1	1			
296	ISOLDE	IS561C	Run	9LI	8 MeV/A	H3	2018-11-04 24:...	09:02:10	45	1			
295	ISOLDE	IS561C	Run	9LI	8 MeV/A	H3 (Steel)	2018-11-03 21:...	02:13:43	13	1			
294	ISOLDE	IS561C	Run	9LI	8 MeV/A	H3	2018-11-03 18:...	03:20:02	17	1			
293	ISOLDE	IS561C	Run	9LI	8 MeV/A	H3	2018-11-03 18:...	00:20:02	2	1			
292	ISOLDE	IS561C	Run	9LI	8 MeV/A	H3	2018-11-03 17:...	00:20:01	2	1			
291	ISOLDE	IS561C	Run	9LI	8 MeV/A	H3	2018-11-03 17:...	00:20:02	2	1			
290	ISOLDE	IS561C	Run	9LI	8 MeV/A	H3	2018-11-03 16:...	00:19:02	2	1			
289	ISOLDE	IS561C	Run	9LI	8 MeV/A	H3	2018-11-03 16:...	00:20:01	2	1			

Figure 6.7: Graphical user interface from RunDB. The user can search for specific conditions in the left panel. In central table all the different runs are shown.

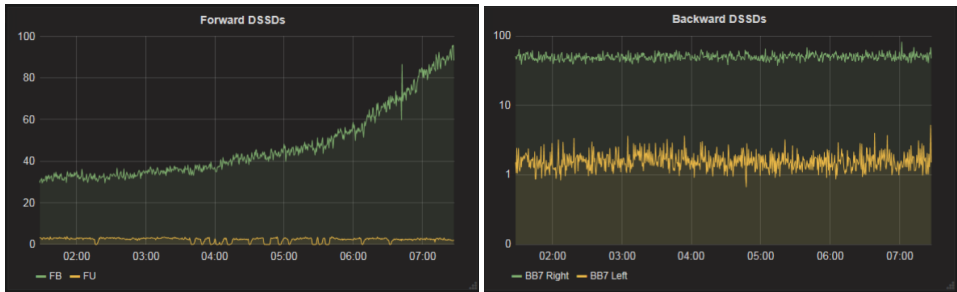


Figure 6.8: Two panels from the Grafana graphical interface. The left shows the trigger rate in two downstream detectors over a period of 5 hours. The right shows the trigger rate in two backward detectors in the same period. The left panel shows an increase in trigger rates, corresponding to a noise problem in the setup.



In particular, the trigger rates can be useful to detect trends in the overall yield. If the beam drops for some reason, the trigger rates will also drop to zero, and this can easily be used for automated alerts for the operator.

Grafana is a simple web frontend that can display the content of the InfluxDB and provide the users with all the data in a structured and interactive way. An example is shown in Figure 6.8. On the left panel is the rate of two detectors at small angles and in the right panel is the trigger rate of two detectors at large angles. Notice how the trigger rate of only one detector rose over the course of several hours. It turned out it was picking up noise and we could ground it properly before it became a problem.

## 6.11 Future upgrades

The trend among many nuclear experiments is to move towards digital DAQ systems. Digital modules are often implemented as a digitizer coupled to a FPGA for waveform processing. Such systems have several advantages. They can analyze the full signal trace and even save it in the data stream. This can potentially allow particle identification based on the waveform and recovery of pile-up events. The digital modules typically operate in a free-running mode, meaning that each channel is self-triggering. This allows for a larger degree of software-based decision making, which generally makes the DAQ more flexible. It is, however, possible to define a global trigger to reduce the data amount[81].

In the group, we have tested two candidates of digital modules. We have a small test setup with two GSI FEBEX[82] cards. Another candidate is the MESYTECH MDPP-16[83], which is a 16-channel VME-based digitizer, and therefore integrates nicely into our existing systems. Currently, we have successfully installed and tested one module. Since it integrates more or less seamlessly into our existing DAQ, the plan is to gradually convert to these modules. Our group is also involved in the installation of PIXIE-16[84] as part of the current upgrade to the ISOLDE Decay Station (IDS).



---

**IS367**

The first experiment was carried out in 2004 and the results were published in a series of papers by Jeppesen and collaborators [31, 35, 45]. Based on the experiences, it was followed up by another experiment in 2005 with an improved setup, mainly manifested as twice the detector coverage.

In this chapter, I will present the analysis of the data from IS367, the extracted cross sections are, however, presented Chapter 13 together with the results from the other experiments. I did not take part in the actual experiment but have analyzed the data based on the logbook and the data from the experiment.

## 7.1 Experimental conditions

The experiment was carried out at ISOLDE, using the REX post accelerator, the predecessor to HIE-ISOLDE with a beam energy of 2.68 MeV/A. The primary target was a deuterated polyethylene ( $\text{CD}_2$ ) target. The background contributions were measured with a pure carbon (C) target and a regular polyethylene target ( $\text{CH}_2$ ).

To estimate the intensity we cannot rely on direct current measurements. This is mainly due to the low intensities of the beam and the short release time of the EBIS. Instead, the intensity is estimated from Rutherford scattering on a heavy silver target using the methods described in 10.3.

An overview of the specifications of the targets and their purpose can be seen in Table 7.1.

Table 7.1: The different target used in IS367.

Target	Thickness	Usage
CD <sub>2</sub>	15 $\mu\text{m}$	The main target.
CD <sub>2</sub>	7.5 $\mu\text{m}$	A thinner main target.
CH <sub>2</sub>	15 $\mu\text{m}$	Background.
<sup>12</sup> C	2 mg/cm <sup>2</sup>	Background.
<sup>9</sup> Be	1.95 mg/cm <sup>2</sup>	Not considered.
<sup>107</sup> Ag	1.1 mg/cm <sup>2</sup>	Yield estimates.

The experimental setup is shown in Figure 7.1. It consists of two BB7s with a thickness of 60  $\mu\text{m}$ . Each DSSD was in a telescope configuration with a 1.5 mm pad detector for particle identification. They were thick enough to stop the light particles and the telescope could thus measure the full energy.

Both detectors are facing the target but only covered the LAB angles below 90°. Due to the kinematic compression discussed in Section 2.2, the energy of the ejectiles in the backward angles are too low to detect properly.

## 7.2 Data analysis

The first task in the data analysis is a calibration of the detectors. From the calibrated energy signals the different particles can be identified. A background subtraction is required before an investigation of the physics in the different reaction channels can be carried out.

### 7.2.1 Energy calibration

The calibration of the detectors was done with a standard  $\alpha$  source, as described in Section 5.3.2. Each segment was calibrated individually and the pads were calibrated with a source from the backside.

Since the energy of the particles that stop in the pad, are up to 4 times larger than the highest calibration point, the calibrations were carefully

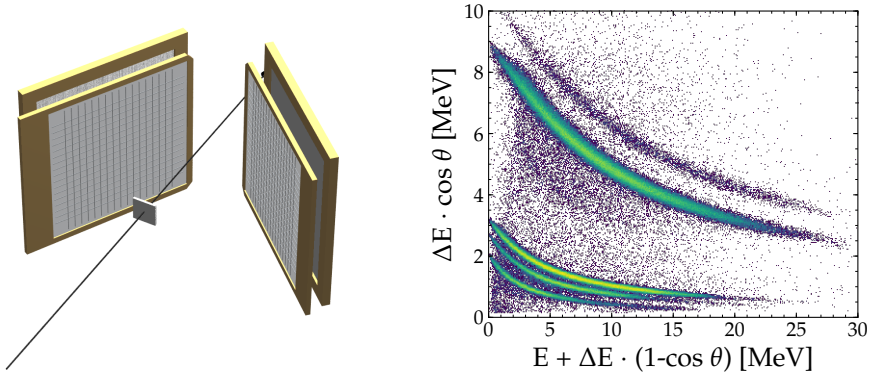


Figure 7.1: **Left** Schematic representation of the setup from IS367. The setup consists of two telescope configurations covering the forward direction in the laboratory. **Right**  $\Delta E$ - $E$  plot for both detectors. The three lower lines corresponds to protons, deuterons and tritons. The two upper lines corresponds to  $\alpha$  and  ${}^6\text{He}$ .

consistency checked at higher energies.

### 7.2.2 Particle identification

The different particles are identified using the methods described in 3.3. The scattered  ${}^9\text{Li}$  from both the heavy Ag target and the main  $\text{CD}_2$  target does not have enough energy to penetrate the  $\Delta E$ -detector. They must, therefore, be identified based on their kinematics, which we will discuss as part of the kinematical analysis.

The right panel in Figure 7.1 shows the  $\Delta E$ - $E$  plot for the measurements with  $\text{CD}_2$ . We can identify protons, deuterons, tritons, and  $\alpha$ . There is also a small contribution of  ${}^6\text{He}$ .

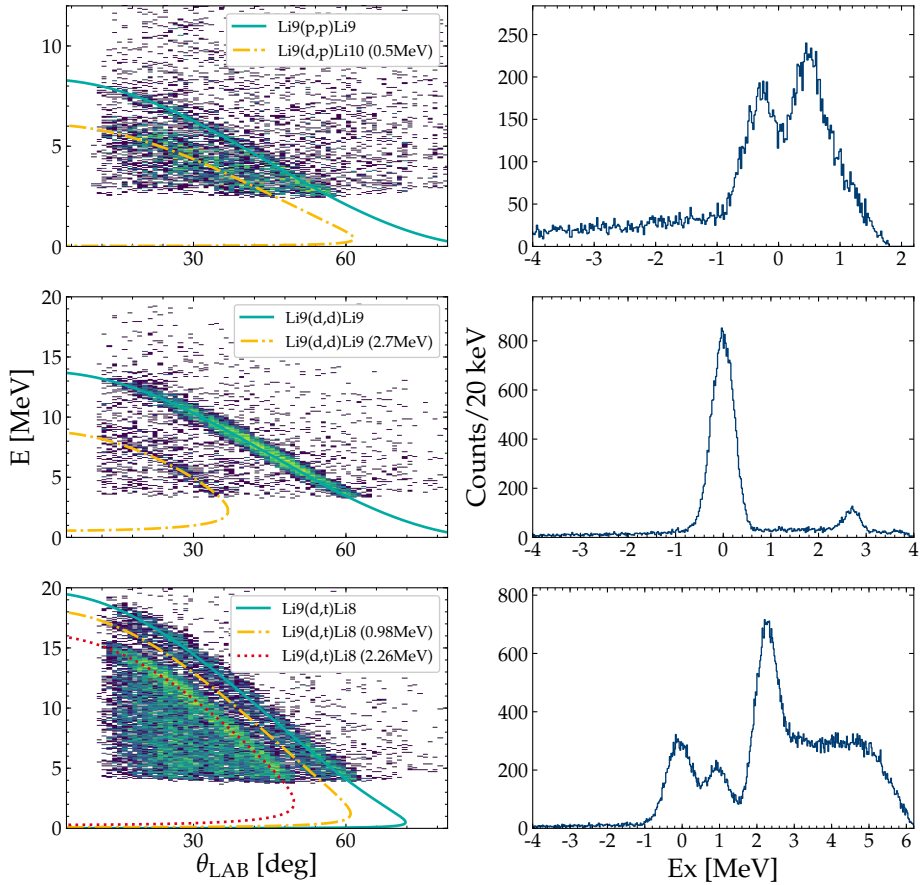


Figure 7.2: Kinematic curves (left column) and excitations spectra (right column) for identified protons, deuterons and tritons from IS367. The excitation spectra is calculated assuming  ${}^9\text{Li}(d,p){}^{10}\text{Li}$ ,  ${}^9\text{Li}(d,d){}^9\text{Li}$  and  ${}^9\text{Li}(d,t){}^8\text{Li}$  respectively. The upper, middle and bottom row shows the results for protons, deuterons and tritons, respectively.

### 7.2.3 Kinematics

The kinematic curves for protons, deuterons and tritons are shown in the left column in Figure 7.2. The corresponding excitation spectra, calculated with Eq. (2.7) are shown in the right column assuming the two-body reactions  ${}^9\text{Li}(d,p){}^{10}\text{Li}$ ,  ${}^9\text{Li}(d,d){}^9\text{Li}$ , and  ${}^9\text{Li}(d,t){}^8\text{Li}$ , respectively.

The protons (top row) have a clear elastic component from  ${}^9\text{Li}(p,p){}^9\text{Li}$ . This is expected since the target has  $\approx 1\%$  protons. To correct for this, a measurement with  $\text{CH}_2$  was performed. The elastic peak from the  ${}^9\text{Li}(p,p){}^9\text{Li}$  can then be subtracted from the measurement with  $\text{CD}_2$ . Notice that it is well separated from the feature expected from  ${}^9\text{Li}(d,p){}^{10}\text{Li}$  reactions, and it is located at negative excitation energies.

The deuterons (middle row) have two well-defined components, corresponding to the ground state and first excited state at 2.7 MeV [26]. The width of the  ${}^9\text{Li}$  ground state peak can be used to estimate the resolution of our setup. A Gaussian fit gives a resolution of  $\text{FWHM} = 551(4)$  keV.

The tritons (bottom row) have clear components from the ground state ( $2^+$ ) and the first two excited states at 0.98 MeV ( $1^+$ ) and 2.26 MeV ( $3^+$ ). There is a known broad resonance at 3.21 MeV ( $1^+$ ) [26], however, it is above the neutron separation threshold. It is therefore embedded in the continuum.

Evidence for a  $0^+$  state at 1.9 MeV has been observed in the mirror nuclei  ${}^8\text{B}$  [85], and is therefore also expected in  ${}^8\text{Li}$ . The spectrum does, however, not reveal any unknown states below the continuum. A proper search for a  $0^+$  state requires a more careful analysis, which I have not pursued.

All the channels have two or more particles in the final state, and coincidences were also detected. An example of  ${}^9\text{Li}(d,d){}^9\text{Li}$  is shown in Figure 7.3 (A). The kinematic lines fit nicely. Notice also, how clean the spectrum is with the coincidence requirement.

**Heavy target** The scattered  ${}^9\text{Li}$  does not penetrate the DSSD and thus cannot be identified with the  $\Delta E - E$  technique. Instead, they are gated based on kinematics. Figure 7.3 (B) shows the kinematic curve for  ${}^9\text{Li}$  scattering off of silver. The data follows the kinematics nicely and the  ${}^9\text{Li}$

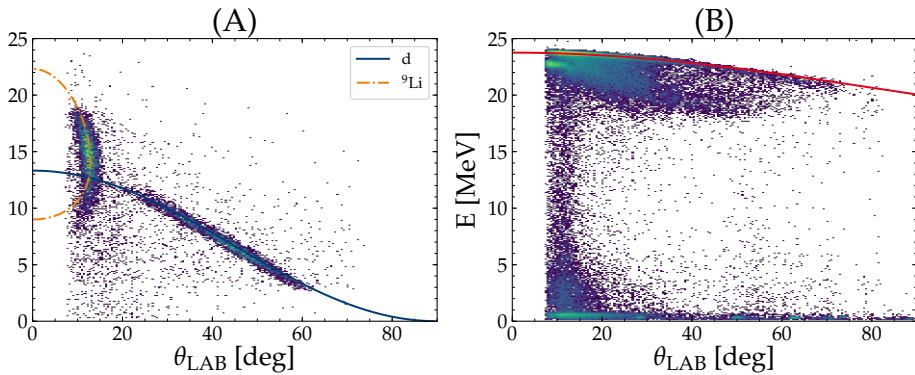


Figure 7.3: (A) Coincident deuterons and  ${}^9\text{Li}$  with the kinematic curves corresponding to the ground state of  ${}^9\text{Li}$ . (B) Kinematic curve of  ${}^9\text{Li}$  scattering off of silver.

can be isolated. Notice the feature below the main curve. This is an artifact of a faulty strip in one of the detectors.

#### 7.2.4 Background subtraction

The  ${}^{10}\text{Li}$  spectrum has a peak just below 0 MeV followed by a large tail at negative excitation energies. These events are unphysical in the sense, that they cannot originate from a  ${}^9\text{Li}(d,p){}^{10}\text{Li}$  reaction, there is simply not enough energy. The events must instead come from various background contributions from reactions with protons and carbon in the target. The peak below 0 MeV for instance, corresponds to  ${}^9\text{Li}(p,p){}^9\text{Li}$ . Background contributions from both carbon and protons were measured with a C target and a  $\text{CH}_2$  target respectively. The results are piped through the same analysis and provide an estimate of the background. The different components are shown Figure 7.4 (A). The background in the  $\text{CD}_2$  data can be evaluated by fitting a superposition of the two background components to the negative excitation energies. This can subsequently be subtracted from the spectrum. The fit



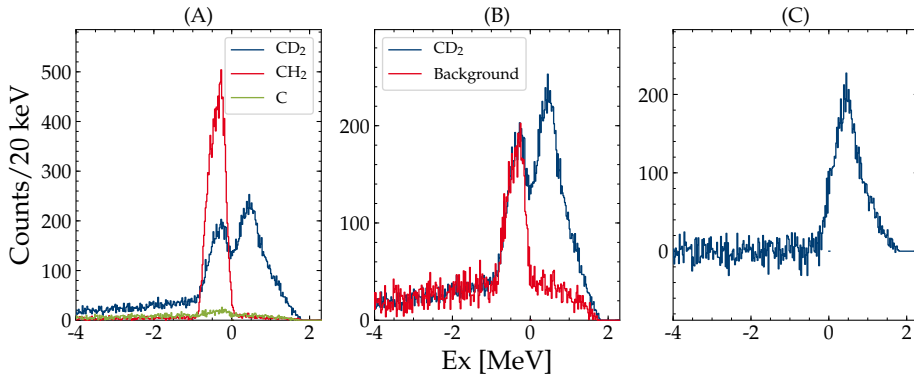


Figure 7.4: **(A)** Excitation spectra for protons from CD<sub>2</sub> target and the two background targets, CH<sub>2</sub> and C. **(B)** The combined background on top of the signal. **(C)** The resulting background subtracted spectrum.

provides two coefficients

$$\text{BG} = 0.25(4) \cdot \text{CH}_2 + 0.35(1) \cdot \text{C}. \quad (7.1)$$

The coefficients are the same for deuterons and tritons since the experimental conditions were the same.

### 7.3 Intensity

The final important ingredient to normalize the data to absolute cross sections is the total number of incoming beam particles which in turn relates to the intensity. This was measured with a heavy target.

In the following discussion we will refer to measurements with such a heavy target as an *intensity measurement* and we will refer to a measurement with the deuterated target as a *physics measurement*.

During the experiment, several intensity measurements were made, sandwiched between two physics measurements. From the intensity measurement,

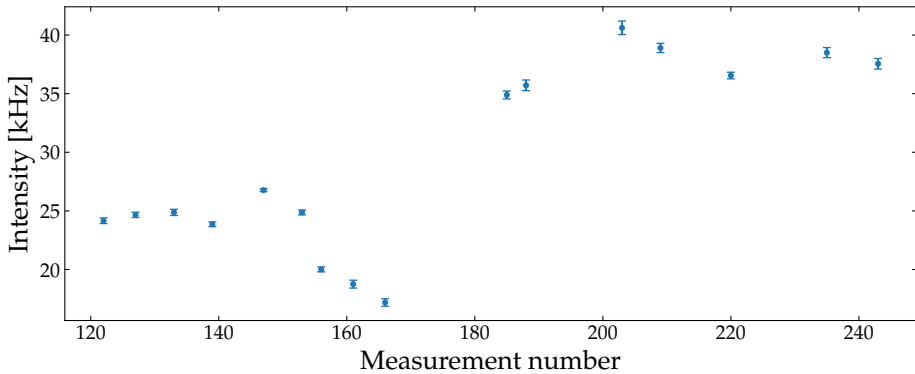


Figure 7.5: Intensity measurements throughout the experiment. The increase in intensity after measurement 180 is due to a reoptimization of the beam by the operators.

we obtain the intensity, which is related to the number of scattered particles in the adjacent physics measurements. If we know how the number of scattered deuterons relates to the intensity, we can extrapolate to the remaining physics measurements, which were not part of a sandwich.

Let us denote the beam intensity in the intensity measurement by  $I$ , which is calculated with the methods in Section 10.3. The intensity across all intensity measurements in the experiment can be seen in Figure 7.5.

Notice that the intensity fluctuates. If it is only the intensity that changes, the number of scattered particles in any given reaction channel should scale accordingly. For instance, the number of scattered deuterons will scale with the number of incoming beam particles. This means that if we can calculate the number of deuterons per incoming beam particle

$$\mathcal{N}_d = \frac{N_d}{N_{9\text{Li}}}, \quad (7.2)$$

we can in principle count deuterons in a given measurement and calculate the corresponding time-integrated intensity

The ratio  $\mathcal{N}_d$  between incoming can be calculated with the sandwiched measurements under the assumption that the intensity is constant across the three measurements. The intensity measurement provides  $I$ , and the adjacent physics measurements provide the rate of scattered deuterons,  $R_d$ . The ratio is thus

$$\mathcal{N}_d = \frac{N_d}{N_{9\text{Li}}} = \frac{R_d \cdot t_P}{I \cdot t_I}, \quad (7.3)$$

where  $t_P$  is the length of the physics run and  $t_I$  is the length of the intensity run. The assumption that the intensity does not change during two adjacent measurements, which is generally not correct. In particular, the super cycle at CERN will determine how many proton bunches that reaches ISOLDE. This changes on a timescale that is comparable to the length of the runs. However, by looking at the distribution across all intensity measurements, it is possible to treat this systematic error as a statistical error.

Figure 7.6 shows  $\mathcal{N}$  as a function of measurement number. The upper panel is the deuterons and the lower panel is for  $\alpha$ . The median, as well as the  $1\sigma$  interquartile range, is shown. We use the median since it is more robust to outliers. In practice, however, the median turned out to be very close to the weighted average.

The distribution does not seem to have a clear systematic trend. We can make a  $\chi^2$  test, to check if the individual  $\mathcal{N}$  estimates are consistent with being from the same normal distribution. For deuterons we get a  $pval = 0.048$ . This is on the edge of being consistent with coming from the same mean, but due to the expected systematic errors, we accept it, with a correspondingly larger uncertainty on the integrated intensity.

The medians for the two particle types are respectively

$$\begin{aligned} \mathcal{N}_d &= 8.50 \cdot 10^{-6} \pm 6.67\% \\ \mathcal{N}_\alpha &= 3.08 \cdot 10^{-5} \pm 7.90\% \end{aligned}$$

The time-integrated beam intensity across all the physics measurements can now be calculated, by simply counting scattered particles and scale

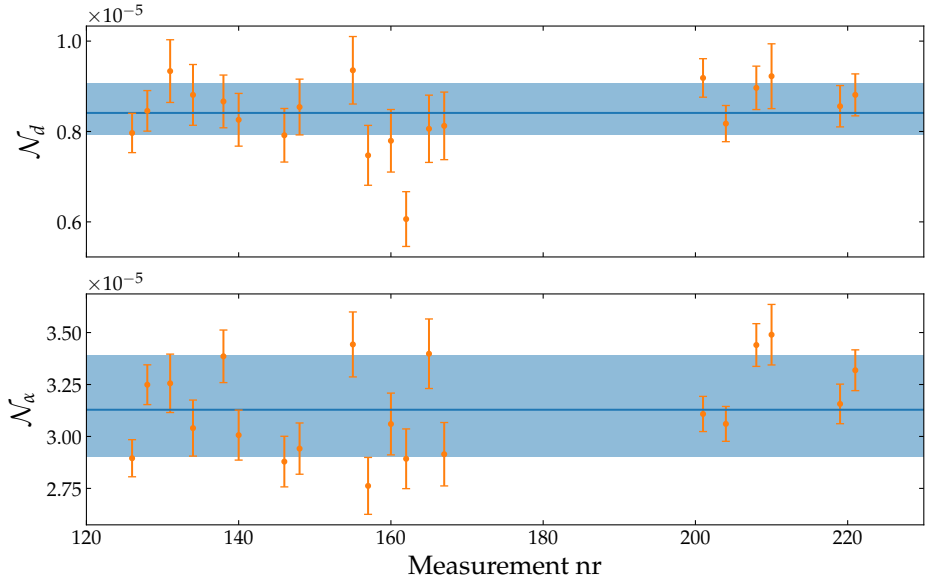


Figure 7.6: Particle per incident  ${}^9\text{Li}$  for d and  $\alpha$  respectively. The blue band corresponds to the median with  $1\sigma$  interquartile range.

them with  $\mathcal{N}$

$$N_{9\text{Li}} = \frac{1}{\mathcal{N}_k} \sum_i N_i^k, \quad (7.4)$$

where  $k$  can be either protons, deuterons, tritons or  $\alpha$ . For deuterons and  $\alpha$  we get

$$\begin{aligned} N_{9\text{Li}}^d &= 3.97 \cdot 10^9 \pm 6.7\% \\ N_{9\text{Li}}^\alpha &= 4.07 \cdot 10^9 \pm 7.9\%, \end{aligned}$$

which is consistent within the statistical uncertainties. We can do the

same for both tritons and protons, and they are all consistent within the uncertainties, so we do a weighted average of all four

$$N_{9\text{Li}}^{\text{avg}} = 4.04 \cdot 10^9 \pm 1.2\%,$$

which will be used to normalize cross sections.

### 7.3.1 Angular distributions

Angular distributions for the individual channels can now be extracted by gating the excitation spectra, projecting on the angular axis and acceptance correct as described in Chapter 10. Since the calculations are often done in the CM frame, a transformation is first applied and the projection is done onto the  $\theta_{\text{CM}}$  axis. The result of this will be presented in Chapter 13 as it is more meaningful to discuss alongside the results from IS561A and IS561C as well as theoretical calculations.



---

## IS561A

The second experiment was carried out in 2016, and it was the first I participated in. The goal was to study the  ${}^9\text{Li}(d,p){}^{10}\text{Li}$  at a higher beam energy compared to IS367. It was the first experiment at ISOLDE with the HIE-ISOLDE upgrade. The upgrade was only partially complete at the time, but we were still able to get a significantly higher beam energy, namely 6.72 MeV/A. This was requested to be able to measure the protons from the  ${}^9\text{Li}(d,p){}^{10}\text{Li}$  reaction in the backward directions, where the energy would only be 0.5 MeV-1.0 MeV due to the kinematic compression, as discussed in Section 2.2. The setup was redesigned and in particular, included a telescope to cover backward angles.

During the experiment, we encountered problems both with beam alignment and low yields from the ISOLDE part. This resulted in significantly lower statistics than expected. The beam alignment problems also led us to steer the beam around during the experiment, which in turn has required a more careful analysis.

The experimental program for this experiment was very similar to the older IS367. We used a deuterated polyethylene target ( $\text{CD}_2$ ) as the main target. For background measurements, we used a pure carbon target and a normal polyethylene target ( $\text{CH}_2$ ). For intensity measurements, we used a gold target. A table of the targets is shown in Table 8.1.

The operators used  ${}^{12}\text{C}$  as a pilot beam to steer the beam into the chamber. We made some measurements with this beam, which turned out to be very useful. The pilot beam is more intense, and a measurement could quickly acquire a significant amount of statistics. Reactions with this beam

provided good constraints on the geometry and beam properties, which will be discussed later.

Table 8.1: The different target used in IS561A.

Target	Thickness	Usage
CD <sub>2</sub>	8 $\mu\text{m}$	The main target.
CH <sub>2</sub>	6 $\mu\text{m}$	Background.
<sup>12</sup> C	2 mg/cm <sup>2</sup>	Background.
<sup>197</sup> Au	0.1 $\mu\text{m}$	Yield estimates. Backed by 3.5 $\mu\text{m}$ mylar

## 8.1 Setup

The experimental setup was updated compared to IS367. A picture is shown in Figure 8.1. The setup has detector coverage in both forward and backward directions. In the forward direction (1) there are five telescopes placed symmetrically around the beam axis in a pentagon structure. Each of these is 60  $\mu\text{m}$  W1s backed by a 1.5 mm pad. Perpendicular on the beam axis was a round DSSD with a thickness of 1 mm, an S3. The idea with this design is inspired by the method discussed in Chapter 4. The thick DSSD captures the recoils and the 5 pentagon detectors capture the light ejectiles. The high degree of symmetry provides good constraints on the beam spot and beam direction. The detectors were mounted in a 3D-printed plastic structure, which ensured good geometrical constraints on the detector positions.

A single telescope (3) with a 60  $\mu\text{m}$  BB7 backed by a 1 mm pad is placed in the backward direction. The purpose of this detector is measuring the ejectiles in the backward LAB direction, which corresponds to the forward CM angles due to the inverse kinematics. The kinematic compression poses two main challenges. First, even though the backward region has larger cross sections for the protons, the CM solid angle is suppressed as discussed in Section 2.2. The energy of the protons from <sup>9</sup>Li(d,p)<sup>10</sup>Li are



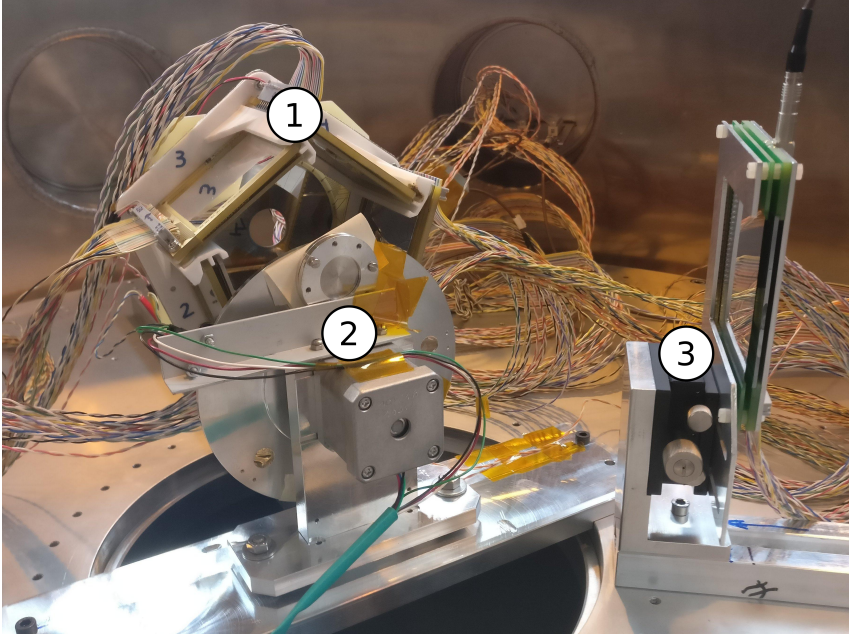


Figure 8.1: The experimental setup used in IS561A. A pentagon structure of W1 detectors with an S3 at the end covers the forward directions(1). A motorized wheel held the targets (2). In the backward direction were a single BB7 placed (3).

500 keV-1000 keV, and will thus not penetrate the DSSD in the backward telescope. This makes particle identification challenging and requires low trigger thresholds.

The targets are placed on a motorized wheel (2) which could be controlled from outside of the vacuum chamber. This enabled easy target change without having to open up the vacuum chamber.

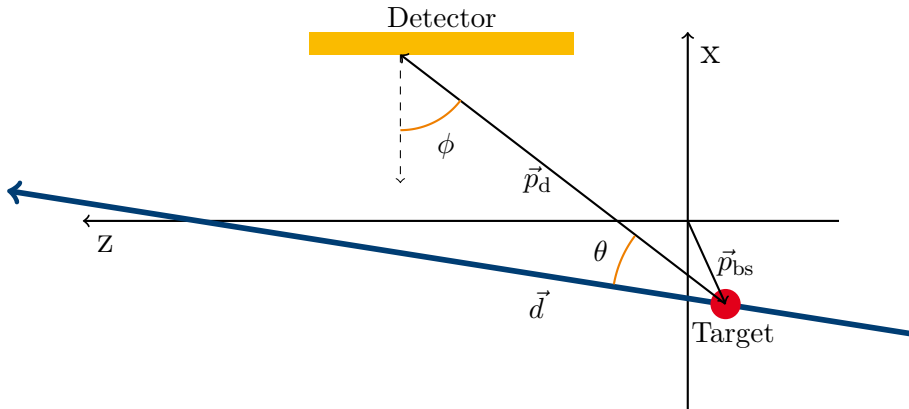


Figure 8.2: Sketch of the scattering of a particle relative to the beam axis and detector. The reaction happens at the beam spot  $\vec{p}_{bs}$ . The kinematic angle  $\theta$  must be in respect with the direction of the beam,  $\vec{d}$ . The relative angle between the particle and the normal detector,  $\phi$  does not depend on the beam axis, but on the beam spot.

## 8.2 Calibration and beam properties

The calibration of the five DSSDs in the pentagon and the backward DSSD is done with an  $\alpha$  source as described in Section 5.3.2. An initial calibration for the pads is done in the same way. It became clear, however, that these were not precise enough at higher energies. One pad, in particular, had undergone a change between the calibration and the measurements, and the calibration could thus not be trusted. Besides the calibrations, it became clear that the beam axis was angled significantly with respect to the setup. There were too few coincidences to use the method described in Chapter 4.

Instead, the kinematic curves of well know reactions can be used to determine the beam spot and the beam direction. The beam is described by five parameters as illustrated in Figure 8.2

$$\begin{aligned}\vec{p}_{\text{bs}} &= (x, y, z) \\ \hat{d} &= (\theta, \phi),\end{aligned}$$

where  $\vec{p}$  is the position where the beam hits the target in a global coordinate system and  $\hat{d}$  is the unit vector in the direction of motion of the beam. The kinematics of any reaction is given by the angle relative to the incoming momentum and therefore the beam axis,

$$\cos \theta = \frac{(\vec{p}_d - \vec{p}_{\text{bs}}) \cdot \hat{d}}{\|\vec{p}_d - \vec{p}_{\text{bs}}\|}, \quad (8.1)$$

where  $\vec{p}$  is the vector to the detection position.

An initial guess of  $\vec{p}_{\text{bs}} = (0, 0, 0)$  and  $\hat{d} = \hat{z}$  is good enough to identify the elastic scattered deuterons from the  $^{12}\text{C}(d,d)^{12}\text{C}$ . We use the  $^{12}\text{C}$  beam since the intensity was several orders of magnitude larger than  $^9\text{Li}$ . Figure 8.3 (A) shows the initial guess and a kinematic curve. The fit of the curve is not particularly good, but the elastic component is easily identified. The kinematic curve is now fitted to the ensemble by minimizing a  $\chi^2$  with the beam parameters as the free parameters

$$\chi^2 = \sum_i \frac{(E_i - T_d(\theta_i))^2}{\sigma^2}, \quad (8.2)$$

where  $E_i$  is the total measured energy in the telescope (corrected for dead layers),  $\theta_i$  is the angle calculated with Eq. (8.1),  $T_d(\theta_i)$  is the kinematic curve from Eq. (2.8) and  $\sigma$  is the resolution. Notice that this method does not account for divergence, spatial distribution or energy distribution. It turned out, however, that the detector resolution sets the limit unless the beam is unphysically large. The uncertainties on the parameters are also mainly due to the detector resolution.

A crucial part of this method is the symmetrical coverage from the pentagon. With just one telescope, the orthogonal direction to that detector is too unconstrained, but having five telescopes covering most of the polar angle,  $\phi$ , constraints the parameters sufficiently.

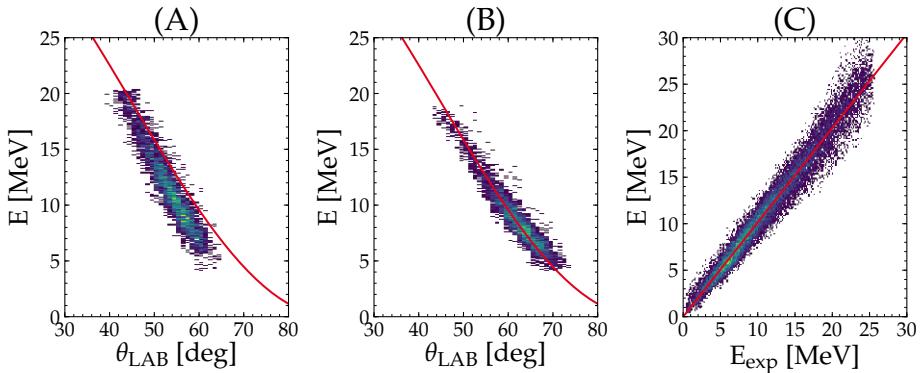


Figure 8.3: Kinematic curves for the  $^{12}\text{C}(\text{d},\text{d})^{12}\text{C}$  reaction are shown before and after a fit of the beam parameters, in (A) and (B) respectively. (C) The linear relationship between expected and measured energy in the pad.

The result is shown in Figure 8.3 (B), with one important extension. The pad calibrations were also adjusted since they did not extrapolate nicely to large energies. This imposes an extra challenge since  $E_i$  depends on the pad energy.

Consider again the elastic scattering of deuterons from  $^{12}\text{C}$ . The scattered deuterons penetrate the DSSD, and the energy deposited depends on the distance traveled in the DSSD, which in turn depends on the geometry of the detector and the angle of the deuteron,  $\phi$ .

The initial energy of a deuteron can be determined from the energy deposited in the DSSD with the help of energy loss tabulations. The effective distance it travels in the detector,  $t_{\text{eff}}(\phi)$ , depends on  $\phi$  as described in Eq. (3.1) from Section 3.3. We can find the initial energy (before the particle hits the telescope)  $E_{\text{init}}$  numerically, that corresponds to a certain measured energy in the DSSD

$$\Delta E(\phi) = \int_0^{t_{\text{eff}}(\phi)} \left. \frac{dE}{dx}(x) \right|_{E_{\text{init}}} dx, \quad (8.3)$$

where  $\frac{dE}{dx}(x)$  is the tabulated energy loss.

The expected energy in the pad is the remaining energy

$$E_{\text{exp}} = E_{\text{init}}(\phi) - \Delta E(\phi) - \Delta E_{\text{deadlayer}}, \quad (8.4)$$

where  $\Delta E_{\text{deadlayer}}$  is the sum of the various energy losses in dead layers.

The relationship between the ADC channel and  $E$  is linear which in turn means that the relationship between the actual energy  $E$  and  $E_{\text{exp}}$  is linear. A fit thus provides an improved calibration. Note that this works for all the different particle types. Figure 8.3 (C) shows the linear relationship and a corresponding fit.

There is one issue with these two procedures, that unfortunately make them dependent on each other. The pad calibration requires  $\phi$  which depends on  $\vec{p}_{\text{bs}}$ . The determination of  $\vec{p}_{\text{bs}}$  requires the kinematic fit, which relies on the pad calibrations. We are caught in a vicious cycle. By iterating the two methods, however, it was possible to converge, even though it required some hand-tuning.

The result is

$$\vec{p}_{\text{bs}} = \begin{cases} x = & 6.0(4) \text{ mm} \\ y = & -3.1(4) \text{ mm} \\ z = & 4.3(2) \text{ mm} \end{cases} \quad \hat{d} = \begin{cases} \theta = & 3.2(6)^\circ \\ \phi = & -135(1)^\circ \end{cases}$$

### 8.2.1 Intensity

We only performed a single measurement on a heavy gold target to estimate the intensity due to the issues with the beam. The scattered  ${}^9\text{Li}$  particles are very forward-focused, so they only hit the downstream DSSD. The spectrum is shown in Figure 8.4 (A). Notice that the beam energy has been reduced to account for energy loss in the target of the kinematic curve. The intensity is estimated with the same analysis as in Section 10.3, but only for a single measurement. The intensity during the measurement was

$$I = 4.6 \text{ kHz} \pm 6.4 \%,$$

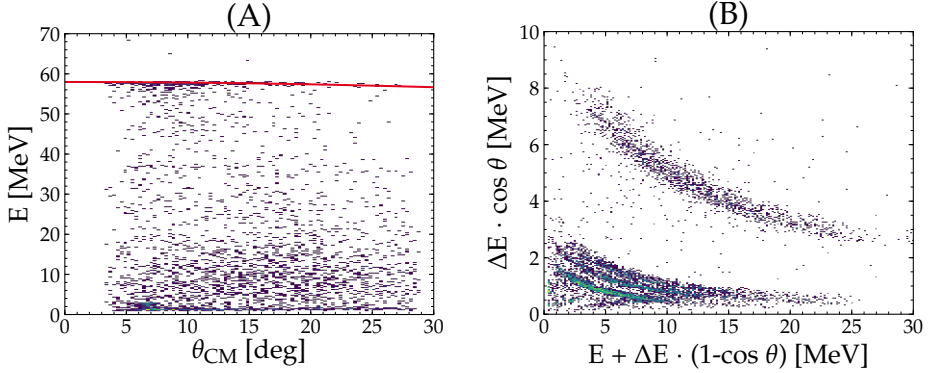


Figure 8.4: **(A)** Kinematic spectrum for elastic scattered  ${}^9\text{Li}$  off of a gold target. The kinematic curve has been corrected for energy loss in the target. **(B)**  $\Delta E - E$  spectrum from the pentagon detectors. The spectrum shows protons, deuterons and tritons as well as *alpha*.

with a ratio

$$\mathcal{N}_d = 1.53 \cdot 10^{-6} \pm 11.2\%,$$

and a total number of  ${}^9\text{Li}$

$$N_{9\text{Li}}^d = 2.87 \cdot 10^8 \pm 8.7\%.$$

### 8.3 Data analysis

We can evaluate the data with calibrations, beam spot and beam direction determined. The  $\Delta E - E$  spectrum is shown in Figure 8.4 (B), for the pentagon detectors. As in IS367 there are protons, deuterons, tritons, and  $\alpha$ . The corresponding kinematic curves and excitation spectra are shown in Figure 8.5.

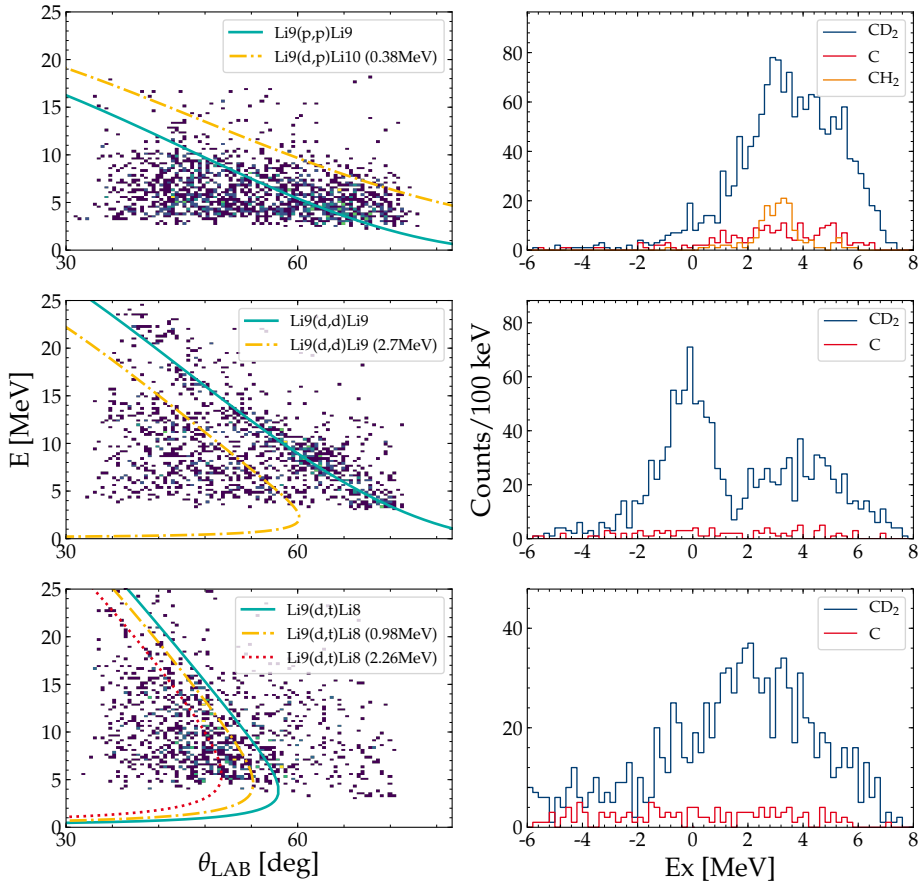


Figure 8.5: Kinematic curves (left column) and excitation spectra (right column) for identified protons, deuterons, and tritons from IS561A. The excitation spectra are calculated assuming  ${}^9\text{Li}(\text{d,p}){}^{10}\text{Li}$ ,  ${}^9\text{Li}(\text{d,d}){}^9\text{Li}$  and  ${}^9\text{Li}(\text{d,t}){}^8\text{Li}$  respectively and the background components are superimposed on the excitation spectra. The upper, middle and bottom row show the results for protons, deuterons, and tritons, respectively.

### 8.3.1 Forward telescopes

The background contributions are shown in all three plots in Figure 8.5. The background of deuterons and the tritons due to the protons in CH<sub>2</sub> is negligible, and the C background is sufficient. For the protons, however, there is a significant contribution. Moreover, due to the larger beam energy, the background from elastic protons is now in the middle of the excitations spectrum for <sup>10</sup>Li.

The proton spectrum has a rather large feature without a lot of structure. The elastic proton peak is, however, visible around 3 MeV as a peak on top of a broader structure beneath.

The deuteron spectrum shows the ground state around 0 MeV and a broader structure at higher energies. The first excited state at 2.7 MeV is easily embedded in this region. The neutron separation energy for <sup>9</sup>Li is 4.06 MeV[26], so we start to get into the continuum, and thus expect little structure, even if there are <sup>9</sup>Li resonances up to 6.43 MeV. The resolution is clearly worse than in IS367, but this is expected from the higher beam energy.

The triton spectrum has less structure than at 2.68 MeV/A. It is curious that the ground state is so weak, but this is left for further analysis.

### 8.3.2 Backward telescope

The backward telescopes should capture the protons from the <sup>9</sup>Li(d,p)<sup>10</sup>Li reaction. Figure 8.6 (A) shows the  $\Delta E - E$  plot for the telescope to the left. There are some high energy particles that penetrate the DSSD, likely originating from fusion reactions. The interesting protons, however, have too little energy to penetrate and stop in the DSSD. The penetrating particles can be suppressed by vetoing on the pad. The resulting kinematic plot is shown in Figure 8.6 (B). The kinematic curve for <sup>9</sup>Li(d,p)<sup>10</sup>Li is drawn on top, to show where the protons are expected.

There is not much structure in the kinematic plot. The features down in the right corner are, unfortunately, a noise peak. This effectively renders half of the detector incapable of detecting the protons from <sup>10</sup>Li. The other half



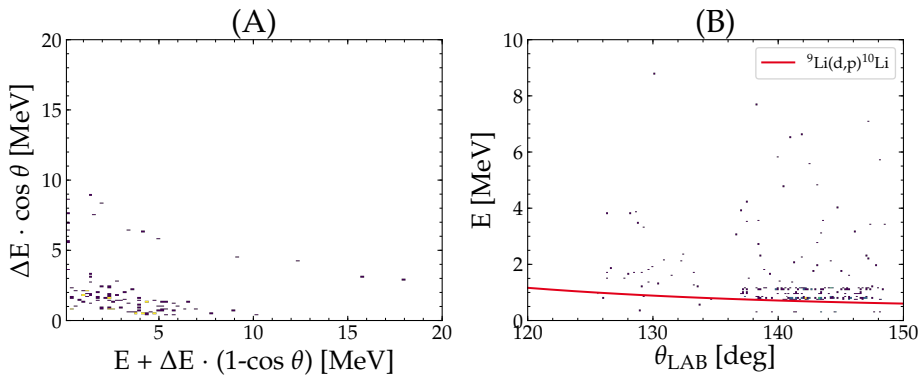


Figure 8.6: Results from the backward telescope. **(A)** The  $\Delta E - E$  spectrum. **(B)** The kinematic spectrum for events that stop in the DSSD.

has very few events and in particular not enough to extract any structure in terms of angular distributions. This could be a DAQ related problem. Since there is noise in half a detector, which corresponds to one shaper, the trigger-thresholds may have been too high in an attempt to suppress the noise. This may, however, have been such that interesting physics events are ignored.



## IS561C

The last experiment was carried out in the fall of 2018. The main goal of this experiment was the two neutron transfer with a tritium target to study  $^{11}\text{Li}$ . The tritium was embedded in a titanium foil and we, therefore, used a pure titanium target to estimate the background. For this experiment the energy upgrade of HIE-ISOLDE was complete, so it could deliver 8.0 MeV/A. This energy would give an extra boost to the low energy ejectiles in the backward directions as compared to IS561A.

As a secondary target, we used a deuterated plastic ( $\text{CD}_2$ ) target in the chamber. A normal plastic target ( $\text{CH}_2$ ) was also present for background measurements. This, unfortunately, turned out to be necessary. The main target was damaged from an earlier experiment, and the repair made it more or less unusable for our purpose. I will discuss this in more detail in Section 9.3. For the stable pilot beam, a heavy lead target was in the chamber but ended up not being used. It was, however, not in the chamber during the radioactive beam. A table of all the targets can be seen in Table 9.1.

The beam properties are determined from elastic deuterons from reactions with the stable pilot beam, as described for IS561A. The beam spot ( $\vec{p}_{bs}$ ) and beam direction ( $\vec{d}$ ) are estimated to be

$$\vec{p}_{bs} = \begin{cases} x = & -0.1(3) \text{ mm} \\ y = & 0.4(3) \text{ mm} \\ z = & -3.7(2) \text{ mm} \end{cases} \quad \hat{d} = \begin{cases} \theta = & 0.4(5)^\circ \\ \phi = & -23(1)^\circ \end{cases}$$

Table 9.1: The different targets used in IS561C.

Target	Thickness	Usage
${}^3\text{H}({}^{48}\text{Ti})$	$450 \mu\text{g}/\text{cm}^2$	Primary target
${}^{48}\text{Ti}$	$900 \mu\text{g}/\text{cm}^2$	Background for primary target
$\text{CD}_2$	$15 \mu\text{m}$	Secondary target.
$\text{CH}_2$	$15 \mu\text{m}$	Background for secondary target.
${}^{208}\text{Pb}$	$1 \text{mg}/\text{cm}^2$	Heavy target. Only used with the stable ${}^{12}\text{C}$ beam.

## 9.1 Setup

The setup for this experiment was very similar to the one used in IS561A. The only major difference was an addition of another backward telescope, placed symmetrically to the previous one and thereby effectively doubling the coverage in the backward directions. We will refer to the two backward telescopes as BB7L for the left and BB7R for the right one. An illustration of the setup is shown on the left in Figure 9.1.

A small silicon telescope was installed at the beam dump. The motivation was to identify different beam contaminants such as  ${}^{12}\text{C}$  or  ${}^{18}\text{O}$ . The large instantaneous intensities meant that it could not be used for intensity measurements due to severe pileup effects during the experiment. Moreover, the detectors in the telescope deteriorated significantly during the experiment. It was thus useful as a qualitative diagnostics tool during the experiment, but not for quantitative analysis.

A Faraday Cup could alternatively be moved into the beam dump, which also served as a diagnostics tool during the experiment. It was, however, not sensitive enough to give a reliable estimate of the beam intensities.

## 9.2 Deuteron target

The secondary target was deuterated plastic ( $\text{CD}_2$ ). Due to the limited space on the target holder, we only mounted a  $\text{CH}_2$  target for background

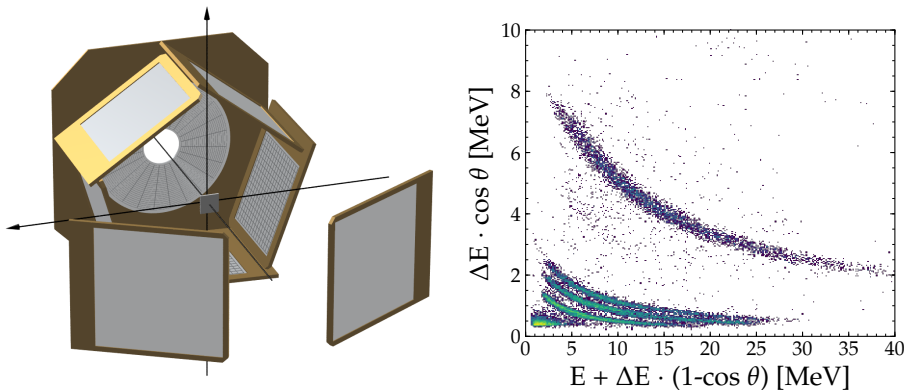


Figure 9.1: **Left:** Rendering of the setup used in IS561C. It is very similar to the one used in IS561B, but with an additional telescope in the backwards direction. **Right:**  $\Delta E - E$  plot from the pentagon detectors.

measurements and no pure carbon target. The  $\Delta E - E$  plot for the forward detectors is shown on the right in Figure 9.1, and shows protons, deuterons, tritons, and  $\alpha$ . The resulting excitation spectra are shown in Figure 9.2.

The proton spectrum (Figure 9.2 (A)) shows largely the same features as at 6.72 MeV/A, where the background again is dominated by the elastic peak. Since there was no measurement with pure carbon we cannot explicitly subtract the carbon component. It was instead estimated by looking at the continuous contributions from the  $\text{CH}_2$  in regions far from the proton peaks.

The deuteron spectrum (Figure 9.2 (B)) have a large ground state peak and the first excited state at 2.7 MeV. The neutron separation threshold at 4.06 MeV is clearly visible. Above this threshold, there are several known resonances at 4.2 MeV, 5.4 MeV and 6.4 MeV[26]. The 6.4 MeV resonance has a reported width of 40(20) keV. The  $S_{2n} = 6.09$  MeV causes a continuum spectrum in this region, however, the peak close to 6.4 MeV is too narrow to be only a continuum, and we thus interpret it as evidence for the resonance. There could be an indication for the resonance at 4.2 MeV, however, it coincides with the neutron threshold  $S_n = 4.06$  MeV. The resonance at

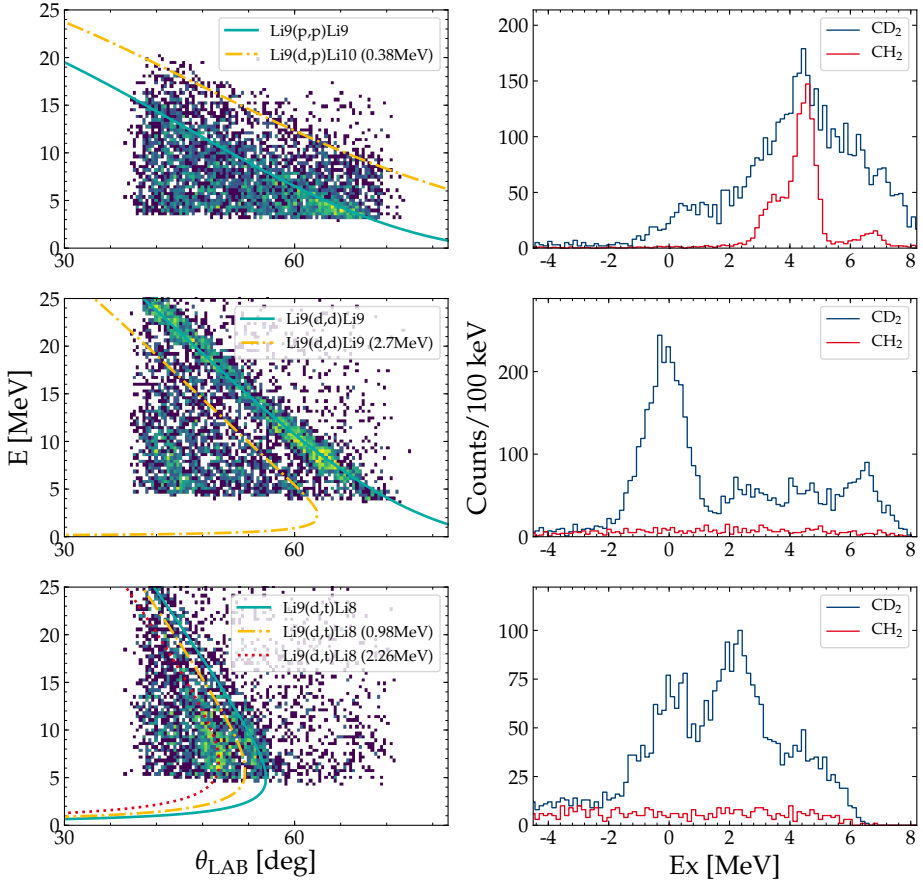


Figure 9.2: Kinematic curves (left column) and excitation spectra (right column) for identified protons, deuterons and tritons from IS561C. The excitation spectra is calculated assuming  ${}^9\text{Li}(d,p){}^{10}\text{Li}$ ,  ${}^9\text{Li}(d,d){}^9\text{Li}$  and  ${}^9\text{Li}(d,t){}^8\text{Li}$  respectively and the background component from  $\text{CH}_2$  is superimposed on the excitation spectra. The upper, middle and bottom row show the results for protons, deuterons, and tritons, respectively.

5.4 MeV is not seen. The excitation spectrum of  ${}^9\text{Li}$  requires a more careful analysis, which is left for the future analysis.

In the triton spectrum, there is a prominent ground-state and second excited state at 2.26 MeV. The first excited state at 0.98 MeV is not resolved with the resolution of this setup.

The backward detectors did, unfortunately, not provide proper measurements in the interesting region of (d,p) reactions, due to trigger thresholds issues, which I will return in Section 9.3.3.

## 9.3 Tritium target

During the, run we noticed a significant contribution from an unknown component in the tritium target. Due to a remount of the target in a previous experiment, we suspected that it was due to glue that was used to attach the target. To sort this out and potentially get a background subtraction we steered the beam too, what we believed was the outer regions of the target. The target was thus divided into three regions. One that was mainly the steel used for the mount (Steel), one that was the central (good) region of the target (H3) and lastly a part dominated by glue (Glue). A picture of the target is shown in Figure 9.3.

### 9.3.1 Pentagon detectors

If the target only contained the expected  ${}^3\text{H}$  and  ${}^{48}\text{Ti}$  components, all the protons would come from a variety of reactions with  ${}^9\text{Li}$ . If there is a contaminant with a lot of protons (such as glue), a major component of elastically scattered protons will show up in a kinematic plot. Let us limit the analysis to the forward pentagon detectors for now. Kinematic curves for the three regions are shown in Figure 9.4 together with the expected kinematic curve for elastically scattered protons. We observe a big contaminant in both the H3 region and the Glue region. Notice the energy offset to the kinematic curves. This indicates that the glue component is rather thick, but we will return to this in Section 9.3.3.

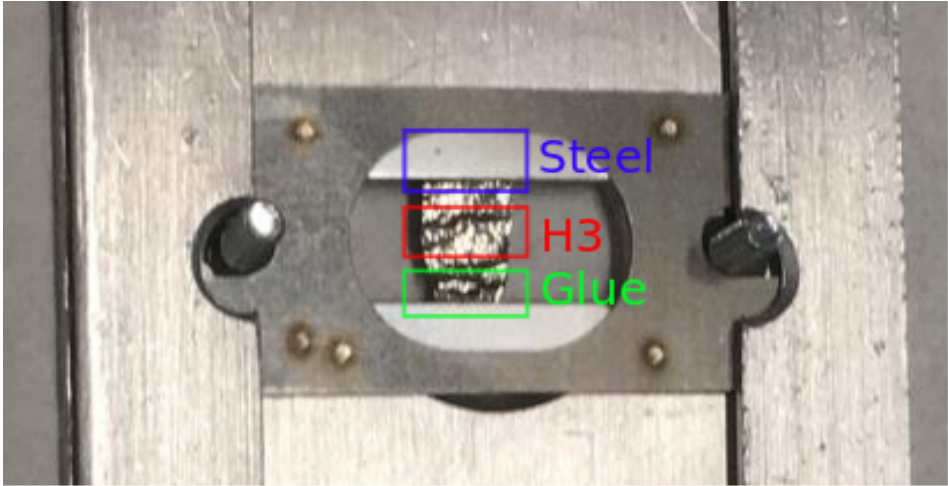


Figure 9.3: The target ladder slot with the  $^3\text{H}$  foil. The three regions were investigated is indicated by colored boxes.

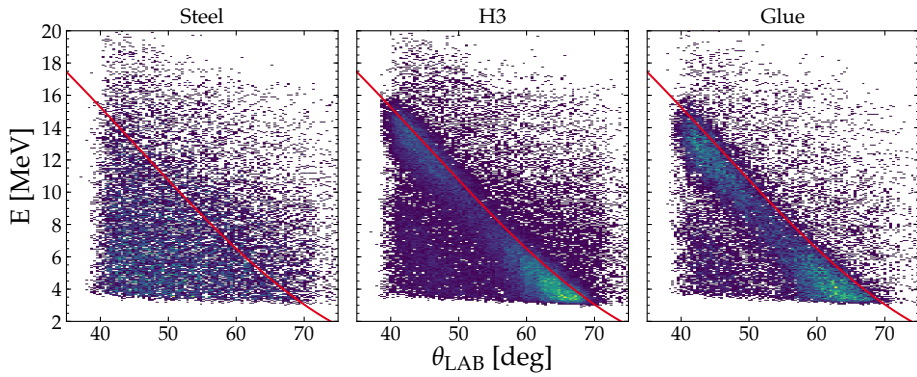


Figure 9.4: Kinematic curves for  $^9\text{Li}$  beam on the main target. The red curves corresponds to elastically scattered protons.



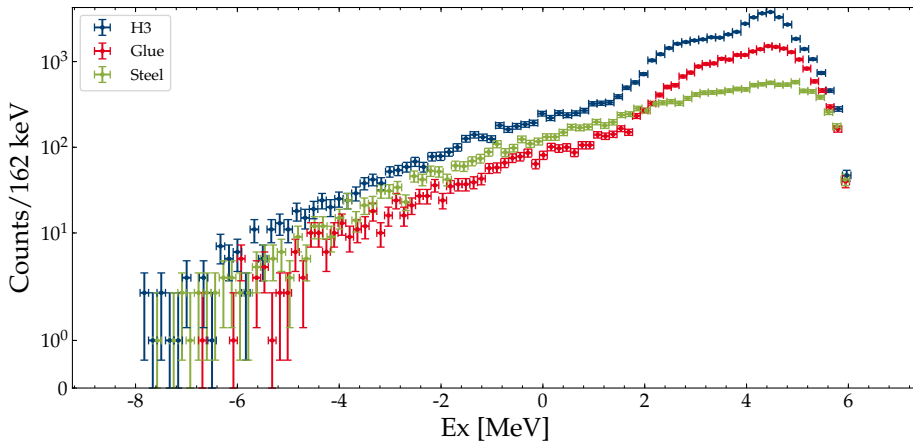


Figure 9.5: Excitations spectra for  $^{11}\text{Li}$  from measured protons in the three target regions, Steel, H3 and Glue.

The excitation spectra for the two neutron transfer to  $^{11}\text{Li}$  based on the protons are shown in Figure 9.5. Unfortunately, the different spectra are too similar between  $-1\text{ MeV}$ - $6\text{ MeV}$  and we can not do a background subtraction.

### 9.3.2 S3

The S3 detector gives a clearer picture of the situation. It is not possible to identify protons in this detector, but the elastically scattered  $^9\text{Li}$  stops as opposed to the light hydrogen isotopes. To simplify the analysis we restrict us to a single ring (a single strip, symmetric in  $\theta$ ). The uncalibrated energy spectra from the three regions as well as an energy spectrum from a measurement on the pure  $^{48}\text{Ti}$  are shown in Figure 9.6. Notice that the pure  $^{48}\text{Ti}$  target was not modified in preparations to this experiment, and therefore free of glue.

The spectrum for  $^3\text{H}$  has a clear peak at channel 2800, corresponding to scattered  $^9\text{Li}$ . At lower energies (channels), a feature appears, that resembles

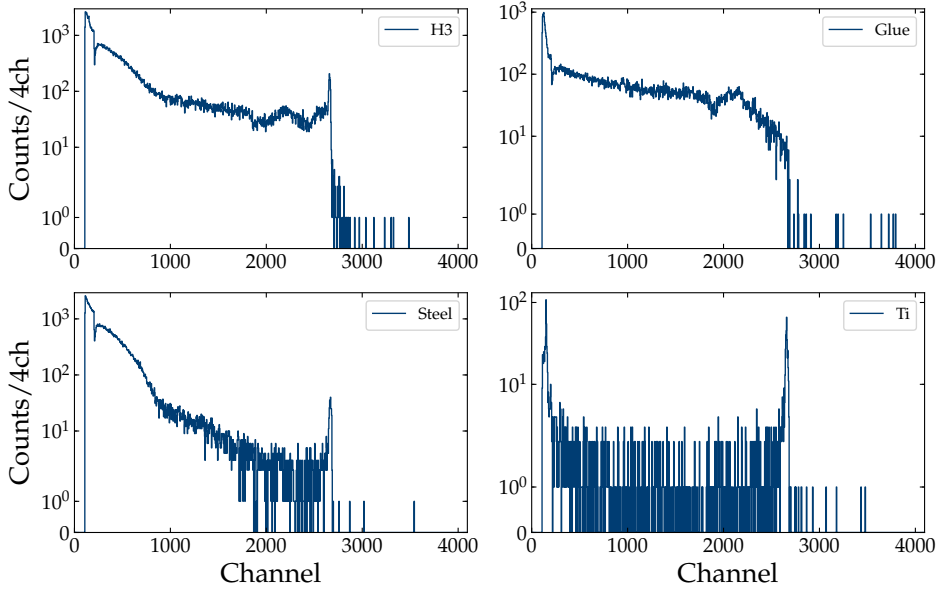


Figure 9.6: Spectra from a single ring (strip) in the S3 detector for different target configurations. Steel, H3, and glue all correspond, to the main target with contamination. The Ti-spectrum was measured with the clean background titanium target.

the feature around channel 2000 in the Glue spectrum. This is consistent with a smeared out elastic peak due to a large energy loss, which could very well result from a thick layer of glue. For channels below 1000, the spectrum has a feature that resembles the same region in the Steel spectrum. This feature falls off so quickly to also be present in the Glue spectrum.

Neither of these two features is present in the pure  $^{48}\text{Ti}$  spectrum. The three regions of the target ( $^3\text{H}$ , Glue and Steel) thus all seem to be largely dominated by reactions with the glue and steel.

Notice, how clean the pure Ti spectrum is. There is not much background from reactions with titanium.

### 9.3.3 Backward detectors

The elastic protons will not scatter beyond  $90^\circ$ , and they will therefore not contaminate the backward detectors. Reactions from  ${}^9\text{Li}$  with steel, the unknown components of glue and  ${}^{48}\text{Ti}$  may, however, give a sizeable but unknown contribution in the backward direction.

Without particle identification for such low-energetic protons, we must rely on energy cuts. The kinematics of the two neutron transfer reaction corresponds to proton-energies of 800 keV-1000 keV in the angular range of that detector for the ground state of  ${}^{11}\text{Li}$ . Since the protons do not penetrate the DSSD, a veto on the pad is included. The excitation spectrum for each detector in the range 450 keV-1500 keV is shown in Figure 9.7. The situation here is more or less the same, and we cannot distinguish the background components from the signal.

#### Trigger thresholds

Another issue with the backward detectors limited the effective coverage region. The trigger thresholds were, due to noise issues during the setup phase, simply set too high for the backward detectors. The *trigger efficiency*, that is the fraction of hits that produces a trigger at a certain energy, can be calculated from the TDC and ADC values. The TDC fires only when a given channel had a signal to trigger on. The ADC can, however, digitize non-zero values if the DAQ was triggered by another source. In a physics measurement, this could be a coincident particle or random noise.

The trigger efficiency can be measured more precisely with a pulser. The DAQ is configured to issue a global trigger on all pulses. At a given energy, i.e. pulse height, the shaper will generate a logic trigger signal and send it to the TDC if the signal passes the threshold for that channel. Different energies are thus simulated by varying the pulse height. If a particular channel produces a trigger as well as an energy signal it has 100 % efficiency. This is now repeated many times and the trigger efficiency for a given

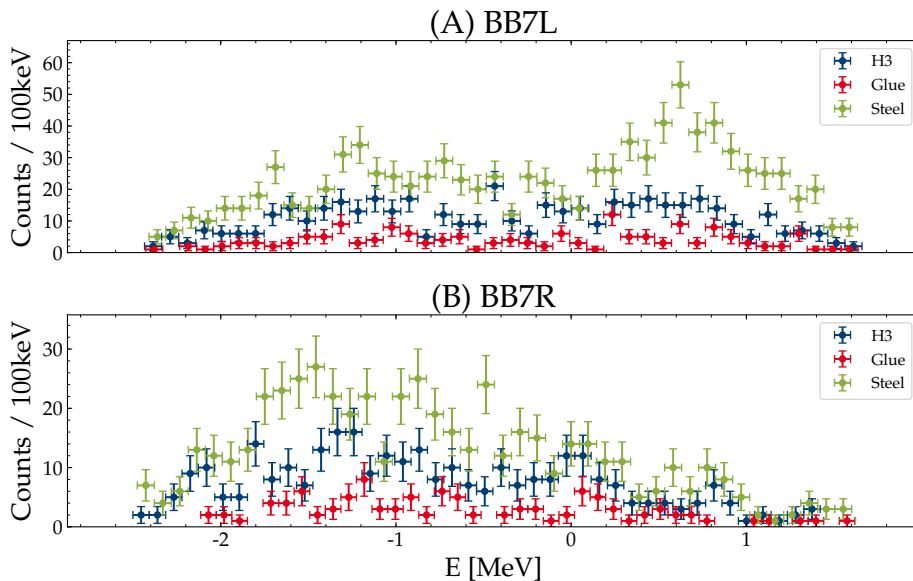


Figure 9.7: Excitation spectra for BB7L, (A), and BB7R, (B), from events that stopped in the DSSD assuming the reaction  ${}^9\text{Li}(t,p){}^{11}\text{Li}$ .

channel is

$$R_{\text{ch}} = \frac{N(TDC > 0 \text{ and } ADC > 0)}{N(ADC > 0)}. \quad (9.1)$$

The result of such a pulser measurement is shown in Figure 9.8 together with the efficiency measured from physics. Unfortunately, the efficiency vanishes below 1 MeV, which is the interesting region for protons. These detectors are thus not able to detect the protons of interest. When the efficiency is so close to zero, attempts to put an upper limit had huge uncertainties, and was therefore effectively useless.

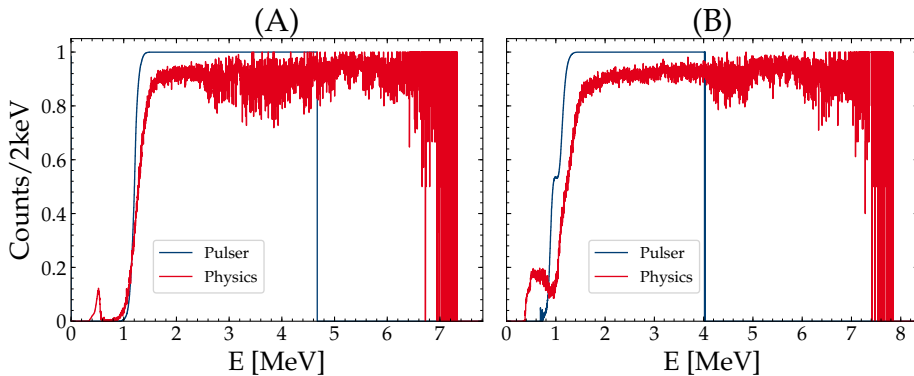


Figure 9.8: Trigger efficiency for BB7L, (A), and BB7R, (B). Both a pulser measurement as well as a physics measurement was performed.

### Thickness of contaminant

The thickness of the glue component can be estimated based on energy loss considerations of the identified particles in the pentagon. Ignoring any glue component, we obtain the kinematic curves shown in Figure 9.9 (A) and (B) for  ${}^9\text{Li}$  and  ${}^{12}\text{C}$  respectively. The curves correspond to the elastic scattering of protons in each case. The energy is clearly too low, i.e. there is missing some energy in the analysis.

Since the exact composition of glue is unknown, we model it as plastic. The target thus consists of a thin titanium foil and a  $90\ \mu\text{m}$  thick layer of plastic and the reaction is assumed to happen in the middle of the thick plastic layer, and the corresponding energy loss corrections are applied. The kinematic curves for the protons are shown in Figure 9.9 (C) and (D). The thickness was varied to make (C) and (D) consistent (considering that plastic is not the real material).

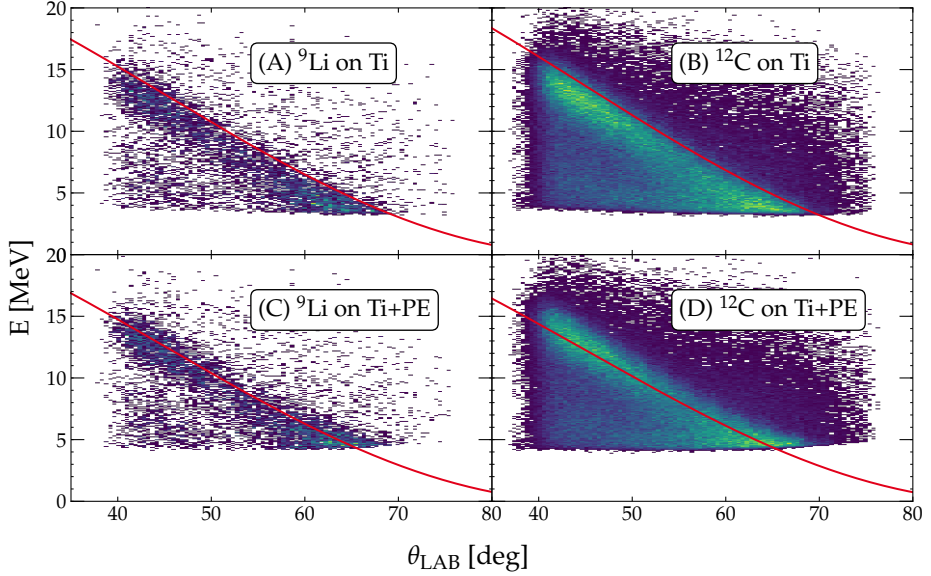


Figure 9.9: Kinematic curves for elastic protons. In (A) and (B) only a thin titanium target is assumed. In (C) and (D) a thick plastic layer was added and the energy corrections were done accordingly.

### 9.3.4 Intensity

There was no heavy target, in this experiment, due to target ladder limitations. This means no precise measurement of the intensity. The titanium target is too light for the  ${}^9\text{Li}$  beam to scatter according to the Rutherford distribution in our coverage region. The *grazing angle*, which is the transition angle from Coulomb interaction to nuclear interactions, for  ${}^9\text{Li}$ , is only  $9.1^\circ$  in LAB which is outside our coverage.

We can attempt a crude estimate of the intensity by extrapolating the scattering of  ${}^9\text{Li}$  on titanium into the Rutherford region. Beyond the grazing angle, the scattering shows Fresnel and Fraunhofer diffraction patterns. We can not resolve these patterns, but they do follow an exponential trend

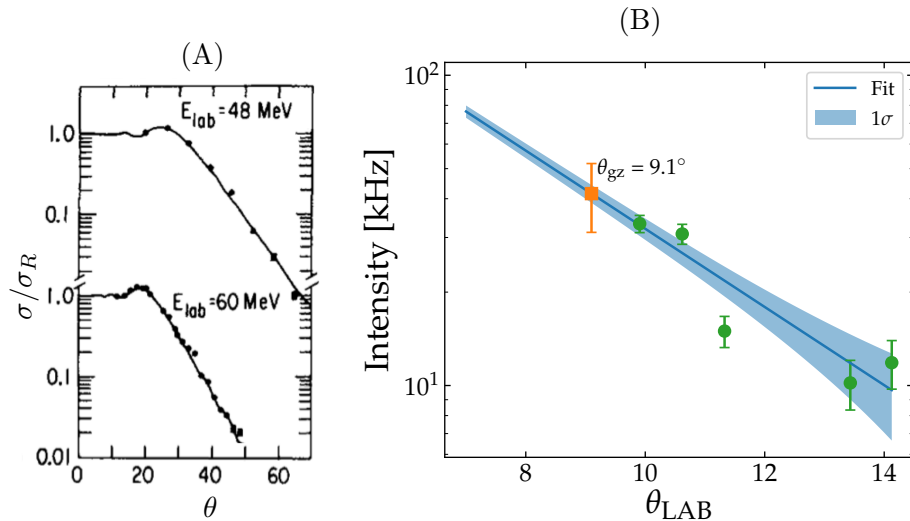


Figure 9.10: **(A)** Elastic scattering of  $^{13}\text{C}$  on  $^{40}\text{Co}$  [86]. Notice the exponential trend after the grazing angle around  $25^\circ$ . **(B)** The calculated intensity based on  $^9\text{Li}$  scattered off of  $^{48}\text{Ti}$ . The data is fitted to Eq. (9.2) and extrapolated to the grazing angle at  $9.1^\circ$ . The orange points are the intensity value of the fit at the grazing angle, and the error estimate is described in the main text.

[47]. For angles up to the grazing angle, scattering follows the Rutherford distribution. Above the grazing angle the ratio between a Rutherford distribution and the measured distribution scales as

$$\frac{d\sigma/d\Omega}{d\sigma_R/d\Omega} \propto e^{-\lambda(\theta-\theta_{gz})},$$

for angles  $\theta \geq \theta_{gz}$ . See Figure 9.10 (A) for an example of this behaviour taken from elastic scattering of  $^{13}\text{C}$  on  $^{40}\text{Co}$  [86].

The intensity can now be calculated by the method in 10.3, with one important difference. Since the angles are above the grazing angle, the

exponential factor will be carried on and the intensity estimate is instead

$$I' = I \cdot e^{-\lambda(\theta - \theta_{\text{gz}})}, \quad (9.2)$$

where  $I$  is the actual intensity.

We can now measure in a number of different angles and fit to Eq. (9.2) to determine  $\lambda$  and in particular the real intensity  $I$ , which corresponds to the value at  $\theta = \theta_{\text{gz}}$ .

There were a variety of problems with the S3 detector and in particular the calibrations. This meant that the matching algorithm discarded most of the elastic events. This analysis was therefore performed with the rings which are mostly symmetric in  $\theta$ . This omits the matching step and lets us identify the scattered particles by energy. Assuming that each ring corresponds to a single angle, we can plot the deduced intensity as a function of the central angle in each ring. See Figure 9.10 (B) for the data and the subsequent fit to Eq. (9.2). The fitted value is

$$I_{\text{fit}} = 41(3) \text{ kHz}, \quad (9.3)$$

where the error is derived from the fit. The orange dot indicates the value of the fit at the grazing angle, with the error estimate from the end of this section. There are several systematic errors, which must also be accounted for. First of all, the rings are not fully symmetrical, and using a single angle for a given ring does not reflect this. Secondly, we are averaging over the ring, which becomes more problematic as we approach  $0^\circ$ . Most importantly, however, is the gross simplification in the model. Many details about the diffraction pattern are left out. Lastly, the fit is not including many angles. Due to these systematics we take a slightly conservative approach and report an uncertainty of 25%.

$$I = 41(10) \text{ kHz}, \quad (9.4)$$

We did have a Faraday cup in, but it was not very accurate due to the low current, but the readings were consistent with this order of magnitude.



---

# Acceptance

Before the experimental results can be compared to theoretical predictions, they need to be transformed into absolute cross sections. In this chapter, I will discuss a transformation method based on Monte Carlo simulations to produce differential cross sections. To perform the simulations, I used the simulation package `simX`[55].

Most nuclear physics experiments count reactions. The counting numbers do, however, not only reflect the reaction probability, but also the target properties, the geometric coverage of our detectors, kinematics and more. This makes it difficult to compare results to other experiments with different setups and in particular to theoretical calculations that do not deal with geometrical particularities. Instead, the counting numbers are transformed to cross sections. This transformation depends, therefore, on all the geometrical properties of the setup and the beam, and it is called *acceptance*.

In principle, cross section can depend on many variables, but some are more interesting than others. We will thus limit this discussion to differential angular cross sections and differential energy cross section, or more generally the double differential cross section.

## 10.1 Differential cross section

For a given reaction the number of reactions is given by

$$N_R = N_I n_t \sigma, \quad (10.1)$$

where  $N_R$  is the number of reactions,  $N_I$  is the number of incident beam particles,  $n_t$  is the number of target particles per  $\text{cm}^2$  and  $\sigma$  is the integrated cross section for the reaction in units of  $\text{cm}^2$ . This can also be expressed as a differential cross section

$$\frac{d^2 N_r(\theta, \phi, E)}{d\Omega dE} = N_I n_t \frac{d^2 \sigma(\theta, \phi, E)}{d\Omega dE}. \quad (10.2)$$

The total number of detected particles can be calculated by integrating over the solid angle covered by the detectors,  $\Omega_S$ , and the length of the kinematically allowed energy interval,  $E_r$ .

To get the cross section from counting numbers, Eq. (10.2) can be re-arranged

$$\frac{d^2 \sigma(\theta, \phi, E)}{d\Omega dE} = \frac{1}{N_I n_t} \frac{d^2 N_r(\theta, \phi, E)}{d\Omega dE}. \quad (10.3)$$

It is not possible to measure infinitesimal counting numbers, angles or energies in an actual experiment. The data is instead binned using a suitable bin size, usually depending on the amount of statistics. Too small bins result in large uncertainties. Too big bins average out possibly interesting features. Either way, the cross section at each point in a given bin can be approximated with the average of the bin

$$\frac{d^2 \sigma(\theta, \phi, E)}{d\Omega dE} \approx \frac{1}{N_I n_t} \frac{N_r(\theta_i, \phi_i, E_i)}{\Delta\Omega \Delta E}, \quad (10.4)$$

where  $N_r$  is the number of reactions in a given bin,  $\Delta\Omega$  is the solid angle corresponding to the bin and  $\Delta E$  is the length of the energy interval covered by the bin. The subscript  $i$  on the RHS indicates that it is a bin, uniquely identified by one set of coordinates, for instance, the center of the bin. The corresponding coordinates on the LHS can now be any set of coordinates within the bin.

In reality, some bins will be outside of detector range and some will be suppressed due to kinematics. This can be thought of as if the effective size

of the bin is reduced. The ratio of detected particles to the effective size of the bin is, however, unchanged (within the resolution of the bin)

$$\frac{N_r(\theta_i, \phi_i, E_i)}{\Delta\Omega\Delta E} = \frac{N_r^d(\theta_i, \phi_i, E_i)}{\Delta\Omega'\Delta E'}, \quad (10.5)$$

where  $N_r^d(\theta_i, \phi_i, E_i)$  is the number of detected particles in the bin and  $\Delta\Omega'\Delta E'$  is the effective size of the bin. Substituting Eq. (10.5) back into Eq. (10.4) gives the estimated differential cross section,

$$\frac{d^2\sigma(\theta, \phi, E)}{d\Omega dE} \approx \frac{1}{N_I n_t} \frac{N_r^d(\theta_i, \phi_i, E_i)}{\Delta\Omega'\Delta E'}. \quad (10.6)$$

## 10.2 Monte Carlo

To get a reliable estimate of the cross section, each of the values on the right side of Eq. (10.6) must be evaluated.  $N_I$  and  $n_t$  does not depend on the geometric setup of the detectors or the reference frame.  $N_r^d$  is simply what is measured in the experiment.  $\Delta\Omega'$  and  $\Delta E'$  are, however, more difficult. As mentioned earlier, they depend on the geometry of the setup as well as the kinematics. Furthermore, the effects of a broad divergent beam, finite angular resolution in the detectors and the like, also affect the effective bin size. It is not easy to incorporate all these effects in an analytical way, but it can be solved with a Monte Carlo simulation.

Consider a simulation of a uniform distribution. A fraction of the simulated particles end up in each bin, proportional to the size of the bin

$$\frac{N_s(\theta_i, \phi_i, E_i)}{N_S} = \frac{\Delta\Omega\Delta E}{4\pi E_r}, \quad (10.7)$$

where  $N_s(\theta, E)$  is the number of simulated particle in a specific bin,  $N_S$  is the total number of simulated particles and  $E_r$  is the length of the energy interval we sample uniformly from.

The simulation can now be extended to include beam properties and the geometrical outline of the detector. By keeping track of how many particles

that are detected, we get a measure of the effective bin size

$$\frac{N_s^d(\theta_i, \phi_i, E_i)}{N_S} = \frac{\Delta\Omega' \Delta E'}{4\pi E_r}, \quad (10.8)$$

where  $N_s^d(\theta_i, \phi_i, E_i)$  is the detected amount of a the simulated reactions and  $\Delta\Omega' \Delta E'$  is the effective bin size. It is, however, *the same*  $\Delta\Omega' \Delta E'$  as in Eq. 10.6. The effective bin size  $\Delta\Omega' \Delta E'$  can now be isolated and substituted into Eq. (10.6)

$$\frac{d^2\sigma(\theta, \phi, E)}{d\Omega dE} \approx \frac{1}{n_t} \frac{N_S}{N_I} \frac{N_r^d(\theta_i, \phi_i, E_i)}{N_s^d(\theta_i, \phi_i, E_i)} \frac{1}{4\pi E_r}. \quad (10.9)$$

We may define the acceptance as the transformation from double differential cross sections to counting number in a given bin, given by

$$\mathcal{A}(\theta_i, \phi_i, E_i) = \frac{N_i n_t N_s^d(\theta_i, \phi_i, E_i) 4\pi E_r}{N_S}, \quad (10.10)$$

under the assumption that we can assign an average differential cross section to the whole bin.

The single differential cross sections can now be obtained by integration. The angular cross section reads

$$\begin{aligned} \frac{d\sigma(\theta, \phi)}{d\Omega} &\approx \int_E \frac{1}{n_t} \frac{N_S}{N_I} \frac{N_r^d(\theta_i, \phi_i, E_i)}{N_s^d(\theta_i, \phi_i, E_i)} \frac{1}{4\pi E_r} dE' \\ &= \frac{1}{n_t} \frac{N_S}{N_I} \sum_i \left( \frac{N_r^d(\theta_i, \phi_i, E_i)}{N_s^d(\theta_i, \phi_i, E_i)} \right) \frac{\Delta E}{4\pi E_r}, \end{aligned} \quad (10.11)$$

where the sum is over all energy bins and each bin are assumed to have the same width  $\Delta E$ .

Similarly for the differential energy cross section

$$\frac{d\sigma(E)}{dE} \approx \frac{1}{n_t} \frac{N_S}{N_I} \sum_i \left( \frac{N_r^d(\theta_i, \phi_i, E_i)}{N_s^d(\theta_i, \phi_i, E_i)} \Delta\Omega \right) \frac{1}{4\pi E_r}, \quad (10.12)$$

where  $\Delta\Omega$  is the solid angle of the bin.

Notice an important difference here. For the angular distribution, we could sum up all energies at a given angle, because each bin has the same weight ( $\Delta E$ ) and pull it outside the sum. For the energy distribution, however, we need to apply the weight ( $\Delta\Omega$ ), which consequently also scales the uncertainties.

### 10.2.1 Bound states

A similar analysis yields the single differential angular cross section of bound states. The simulation is thus only with a single energy, corresponding to the resonance energy, and the energy dependence  $\Delta E/E_r$  in Eq. (10.8) vanishes

$$\frac{d\sigma(\theta, \phi)}{d\Omega} \approx \frac{1}{n_t} \frac{N_S}{N_I} \frac{N_r^d(\theta_i, \phi_i)}{N_s^d(\theta_i, \phi_i)} \frac{1}{4\pi}. \quad (10.13)$$

## 10.3 Rutherford estimation

The same ideas can be used to estimate the intensity in an experiment based on Rutherford scattering.

Consider an experiment with a beam impinging on a heavy target with subsequent measurement of the scattered beam particles. Not all particles will interact with a target particle, and the distribution follows the well known Rutherford cross section in the center-of-mass frame [47]

$$\begin{aligned} \frac{d\sigma_R}{d\Omega}(\theta, \phi) &= \left( \frac{e^2}{4\pi\epsilon_0} \frac{zZ}{E} \frac{1}{\sin^2(\theta/2)} \right)^2 \\ &= \left( \frac{\alpha\hbar czZ}{4E} \frac{1}{\sin^2(\theta/2)} \right)^2 \\ &= \left( \frac{1.44\text{MeV} \cdot \text{fm}}{4E} \frac{zZ}{\sin^2(\theta/2)} \right)^2, \end{aligned} \quad (10.14)$$

where  $z$  is the charge of the beam particles,  $Z$  is the charge of the target and  $E$  is the available energy in the CM system

$$E = E_{\text{LAB}} \frac{m_{\text{target}}}{m_{\text{target}} + m_{\text{beam}}}. \quad (10.15)$$

The measured number of beam particles is

$$N_R = N_I n_t \int_{\Omega_{\text{setup}}} \frac{d\sigma_R}{d\Omega}(\theta, \phi) d\Omega' \quad (10.16)$$

where  $N_I$  is the total number of the incoming beam,  $n_t$  is the target density.

Notice the integration of the Rutherford cross section over  $\Omega_{\text{setup}}$  which is the solid angle covered by the setup. A re-arrangement of Eq. (10.16) gives the number of incoming beam particles

$$N_I = \frac{N_R}{n_t \int_{\Omega_{\text{setup}}} \frac{d\sigma_R}{d\Omega}(\theta, \phi) d\Omega'}. \quad (10.17)$$

We can now use two different strategies to determine  $\Omega_{\text{setup}}$ . The first method is a Monte Carlo method like the one we used in the previous section. This method makes it easy to incorporate imperfect beams, etc. The second is a simpler geometrical method, which is good to consistency check, but lacks the sophistication that a simulation can provide.

### 10.3.1 Monte Carlo

In the Monte Carlo method,  $N_S$  reactions are simulated and distributed according to the Rutherford formula. The number of detected particles are also counted,  $N_s^d$ . Notice that the simulation does not need to cover the full angular range. In particular, the Rutherford distribution diverges when  $\theta \rightarrow 0$ , and there should be a cutoff  $\theta_{\text{min}}$ .

The ratio of detected scattered beam particles (analogous to Eq. (10.8)) to simulated particles is

$$\frac{N_s^d}{N_S} = \frac{\int_{\Omega_{\text{setup}}} \frac{d\sigma_R}{d\Omega}(\theta, \phi) d\Omega'}{\int_{\theta > \theta_{\text{min}}} \frac{d\sigma_R}{d\Omega}(\theta, \phi) d\Omega'} = \frac{\int_{\Omega_{\text{setup}}} \frac{d\sigma_R}{d\Omega}(\theta, \phi) d\Omega'}{2\pi \int_{180}^{\theta_{\text{min}}} \frac{d\sigma_R}{d\Omega}(\theta, \phi) \sin\theta d\theta'}, \quad (10.18)$$

which can be rearranged to

$$\int_{\Omega_{\text{setup}}} \frac{d\sigma_R}{d\Omega}(\theta, \phi) d\Omega' = \frac{N_s^d}{N_S} 2\pi \int_{180}^{\theta_{\text{min}}} \frac{d\sigma_R}{d\Omega}(\theta, \phi) \sin\theta d\theta' \quad (10.19)$$

and plugged back into Eq. (10.17) to get

$$N_I = \frac{N_r N_S}{2\pi n_t N_s^d} \frac{1}{\int_{180}^{\theta_{\text{min}}} \frac{d\sigma_R}{d\Omega}(\theta, \phi) \sin\theta d\theta'} \quad (10.20)$$

### 10.3.2 Geometric

The solid angle of the individual pixels can also be calculated with a simple geometric approximation where each pixel is projected onto the tangent plane of the unit sphere. The solid angle is thus the area on this plane. If the pixels are small enough, this is a sufficiently good approximation.

The Rutherford cross section in LAB is given as

$$\frac{d\sigma_R^{\text{LAB}}}{d\Omega}(\theta, \phi) = \left( \frac{zZ\alpha\hbar c}{2E} \right)^2 \cdot \frac{\left( \cos\theta + \sqrt{1 - \left( \frac{m_1}{m_2} \sin\theta \right)^2} \right)^2}{\sin^4\theta \sqrt{1 - \left( \frac{m_1}{m_2} \sin\theta \right)^2}},$$

and multiplying with the solid angle of the pixel yields

$$\int_{\Omega_{\text{setup}}} \frac{d\sigma_R}{d\Omega}(\theta, \phi) d\Omega' \approx \sum_{\text{pixels}} \frac{d\sigma_R^{\text{LAB}}}{d\Omega}(\theta_{\text{pixel}}) \Omega_{\text{pixel}}. \quad (10.21)$$

Plugging back into Eq. (10.17) gives

$$N_I = \frac{N_r}{n_t \sum_{\text{pixels}} \frac{d\sigma_R^{\text{LAB}}}{d\Omega}(\theta_{\text{pixel}}) \Omega_{\text{pixel}}} \quad (10.22)$$





---

# Scattering theory

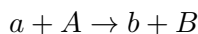
To extract physics from the experimental results, we need to compare with theoretical models. These models should be able to describe the reaction mechanism as well as the internal structure of the reaction constituents and it is thus important that a description can include both in a consistent way.

In this chapter I will present the main results of the scattering theory used to compare the data in Chapter 13. The sections are based on notes by A. Moro[87], but it is described in multiple textbooks and notes such as [47, 88–90].

I have used the **fresco** software [91] to carry out calculations. I have used the publicly available version as well as a slightly modified version by A. M. Moro [92].

## 11.1 General scattering

The problem of scattering is generally well understood. Consider the situation with a beam particle  $a$  impinging on a target  $A$  resulting in two outgoing fragments  $b$  and  $B$



The scattering is described by the total wavefunction of the system which is governed by the interaction between the projectile and the target

via the time-independent Schrödinger equation

$$[\hat{T}_{\vec{R}} + H_a(\xi_a) + H_A(\xi_A) + V(\vec{R}, \xi_a, \xi_A) - E]\Psi(\vec{R}, \xi_a, \xi_A) = 0 \quad (11.1)$$

where  $\hat{T}_{\vec{R}}$  is the kinetic operator,  $H_a(\xi_a)$  and  $H_A(\xi_A)$  are the internal Hamiltonians of the projectile and target with corresponding solutions  $\Phi_a(\xi_a)$  and  $\Phi_A(\xi_A)$ . The interaction is  $V(\vec{R}, \xi_a, \xi_A)$  and  $\Psi(\vec{R}, \xi_a, \xi_A)$  is the total wavefunction. The internal coordinates of the projectile and the target are denoted  $\xi_a$  and  $\xi_A$ . The total energy of the system is the sum of kinetic and internal energies.

To keep track of rearrangement processes and to simplify the notation, a particular set of nuclei are denoted a *mass partition*. This could, for instance, be the incoming mass partition,  $a + A$ . Inelastic scattering, the initial and final mass partition are identical, whereas a transfer reaction will have a different final mass partition. The projectile-target mass partition will be denoted  $\alpha$ . The internal coordinates of the the mass partition is combined into  $\xi_\alpha$  and the wavefunction of the incoming mass partition is  $\Phi_\alpha(\xi_\alpha) = \Phi_a(\xi_a)\Phi_A(\xi_A)$

The solution to Eq. (11.1),  $\Psi(\vec{R}, \xi_a, \xi_A)$ , contains the full description of the scattering process. During the reaction, the wavefunction is highly distorted due to the interaction, but asymptotically the solution will be an eigenstate of the projectile and target, as the interaction becomes negligible.

The incident projectile can be represented as a plane wave approaching the target. During the collision the wave will be distorted which generates spherically outgoing waves. If there is no rearrangement of nucleons the asymptotic solution include three main contributions.

A plane wave corresponding to incoming particles that did not react, elastic scattering and inelastic scattering, where the excited state of the mass partition  $\alpha$  is denoted  $\alpha'$ .

$$\Psi^{(+)} \rightarrow \Phi_\alpha(\xi_\alpha)e^{i\vec{K}\cdot\vec{R}} + \Phi_\alpha(\xi_\alpha)f_{\alpha\alpha}(\theta)\frac{e^{iKR}}{R} + \sum_{\alpha' \neq \alpha} \Phi_{\alpha'}(\xi_\alpha)f_{\alpha'\alpha}(\theta)\frac{e^{iKR}}{R}, \quad (11.2)$$

where (+) refers to outgoing boundary conditions.  $f_{fi}(\theta)$  is the so-called *scattering amplitude* from initial state  $i$  to final state  $f$ . If the final state is a different mass partition,  $\beta$  the plane wave vanishes and asymptotically

$$\Psi^{(+)} \rightarrow \sum_{\beta \neq \alpha} \Phi_{\beta}(\xi_{\beta}) f_{\beta\alpha}(\theta) \frac{e^{iKR}}{R}. \quad (11.3)$$

The differential angular cross section can be calculated from the scattering amplitude [93]

$$\frac{d\sigma}{d\Omega_{\alpha \rightarrow \beta}} = \frac{v_{\beta}}{v_{\alpha}} |f_{\beta\alpha}(\theta)|^2, \quad (11.4)$$

where  $v_{\alpha}$  and  $v_{\beta}$  are the asymptotic velocities. This can also be expressed in terms of the *transition matrix*

$$\mathcal{T}_{\beta\alpha} = -\frac{2\pi\hbar^2}{\mu_{\beta}} f_{\beta\alpha}(\theta). \quad (11.5)$$

It can be shown that by introducing an auxiliary potential  $U_{\beta}$ , which in principle can be arbitrary, there exists an integral form of the transition matrix [93]

$$\mathcal{T}_{\beta\alpha} = \mathcal{T}_{\beta\alpha}^{(0)} \delta_{\beta\alpha} + \left\langle \chi_{\beta}^{(-)*}(\vec{K}, \vec{R}) \phi_{\beta}(\xi_{\beta}) \left| V - U_{\beta} \right| \Psi_{\alpha}^{(+)} \right\rangle, \quad (11.6)$$

where the first term is the elastic scattering due to  $U_{\beta}$  and vanishes if  $\beta \neq \alpha$ . Notice that this is in a post-form, meaning the interaction  $V$  should be appropriate for the  $\beta$  partition. Furthermore is  $\chi_{\beta}^{(-)}$  the time-reversed of  $\chi_{\beta}^{(+)}$  which is the solution to

$$[\vec{T}_{\beta} + U_{\beta} + \epsilon_{\beta} - E] \chi_{\beta}^{(+)}(\vec{K}, \vec{R}) = 0. \quad (11.7)$$

Notice that this can also be written in a prior form and by omitting the elastic part it reads

$$\mathcal{T}_{\beta\alpha} = \left\langle \Psi_{\beta}^{(-)} \left| V - U_{\alpha} \right| \chi_{\alpha}^{(+)}(\vec{K}, \vec{R}) \phi_{\alpha}(\xi_{\alpha}) \right\rangle, \quad (11.8)$$

It is the aim to find the scattering amplitude in order to subsequently calculate the cross section. Until now, the results are still exact. The challenge is that they require the full wavefunction for either the initial or final mass partition. This can in general not be solved and suitable approximations are required.

## 11.2 Optical potential

The simplest approximation is to only consider the elastic scattering. This is called the Optical Model (OM). In this approximation, only the elastic channel is calculated, and all other channels are treated as loss of flux from the elastic channel. The effective Hamiltonian for this system is

$$H_{\text{eff}} = H_{\alpha} + U_{\alpha}(R), \quad (11.9)$$

where  $U_{\alpha(R)}$  is a complex effective potential. The real part of the interaction accounts for the elastic scattering whereas the complex part accounts for the couplings to all other states by removing flux.

The optical potential,  $U_{\alpha(R)}$ , is usually determined phenomenologically by fitting some parametrization to experimental data. The shape of the parametrization is generally the same but the parameters depend on the reaction and the energy. There exist many different parametrizations of the optical potential parameters across the literature which are fitted to data within different energy and isotope ranges. See RIPL [94] for a comprehensive collection.

The analytical form of the optical potential is usually a sum of a Coulomb and a central nuclear interaction. If one of the particles is a neutron, the Coulomb part naturally vanishes. The Coulomb part corresponds to a uniform distribution of charges with radius  $R_c$

$$U_C(R) = \begin{cases} \frac{Z_p Z_t e^2}{2R_c} \left( 3 - \frac{R^2}{R_c^2} \right) & \text{if } R \leq R_c \\ \frac{Z_p Z_t e^2}{R} & \text{if } R > R_c \end{cases} \quad (11.10)$$

The nuclear part is very similar to the shell model, and the Woods-Saxon form is thus used

$$f(r, R, a) = \frac{1}{1 + e^{\frac{r-R}{a}}} \quad (11.11)$$

The idea is the same, namely that the interaction can be described as a mean-field of nucleons, and the Woods-Saxon give a realistic shape defined through three parameters, the depth,  $V_r$ , the radius,  $r_r$ , and the diffuseness,  $a_r$

$$U_N(r) = -V_r f(r, r_r, a_r) \quad (11.12)$$

The nucleon states at the surface of the nuclei are typically easier to interact with. In a shell model picture, these correspond to lastly occupied nucleon states. They can, in the shell model picture, easily be excited into higher energy states. They can even be knocked out or the projectile may transfer one or more nucleons to empty states. An imaginary surface term is therefore normally included and is a derivative of a Woods-Saxon

$$U_S(r) = 4i \frac{d}{dr} W_i f(r, r_i, a_i). \quad (11.13)$$

The last part, which was also the key ingredient in the shell model to reproduce the magic numbers, is the spin-orbit coupling. Similarly to the shell model it has the form

$$U_{ls}(r) = V_{sl} \left( \frac{\hbar}{m_\pi c} \right)^2 \frac{1}{r} \frac{d}{dr} f(r, r_{ls}, a_{ls}) (2\vec{l} \cdot \vec{s}), \quad (11.14)$$

where the imaginary part is usually zero and thus omitted.

### 11.3 Coupled-channels method

A more difficult task is to include inelastic reactions. In this case, the coupling to one or more excited states needs to be taken into account. This

problem can be formally treated with the coupled-channels method (CC). The Hamiltonian is again given as

$$H = T_\alpha(\vec{R}) + H_\alpha(\xi_\alpha) + V_\alpha(\xi_\alpha, \vec{R}), \quad (11.15)$$

where  $\vec{R}$  is the relative coordinate between  $a$  and  $A$ . For simplicity, it is only the projectile that can be excited.

The total wavefunction can now be expanded in the complete set of eigenstates for the projectile  $\phi_n(\xi_a)$

$$\Psi(R, \xi_a) = \phi_0(\xi_a)\chi_0(\vec{R}) + \sum_{n>0} \phi_n(\xi_a)\chi_n(\vec{R}), \quad (11.16)$$

where the coefficients  $\chi_n(\vec{R})$  describes the relative probability at a given  $\vec{R}$  for the projectile to be in state  $n$ .

The Hamiltonian in Eq. (11.15) and the expansion in Eq. (11.16) can now be inserted into the Schrödinger equation

$$[E - H]\Psi(\vec{R}, \xi_a) = 0. \quad (11.17)$$

Multiplying  $\phi_n^*$  on each side and integrating over  $\xi_a$  yields a set of differential equations of the form

$$\left[ E - \epsilon_n - \vec{T}_{\vec{R}} - V_{n,n}(\vec{R}) \right] \chi_n(\vec{R}) = \sum_{n' \neq n} V_{n,n'}(\vec{R}) \chi_{n'}(\vec{R}), \quad (11.18)$$

where  $V_{n,n'}(\vec{R})$  are *coupling potentials* defined by

$$V_{n,n'}(\vec{R}) = \int d\xi_a \phi_n^*(\xi_a) V(\xi_a, \vec{R}) \phi_{n'}(\xi_a). \quad (11.19)$$

Each of these potentials gives rise to the excitation from one state to another. The potentials must, however, be constructed within some model  $V(\xi_a, \vec{R})$ . This could, for instance, be a rotor model or Coulomb excitation.

The solution to the coupled equations can be difficult if there are many states available. Often, however, the excited states can be treated perturbatively because they interact rather weakly with the ground state. The

total interaction is thus mainly governed by an average potential accounting for elastic scattering,  $V_0(\vec{R})$ . Notice it does not depend on the internal coordinates. A small perturbation to this potential accounts for the excitations  $\Delta(\vec{R}, \mathbf{x}_a)$ . The assumption in the *Distorted Wave Born Approximation* (DWBA) is that this perturbation is small, such that  $V_0(\vec{R})$  describes the elastic scattering well.

## 11.4 CDCC

If the excitation crosses the breakup threshold of the final state, the model space must be extended to encompass these breakup states. This is also the case for unbound systems such as  $^{10}\text{Li}$ . In principle, the CC methods can handle this but there are a few challenges. Firstly the breakup leads to states that are continuous in energy and thus an infinite number of states. If it is a weakly bound nucleus, the DWBA assumption does not hold, since the reaction probability is substantial. Secondly, such unbound states do not vanish at large distances. Asymptotically they keep oscillating making it unfeasible to calculate the coupling potential integrals.

One approach to solve this is by discretizing the continuum into energy bins and treat these bins as states which can be coupled. This leads to the continuum-discretized coupled-channels (CDCC) method, developed by Rawitscher[95] and later refined[96, 97].

Consider again a reaction with mass partition  $a + A$ . However, this time  $a$  consists of a valence nucleon  $x$  and a core  $c$ ,  $a = c + x$ . In the case of deuteron breakup,  $a$  could be the deuteron with  $x$  being the neutron and  $c$  being the proton. In the case of  $^{10}\text{Li}$  the core would now be  $^9\text{Li}$  with a valence neutron. The idea in the CDCC method is to discretize the continuum of  $a$  into bins and assume an effective three-body Hamiltonian on the form

$$H = H_a + T_{\vec{R}} + U_{cA}(\xi_{cA}) + U_{xA}(\xi_{xA}), \quad (11.20)$$

where  $H_a$  is the internal Hamiltonian of the composite system  $a$  (the deuteron for instance) and  $U_{cA}(\xi_{cA}) + U_{xA}(\xi_{xA})$  are optical potentials describing elastic

scattering of the core-target and valence-target systems.

For a spinless core (assumed for simplicity), the bins are denoted

$$\phi_i(\vec{r}) = \frac{u_i(\vec{r})}{r} [Y_{l_i}(\hat{r}) \otimes \chi_s]_{j_i m_i}, \quad (11.21)$$

where each bin,  $i$ , is characterized by the wave number interval  $[k_i, k_{i+1}]$ , the orbital angular momentum between the valence and the core  $\vec{l}$ , the valence spin  $\vec{s}$  and the coupling between the two  $\vec{j} = \vec{l} + \vec{s}$ . The radial part is a linear combination of scattering states

$$u_i(\vec{r}) = \sqrt{\frac{2}{\pi N_i}} \int_{k_i}^{k_{i+1}} w_i(k) u_{kl_i s j_i}(\vec{r}) dk, \quad (11.22)$$

where  $w_i(k)$  is a weight function, which is usually unity in case of a non-resonant continuum and  $N_i$  is a normalization constant. The average damps the oscillations at large distances, making the wave function in the bin normalizable.

The wavefunction can now be expanded in terms of the eigenstates of the  $a$  system including the discretized continuum. If there were only a single bound state,  $\phi_0$ , and the discretized continuum,  $\phi_i$ , the CDCC function is

$$\Psi^{\text{CDCC}}(\vec{R}, \vec{r}) = \chi_0^+(\vec{R}) \phi_0(\vec{r}) + \sum_{i=1}^N \chi_i^+(\vec{R}) \phi_i(\vec{r}), \quad (11.23)$$

which give rise to a set of coupling potentials, just like in the CC method

$$U_{ij}(\vec{R}) = \int \phi_i^* [U_{cA} + U_{xA}] \phi_j(\vec{r}). \quad (11.24)$$

The task is now to solve this set of coupling potentials, which in turn yields the coefficients  $\chi_i(\vec{R})$ , as described in Eq. (11.18). With  $\Psi^{\text{CDCC}}$  the transition matrix can readily be calculated. This procedure is performed by **fresco**.



Once the wavefunction has been established, the differential cross section can be calculated by combining Eq. (11.4) and Eq. (11.5). This can be extended to double differential cross sections by considering the energy bins

$$\left. \frac{d^2\sigma}{dE d\Omega} \right|_{E \in E_i} \approx \frac{1}{\Delta E_i} \frac{d\sigma}{d\Omega}, \quad (11.25)$$

where  $E_i$  defines an energy bin and  $\Delta E_i$  is the width of the bin.



---

## Population of $^{10}\text{Li}$

In this chapter, I present the structure model of  $^{10}\text{Li}$  and discuss the one neutron transfer reaction. Due to the system being unbound, it is important to consider what the theoretical framework actually describes both in terms of the structure and the reaction mechanism. In the end, I will discuss some kinematic considerations which can help us assess whether the theoretical framework is appropriate.

### 12.1 Structure of $^{10}\text{Li}$

The structure of  $^{10}\text{Li}$  is in principle a matter of understanding the continuum behavior of a neutron and  $^9\text{Li}$ . As mentioned in the introduction, it is a key ingredient to understand  $^{11}\text{Li}$ . The structural model ties into the CDCC scattering framework, which is used to describe the transfer reaction. The reaction will be discussed further in the next section.

The structure of  $^{10}\text{Li}$  is essentially given by the full wavefunction of the  $n^9\text{Li}$  system, which can be in a superposition of eigenstates of the  $^{10}\text{Li}$  Hamiltonian.

$$H = \vec{T} + H_{9\text{Li}} + H_n + V_{n^9\text{Li}}, \quad (12.1)$$

where  $V_{n^9\text{Li}}$  describes the  $n^9\text{Li}$  interaction that constitutes  $^{10}\text{Li}$ . In this thesis, I have adopted the model developed in [98] and applied to (d,p)

	$v_c^l$	$v_{\text{so-v}}^l$	$v_{\text{so-c}}^l$	$v_{\text{ss}}^l$
l=0	-5.4	-	-	-4.5
l=1	260.75	300.0	1.0	1.0
l=2	229.5	-300.0	-1.0	-7.5

Table 12.1: Parameters used in the structure for  $^{10}\text{Li}$ . All values are in MeV. Notice the signs of the spin terms are tuned to reproduce a specific ordering of the resonances.

reactions with  $^9\text{Li}$  in [32], which employs the following  $l$ -dependent structure

$$V_{n^9\text{Li}}^l = V_c^l(r) + V_{\text{so-v}}^l(r)\vec{l} \cdot \vec{s}_n + V_{\text{so-c}}^l(r)\vec{l} \cdot \vec{I} + V_{\text{ss}}^l(r)\vec{s}_n \cdot \vec{I}, \quad (12.2)$$

where  $\vec{s}_n$  is the spin of the neutron,  $\vec{I}$  is the spin of the  $^9\text{Li}$  core and  $l$  is the angular momentum between  $^9\text{Li}$  and the neutron.

This model includes a central radial term as well as spin-orbit and spin-spin terms. The radial functions are Gaussian

$$V_i^l(r) = v_i^l e^{-(r/R)^2},$$

with  $R = 2.55$  fm. The  $v_i^l$  values are chosen to reproduce several key features, and the full set of parameters can be seen in Table 12.1

- A virtual s-wave character of the  $2^-$  state [98].
- A splitting of the two  $p$ -states with a centroid close to 0.5 MeV. The sequence of the two states is arbitrary but was chosen to be consistent with [99]. It turns out, however, that the shape of the combined  $p$ -centroid was not sensitive to the ordering.
- A  $d$ -wave resonance around 4 MeV.

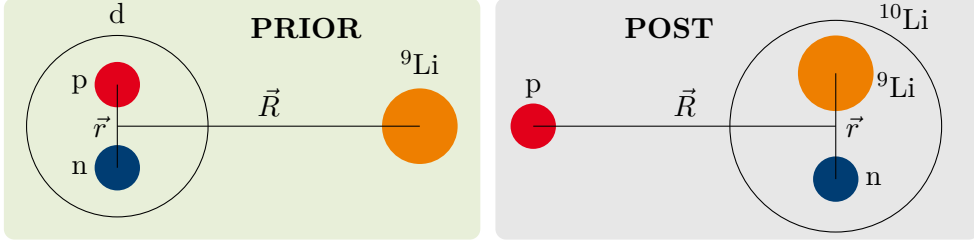


Figure 12.1: Schematic representation of the three-body configuration in a prior description and in a post description. In the prior (left) the internal coordinates  $\vec{r}$  is the relative coordinate between the proton and neutron in the deuteron. In the post (right)  $\vec{r}$  is the relative coordinate between the neutron and  ${}^9\text{Li}$ .

## 12.2 Transfer reaction

Consider a one neutron transfer from a deuteron to  ${}^9\text{Li}$ . Schematically it can be represented as shown in Figure 12.1. The transition matrix can be written in both a post or a prior form

$$\mathcal{T}^{\text{prior}} = \left\langle \Psi_f^{(-)}(\vec{R}, \vec{r}) \left| V_{n{}^9\text{Li}} + U_{p{}^9\text{Li}} - U_{d{}^9\text{Li}} \right| \phi_d(\vec{r}) \chi_{d{}^9\text{Li}}^{(+)}(\vec{R}) \right\rangle \quad (12.3)$$

$$\mathcal{T}^{\text{post}} = \left\langle \phi_{10\text{Li}}(\vec{r}) \chi_{p10\text{Li}}^{(-)}(\vec{R}) \left| V_{pn} + U_{p{}^9\text{Li}} - U_{n10\text{Li}} \right| \Psi_i^{(+)}(\vec{R}, \vec{r}) \right\rangle \quad (12.4)$$

Using the method of the CDCC, one of the two representations must be chosen, and the approximate CDCC-wavefunction can be generated. It turns out that the prior representation is the only one that is numerically stable. The CDCC-wavefunction is generated by expanding the exact wavefunction in the continuum bins of the core-valence system. In the post representation, the  $V_{pn}$  interaction dominates at small  $pn$  distances, but the coordinates that are integrated are the  $n{}^9\text{Li}$  and  $p{}^{10}\text{Li}$ . Given the fact that the  $n{}^9\text{Li}$  is a continuum, there is no physical cutoff of the interaction, and thus the numerical integration becomes ill-defined. In the prior representation, on the

other hand, the  $p^9\text{Li}$  interaction vanishes rather quickly, and a well-defined integration region in  $\vec{R}_{prior}$  is required.

The CDCC wavefunction in the prior form can now be generated from the  $^{10}\text{Li} = n + ^9\text{Li}$  continuum. The  $^{10}\text{Li}$  states are denoted as

$$\psi_{^{10}\text{Li}}^{i,J,M}(\xi_{^9\text{Li}}, \vec{r}) = \left[ \phi_I(\xi_{^9\text{Li}}) \otimes \varphi_{i,l,j}(\vec{r}) \right]_{J,M}$$

where  $\phi_I(\xi_{^9\text{Li}})$  is the internal wavefunction of  $^9\text{Li}$  and  $\varphi_{i,l,j}(\vec{r})$  is the relative  $n^9\text{Li}$  wavefunctions

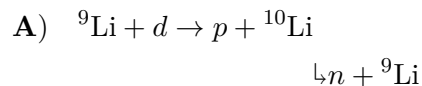
$$\Psi_f^{(-)}(\vec{R}, \vec{r}) \approx \sum_{i,J^\pi} \chi_{i,J^\pi}(\vec{K}_i, \vec{R}_i) \psi_{^{10}\text{Li}}^{i,J,M}(\xi_{^9\text{Li}}, \vec{r}),$$

where  $\vec{K}_i$  is the final momentum of the outgoing proton. This expansion gives rise to a number of coupled equations for the unknowns  $\chi_{i,J^\pi}(\vec{K}_i, \vec{R}_i)$ , which can be solved. This task is performed by **fresco**.

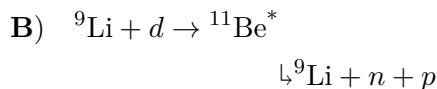
### 12.3 Alternative reaction mechanisms

There might be other reaction mechanisms than the one outlined in the previous section that contributes with a proton in the final state. In principle, these different reactions mechanisms are all different classical ways of thinking about the three-body system with a neutron, a proton, and a  $^9\text{Li}$ . The full wavefunction should in principle contain all information about the reaction. However, different approximations, favor different "parts" of the wavefunction and subsequent overlaps, what we refer to as the reaction mechanisms.

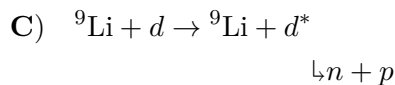
The model we use favors the sequential reaction where the neutron is firstly transferred to the  $^9\text{Li}$  core due to the  $n^9\text{Li}$  interaction which subsequently breaks up. We will refer to this as our main reaction channel



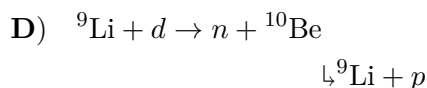
The deuteron impact may also create a compound nucleus that eventually breaks up. This is not the only channel that can eject a proton, but if we measure a coincident  ${}^9\text{Li}$  as well, this is the only reaction that has the correct final state.



The simple breakup of the deuteron, without any core interaction with  ${}^9\text{Li}$  also ejects a proton



It may in fact not be a neutron transfer, but rather a proton transfer. In this case, the resulting  ${}^{10}\text{Be}$  may be unstable to proton emission and we end up in the same final state as previous.



In a semi-classical picture, the kinematics is different in each of these cases. In **A)** the proton and  ${}^{10}\text{Li}$  will part, moving away from each other. When  ${}^{10}\text{Li}$  breaks up, the neutron and  ${}^{10}\text{Li}$  will be closer to each other, following their center of mass. This is in stark contrast with situation **C)**

where the break up of the deuteron will let the proton and the neutron off in the same direction, opposite to  $^9\text{Li}$ .

In situation **B)** the breakup will not be governed by two sequential stages with different kinematics, but rather populate the phase-space. Lastly in **D)**, a proton transfer will have very different kinematics for the proton than a neutron transfer since the proton will now share center-of-mass with  $^9\text{Li}$  in the first stage.

These considerations are worth testing experimentally by measuring the correlation between the particles. This, however, requires the detection of at least two of the constituents. As we will see later, this was only achieved in the first experiment at IS367. We will return to the interpretation of these results in Chapter 13.



---

## Results

In this chapter, we will attempt to piece together the structure of  $^{10}\text{Li}$  based on the experimental results from IS367, IS561A and IS561C, guided theoretically by the scattering framework presented in Section 11.

The CDCC calculation requires optical potentials for several interactions such as  $U_{d^9\text{Li}}$  and  $U_{p^9\text{Li}}$ . These reactions were measured in the experiments, and the first step is extracting these potentials from the data. Besides the optical model, we will also attempt a CDCC calculation for the elastic scattering of deuterons off of  $^9\text{Li}$ .

Based on these optical potentials we can perform the CDCC calculation for the neutron transfer reaction and compare with the experimental results.

The experimental excitation spectrum and angular distribution for  $^{10}\text{Li}$  are firstly based on measurements of the ejected proton, inferring the excitation spectrum from the missing energy. The neutron transfer process is, however, not the only reaction mechanism that could eject a proton. It turns out, however, that a small set of  $p^9\text{Li}$  coincidences measured in IS367 gives insight into this issue and it indicates that the neutron transfer is indeed the dominant contribution. The following discussion will refer to *singles* as measurement where only the light ejectile was used.

### 13.1 Elastic scattering

The optical potentials can be extracted from elastic scattering and during the experiments, the elastic scattering of both  $d^9\text{Li}$  and  $p^9\text{Li}$  were measured. They can be fitted to the parametrization presented in Section 11.2.

### 13.1.1 Optical model

The first approach to determine the optical potential parameters is a fit of the parametrization describes in Section 11.2 to the experimental data. Since there are many parameters, some are kept fixed to keep the parameters space as small as possible. This approach is in principle the best since it is the same optical potentials required in the CDCC calculation of  ${}^9\text{Li}$ .

Another approach is to use one of the several systematic parametrizations of the optical potential parameters, conveniently compiled in the RIPL database[94]. Many of these are, however, mostly valid at higher beam energies and for heavier systems, but it is worth to try some of these to see how they perform in this energy range.

Since the run conditions at 2.68 MeV/A were similar to the experiment in IS367A[31], the cross sections should, therefore, be comparable.

### 13.1.2 Elastic deuterons

Figure 13.1(A) shows the fit, the two fits, P1 and P2, from [31] as well as a set of parameters from the parametrization DA1p[100]. Table 13.1 contains the corresponding parameters. The agreement seems reasonable with P1. The fitted parameters are close to P1, with a slightly lower  $W_i$ , meaning slightly less strength in the inelastic channels. It is not surprising that they agree rather well due to the relative close beam energies. The DA1p, on the other hand, is far of and can in particular not reproduce the correct position of the minimum.

When the beam energy increases, the structure of  ${}^9\text{Li}$  should not change. In the optical model, this is mainly reflected by the real part of the potential, which dictates the mean-field of the nuclear potential. The loss of flux to other channels should, however, change due to more open channels, which is mainly described by the imaginary surface terms. A simple approximate extrapolation from 2.68 MeV/A to 6.72 MeV/A is thus to free the  $W$  parameter in a fit. The result, M1, is shown in Figure 13.1(B), with  $W_i = 59.05$ . Freeing more parameters give a very similar result. In  $M1$  was  $W_i$  the only free parameter. In  $M2$  was both  $V_r$  and  $W_i$  free, and in  $M3$  were  $V_r$ ,  $a_r$ ,

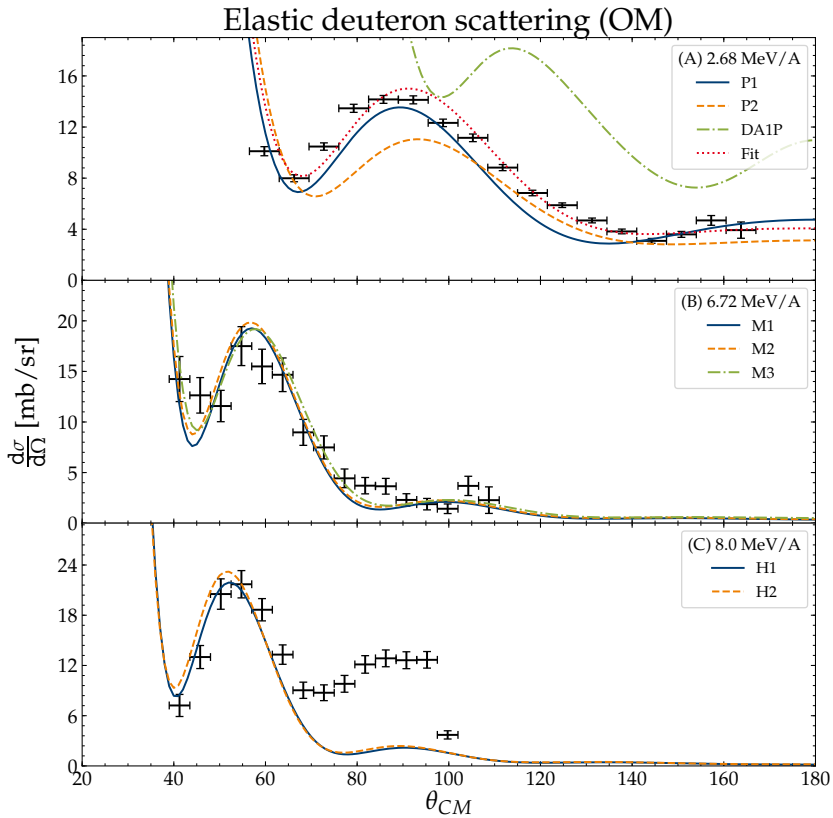


Figure 13.1: The angular cross section for elastic deuterons at three different energies. **(A)** Data for 2.68 MeV/A is shown with different parametrizations of the optical potentials as well as two fits from [31]. The last curve corresponds to a fit to the data. **(B)** The data for 6.72 MeV/A with three fits to the optical potentials. **(C)** The data for 8.0 MeV/A with two fits. H1 is fitted to the full dataset whereas H2 is fitted to the first feature below  $60^\circ$ . The parameters used in the calculations are listed in 13.1.

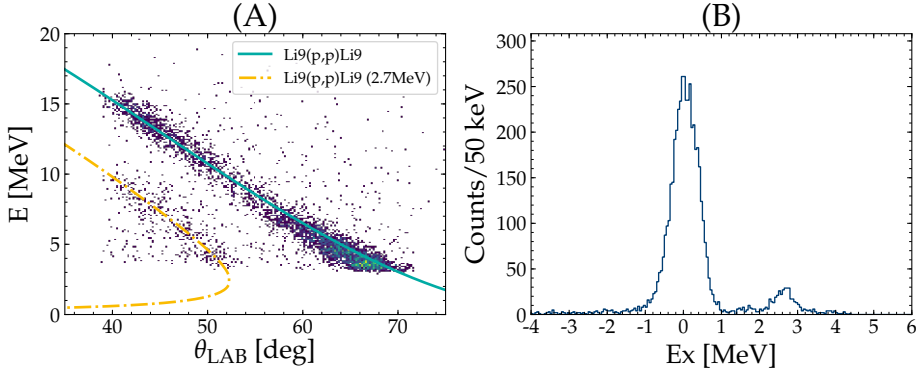


Figure 13.2: Kinematics curve, (A), and excitation spectrum, (B), for  ${}^9\text{Li}(p,p){}^9\text{Li}$  at 8.0 MeV/A.

$W_i$  and  $a_i$  free.

The same exercise for 8.0 MeV/A gives  $H1$  shown in Figure 13.1(C), with  $W_i = 53.4$ . The position of the maximum is nicely reproduced. The amplitude is also nicely reproduced below  $\approx 70^\circ$ .

Above  $70^\circ$  there seems to be extra strength which the optical model can not account for. It was not possible to fit the potential to reproduce this feature by freeing more parameters, and only keeping  $W_i$  free resulted in  $H2$ . This could indicate that there is another component in the data. Looking at the kinematics curve, however, it does not seem to be the case, see Figure 13.2 (A). The kinematic curve, only has contributions from the ground state and the first excited. The corresponding excitation spectrum is shown in (B), and the gate for the angular distribution is  $-1 \text{ MeV} - 1 \text{ MeV}$ . It is thus clear from the elastic reaction. It is not clear why the optical model should perform worse here than at 6.72 MeV/A, and a deeper investigation is left for further analysis.

### 13.1.3 Elastic protons

The same analysis can be carried out for elastic protons, remember they are required for our CDCC calculations. The elastic protons were measured as part of our background measurement. The result is shown in Figure 13.3(A), (B) and (C) for 2.68 MeV/A, 6.72 MeV/A and 8.0 MeV/A respectively.

Three parametrizations has been attempted for 2.68 MeV/A, Powell[101], Watson[102] and Koning/Delaroche (KD)[103]. Neither can, however, reproduce the correct form. The magnitude is not too far off. A fit to the data provides a better reproduction of the data, which can be used in the CDCC calculations.

For 6.72 MeV/A the KD performs rather well and so Watson also provides a rather nice fit. Since KD performs so well, a fit was not pursued.

When the energy is raised to 8.0 MeV/A, however, the two parametrizations underestimates the magnitude significantly. There is, however, a systematic uncertainty from the intensity estimate of 25 %, and the calculations are both within such a large error.

### 13.1.4 CDCC for elastic deuterons

The  $d^9\text{Li}$  scattering can also be performed as a CDCC calculation. This requires, however, both the  $n^9\text{Li}$  and the  $p^9\text{Li}$  interaction. The  $p^9\text{Li}$  optical potential was measured, but the  $n^9\text{Li}$  must be taken from a parametrization. Once again we use the KD and Watson parametrizations, and the parameters are listed in Table 13.2.

The  $pn$  continuum should furthermore be divided into bins and truncated at a suitable maximum energy. To reach convergence, the continuum was truncated at 6 MeV for 2.68 MeV/A and at 10 MeV for 6.72 MeV/A and 8.0 MeV/A. The calculation should also include enough partial waves to converge and up to  $l = 3$  was included.

The  $^9\text{Li}$  groundstate is included with a Reid-Soft-Core[104] implemented in **fresco** by A. M. Moro[92]. It is coupled to each of the bins in the  $pn$  continuum.

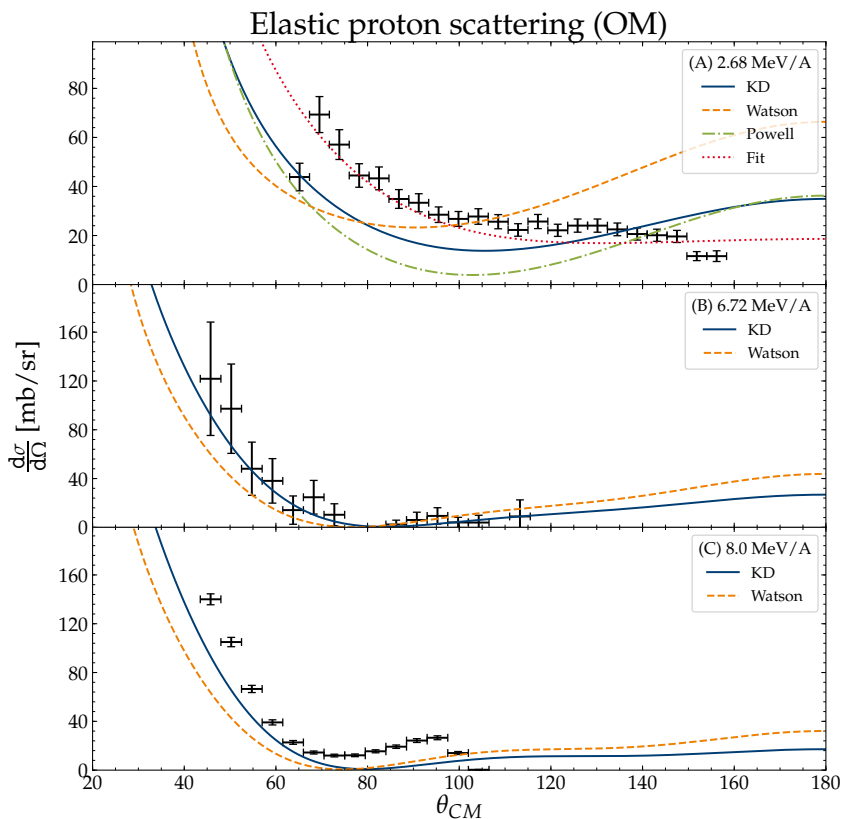


Figure 13.3: The angular differential cross section for elastic protons at three different energies. **(A)** Data for 2.68 MeV/A is shown with different parametrizations of the optical potentials. The last curve corresponds to a fit to the data. **(B)** and **(C)** The data for 6.72 MeV/A and 8.0 MeV/A respectively together with two parametrizations of the optical potentials. The parameters used in the calculations are listed in Table 13.1.

The result of the CDCC calculations with different optical potentials is shown in Figure 13.4 for the three different energies. In the 2.68 MeV/A case, the Watson parametrization is far off. From the elastic protons calculation, Watson was the parametrization furthest from reproducing the shape. If the  $n^9\text{Li}$  interaction have a similar discrepancy, it is not surprising that the CDCC calculation using these optical models are worse. It is, however, noteworthy that it overestimates the magnitude by a large factor. The KD parametrization, on the other hand, does a good job reproducing the shape and magnitude of the data. The first minimum is particularly underestimated.

The fit for the  $p^9\text{Li}$  interaction performs better in this region but at the expense of agreement in the larger angles. Since there are no measurements of the  $n^9\text{Li}$  interaction, it is taken from parametrizations.

For 6.72 MeV/A the Watson parametrizations performs much better, and the KD underestimates by a factor of  $\approx 2$ . It is not clear why this performs worse at higher energies, since it in principle is closer to the proper energy range. The elastic protons seem, however, to be well reproduced by both, which could indicate that the  $n^9\text{Li}$  interaction is not well described.

The same trend continues as we go to 8.0 MeV/A for KD. Watson is now also down by the same factor. In both cases, the  $p^9\text{Li}$  cross sections are underestimated, which may explain why the CDCC calculation underestimates both.

It is worth noting that the shape seems to be reproduced correctly, which could indicate that we are missing some reaction channels such as CN-reactions, that would contribute with a relatively flat background level, and thus an offset to the calculations. This can, however, not be the case at 6.72 MeV/A, since there are almost no cross section at  $100^\circ$ . Moreover, since the background level was low, this would mean that the majority of the CN-contribution should be kinematically similar to elastic scattering, which seems unlikely.

It would in principle be possible to "measure" the  $n^9\text{Li}$  interaction by means of measuring the  $p^9\text{Li}$  and fitting the  $n^9\text{Li}$  part of the potential via a CDCC calculation. The computation time for each iteration of the CDCC calculation is, however, relatively long, making a fit unfeasible for this thesis.

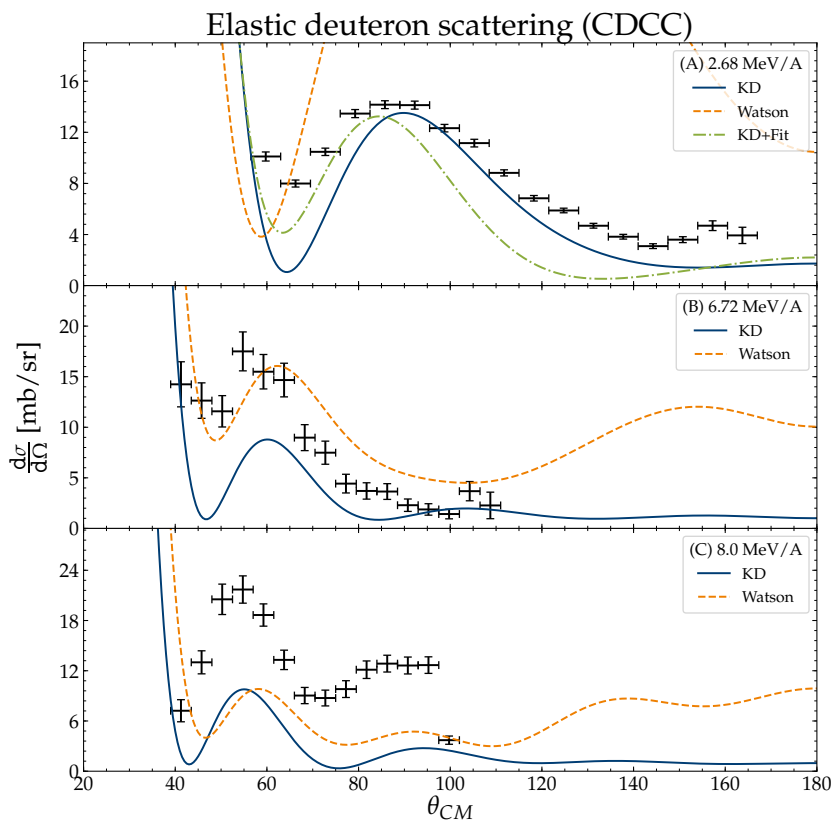


Figure 13.4: The angular cross section for elastic deuterons calculated with CDCC. **(A)** Data for 2.68 MeV/A is shown with two parametrizations of the optical potentials for  $n^9\text{Li}$  and  $p^9\text{Li}$ . The KD+Fit uses the  $p^9\text{Li}$  that was fitted to elastic protons. **(B)** and **(C)** Two parametrizations of the  $n^9\text{Li}$  and  $p^9\text{Li}$  optical potentials.



Table 13.1: Parameters for optical potentials for elastic scattering. Parameters in **bold** were fitted otherwise they were fixed.

	$V_r$	$r_r$	$a_r$	$W_i$	$r_i$	$a_i$	$V_{ls}$	$r_{ls}$	$a_{ls}$
<hr/> <sup>9</sup> Li (d,d) <sup>9</sup> Li <hr/>									
2.68 MeV/A									
P1	<b>104.6</b>	1.2	0.65	<b>12.4</b>	1.2	0.65	6	1.4	0.7
P2	<b>134.6</b>	1.0	<b>0.64</b>	<b>12.2</b>	1.0	<b>0.72</b>	6	1.4	0.7
FIT	<b>104.3</b>	1.2	<b>0.62</b>	<b>10.5</b>	1.2	<b>0.68</b>	6	1.4	0.7
6.72 MeV/A									
M1	104.3	1.2	0.65	<b>59.05</b>	1.2	0.65	6	1.4	0.7
M2	<b>93.04</b>	1.2	0.65	<b>61.85</b>	1.2	0.65	6	1.4	0.7
M3	<b>103.23</b>	1.2	<b>0.61</b>	<b>57.88</b>	1.2	<b>0.63</b>	6	1.4	0.7
8.0 MeV/A									
H1	104.3	1.2	0.62	<b>53.4</b>	1.2	0.68	6	1.4	0.7
H2	104.3	1.2	0.62	<b>58.2</b>	1.2	0.68	6	1.4	0.7
<hr/> <sup>9</sup> Li (p,p) <sup>9</sup> Li <hr/>									
2.68 MeV/A									
Watson	68.86	1.15	0.57	4.86	1.15	0.5	5.5	1.5	0.57
Powell	49	1.25	0.65	7	1.25	0.47	6	1.4	0.7
KD	61.74	1.11	0.68	7.98	1.31	0.52	5.69	0.87	0.59
Fit	<b>62.9</b>	1.2	0.65	<b>13.6</b>	1.2	0.65	6	1.4	0.7
6.72 MeV/A									
Watson	67.77	1.14	0.57	7.19	1.14	0.5	5.5	1.14	0.6
KD	59.95	1.11	0.68	9.68	1.31	0.5	5.6	0.87	0.6
8.0 MeV/A									
Watson	67.42	1.14	0.57	7.94	1.14	0.5	5.5	1.14	0.6
KD	59.38	1.11	0.68	9.98	1.31	0.5	5.6	0.87	0.6

## 13.2 Neutron transfer to $^{10}\text{Li}$

The analysis of the one-neutron transfer is more difficult, since the resulting  $^{10}\text{Li}$  is unbound. Experimentally it is also more challenging. In the experiments it is primarily the ejected proton that was measured. This gives, however, little information about the actual reaction mechanism, as will be discussed later on. Moreover, the acceptance correction is more challenging since it now spans a finite energy range and not a bound state.

### 13.2.1 Acceptance

The correction of the acceptance requires the treatment of the double differential acceptance Eq. (10.9) as described in Section 10.9

$$\frac{d^2\sigma(\theta, \phi, E)}{d\Omega dE} \approx \frac{1}{n_t} \frac{N_S}{N_I} \frac{N_r^d(\theta_i, \phi_i, E_i)}{N_s^d(\theta_i, \phi_i, E_i)} \frac{1}{4\pi E_r}. \quad (13.1)$$

One challenge with the double differential acceptance is the amount of statistics.  $N_r^d(\theta_i, \phi_i, E_i)$  and in particular  $N_s^d(\theta_i, \phi_i, E_i)$  can get quite small, which can lead to large uncertainties. Especially the regions at the edge of the acceptance will have low count numbers. It is, however, enlightening to investigate the acceptance region by plotting the number of detected particles given a uniform distribution, where  $E_r$  is the corresponding available energy in CM. Figure 13.5 shows  $N_s^d(\theta_i, \phi_i, E_i)$  as a function of CM angle and excitation energy and the result for 2.68 MeV/A, 6.72 MeV/A and 8.0 MeV/A respectively.

The first striking feature is the non-trivial shapes. Traditionally theorist is aware and will report the integrated cross section in some region, for instance, angular distributions between 0 MeV-2 MeV. There are, however, a complicated correlation between angle and energy in terms of acceptance.

One way to approach this is to simply gate on a "simple" region. In this case, we would have sufficient coverage and the theoretical calculations can be integrated over some regular regions.

An alternative approach is to use the acceptance to calculate the expected number of counts and then compare this the experimental result. In this

Table 13.2: Parameters for optical potentials for elastic scattering of neutrons. Notice that  $W_i$  is 0.0 in some cases. This reflects the fact that we are extrapolating beyond the parametrization.

	$V_r$	$r_r$	$a_r$	$W_i$	$r_i$	$a_i$	$V_{ls}$	$r_{ls}$	$a_{ls}$
2.68 MeV/A									
Watson	50.86	1.15	0.57	0.0	1.15	0.5	5.5	1.5	0.57
KD	47.13	1.11	0.68	4.64	1.31	0.54	5.63	0.87	0.59
6.72 MeV/A									
Watson	49.77	1.14	0.57	0.53	1.14	0.5	5.5	1.4	0.57
KD	45.74	1.11	0.68	5.1	1.31	0.54	5.54	0.87	0.59
8.0 MeV/A									
Watson	49.42	1.14	0.57	1.28	1.14	0.5	5.5	1.4	0.57
KD	45.30	1.11	0.68	5.16	1.31	0.54	5.51	0.87	0.59

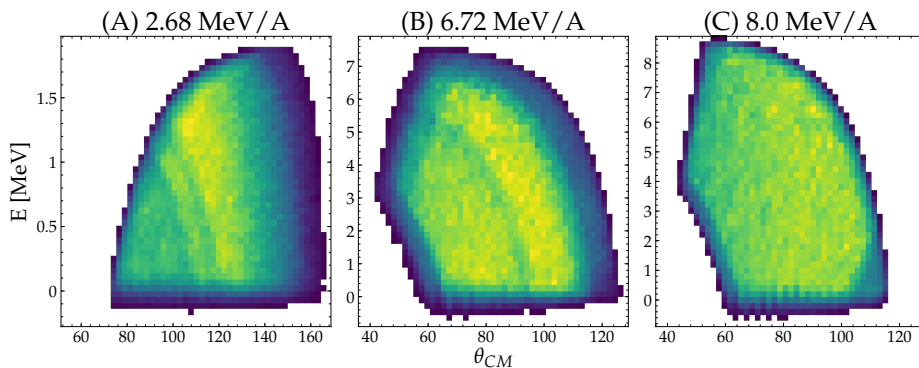


Figure 13.5: Acceptance for  $^9\text{Li}(d,p)^{10}\text{Li}$  at 2.68 MeV/A 6.72 MeV/A and 8.0 MeV/A respectively. Notice lines in the two first panels. They corresponds to dead strips of the detectors.

way the full dataset is used, however, it makes it difficult to compare to other experimental datasets and models that have not been folded with our acceptance.

Consider the case of 2.68 MeV/A, shown in Figure 13.5 (A). The upper left area in the acceptance plot makes it impossible to define a "simple" region that includes all the data. The dataset can be reduced by choosing  $\theta_{\text{CM}} = 90^\circ - 150^\circ$  and  $E = 0 \text{ MeV} - 1.5 \text{ MeV}$  where there is full coverage, and the theoretical projections can be integrated over either  $\theta_{\text{CM}} = 90^\circ - 150^\circ$  or  $E = 0 \text{ MeV} - 1.5 \text{ MeV}$ . This would, however, be at the expense of some data. Extending the region down to  $\theta_{\text{CM}} = 70^\circ$  and project onto the angle axis, there will be missing quite a lot of cross section at low angles due to the vanishing acceptance.

The next step is choosing the bin size. The simplest binning is simply one energy bin to increase the statistics in each of the angular bins. This effectively changes Eq. (10.11) to

$$\frac{d\sigma(\theta, \phi)}{d\Omega} \approx \frac{1}{n_t} \frac{N_S}{N_I} \frac{N_r^d(\theta_i)}{N_s^d(\theta_i)} \frac{\Delta E}{4\pi E_r}, \quad (13.2)$$

where  $\Delta E$  is now the length of the energy interval chosen from the acceptance plot.  $N_r^d(\theta_i)$  is the number of detected particles detected in a given angular bin, summed over all energies in the range.  $N_s^d(\theta_i)$  is the corresponding number of detected simulated particles summed over the energy range.

In the same way, Eq. (10.12) becomes

$$\frac{d\sigma(E)}{dE} \approx \frac{1}{n_t} \frac{N_S}{N_I} \frac{N_r^d(E_i)}{N_s^d(E_i)} \frac{\Delta\Omega}{4\pi E_r}, \quad (13.3)$$

where  $\Omega$  is the solid angle covered in region.

This approximation treats the acceptance across an energy bin as an average. If there is a large variation in acceptance as well as in cross section across the energy bin, this is not a valid approximation. In this case, the more complex version should be used with the statistics problems it may give.

We can now benchmark the two approaches with the data from 2.68 MeV/A given different regions. We consider two angular ranges, a conservative

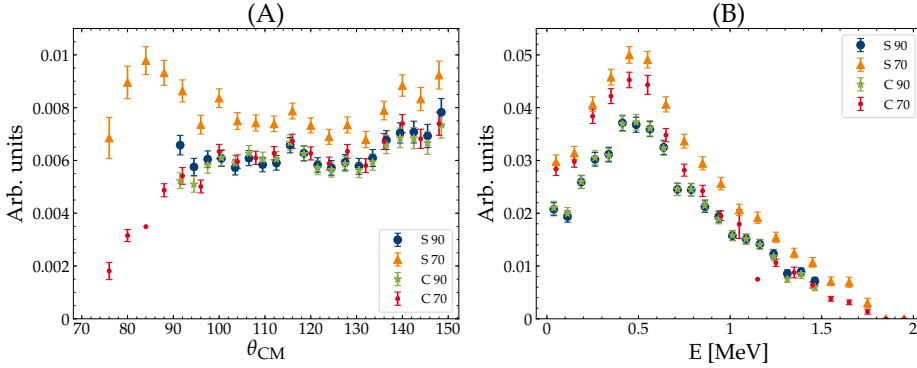


Figure 13.6: **(A)** Differential angular cross sections at 2.68 MeV/A. **(B)** Differential energy cross sections at 2.68 MeV/A. They are corrected for acceptance, but not normalized, hence the arbitrary units.

$\theta_{\text{CM}} = 90^\circ - 150^\circ$  and an opportunistic  $\theta_{\text{CM}} = 70^\circ - 150^\circ$ . In both cases are  $E = 0 \text{ MeV} - 1 \text{ MeV}$ . In the simple (**S**) case we will use 1 bin whereas we will use 15 bins in the complex case (**C**). The result for differential energy cross sections as well as differential angular cross sections are shown in Figure 13.6.

In the conservative case (**S90** and **C90**), both are very similar. When the range increases to the opportunistic case, it starts to include areas that are not covered by the acceptance (**S70** and **C70**) which leads to an overestimation of the cross section. Qualitatively, the angular distributions of **S70** and **C70** are widely different at low angles. This underlines the importance of having a good understanding of the acceptance region.

The exact behaviour depends on the specific acceptance, but we can conclude that if we stay within a safe region we can safely use either method.

### 13.2.2 Calculation

The calculation for the neutron transfer uses the CDCC method and the structure model of  $^{10}\text{Li}$  presented in Chapter 12. To carry out the calculation,

we need the optical potentials for the  $p^9\text{Li}$  interaction. The different sets of parameters presented in the previous calculations have been tried, and I finally ended using the fit for 2.68 MeV/A, and the KD parametrization for 6.72 MeV/A and 8.0 MeV/A. The results are shown together with the data in Figure 13.7, and will be discussed in the following sections.

### 13.2.3 Singles

Based on the acceptance discussion the analysis is limited to  $\theta_{\text{CM}} = 90^\circ - 150^\circ$  and  $E = 0 \text{ MeV} - 1 \text{ MeV}$  for 2.68 MeV/A. The final result is shown in Figure 13.7 (A). There are three observations in the excitation spectrum.

**Evidence of virtual state** Firstly, there is significant strength at the threshold in the excitation plot (right panel). Only a significant contribution from a virtual state can give rise to this. Such a virtual state is one of the major debated questions about the structure of  $^{10}\text{Li}$ . It is clear that these data require a significant contribution from a  $s_{1/2}$  state to reproduce the data. The overall shape of the calculations seems to fit the data nicely, however, the magnitude is off by a factor of  $\approx 2$ . Remember that this spectrum is based on measured protons. There could therefore also be other reaction mechanisms with proton final states, such as deuteron breakup or compound nucleus reactions. We will return to this point when discussing coincidences.

**Splitting of the  $p$ -wave** The second main observation is the shape of the peak. Even though the data give a clear peak just below 0.5 MeV, we can not directly conclude that we need two resonant  $p_{1/2}$  contributions to reproduce it. The resolution of the setup is not good enough to distinguish two close resonant states. This will instead require a more detailed investigation of the model.

**Indications of  $d$ -wave** The energy region of the previous indications for a  $d$ -wave contribution can not be achieved at 2.68 MeV/A, but can at 6.72 MeV/A and 8.0 MeV/A. These two experiments have a few more

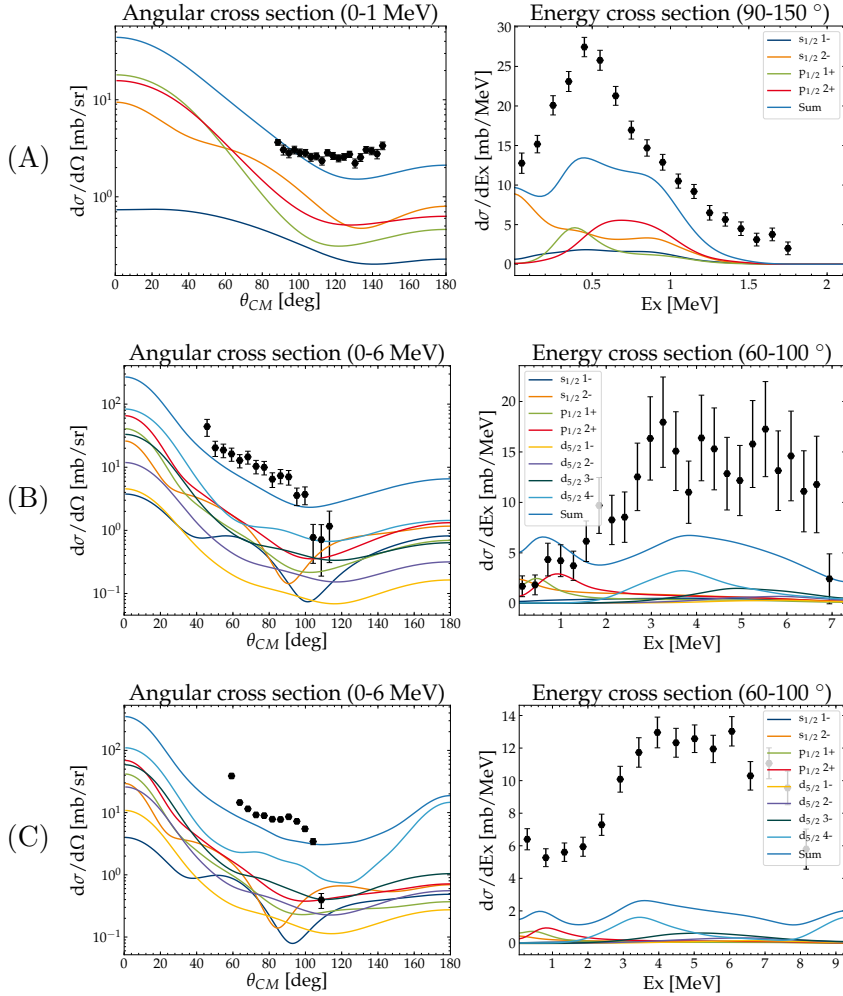


Figure 13.7: (A), (B), and (C) Differential cross for 2.68 MeV/A, 6.72 MeV/A and 8.0 MeV/A, respectively. Left column shows the angular cross section and the right column shows the energy cross section. The title of each panel indicates the integration range in the other variable.

limitations. At 6.72 MeV/A the statistics were limited and at 8.0 MeV/A the intensity estimate remains very uncertain. In both cases, the energy resolution is worse than 2.68 MeV/A, which is mainly an effect of the higher beam energy, giving a larger kinematic compression. This means we can not conclude much about the low energy region (0 MeV-2 MeV).

For 6.72 MeV/A AND 8.0 MeV/A we investigate  $\theta_{\text{CM}} = 65^\circ - 100^\circ$  and  $E = 0 \text{ MeV} - 6 \text{ MeV}$  to stay within acceptance. The results are shown in Figure 13.7 (B) and (C), respectively. The data shows a broad feature above 2 MeV in both cases. For 6.72 MeV/A the shape of the angular distribution seems to match well, but the magnitude is too low. The missing cross section in the model comes mainly from the high energy region, and in particular in the area where we could expect to see the  $d$ -wave resonance. This could indicate the existence of such a resonance, and this is backed by a similar feature at 8.0 MeV/A. The normalization of this data set is, however, rather uncertain, so it is difficult to conclude much from magnitude. Without the measurement of coincidences, it is difficult to determine how much of this belongs to other reactions mechanisms.

### 13.2.4 Slices

We can learn more about the data if we only look at the angle integrated or energy integrated differential cross sections in certain bins. This is essentially an attempt to look at the double differential cross section. We can divide our acceptance region into bins of  $10^\circ$  and calculate the angle integrated cross section. Likewise, can we divide the energy range into bins of 200 keV for 2.68 MeV/A and 1 MeV for 6.72 MeV/A and 8.0 MeV/A and calculate the energy integrated cross sections. The results are shown in Figure 13.8, 13.9 and 13.10 respectively.

**2.68 MeV/A** The main contribution of the strength at 0 MeV comes from the small angles. According to the calculation, this is not surprising, since the  $s_{1/2}(2^-)$  are dominating in this region. At larger angles, the spectra look rather similar, indicating that the different components do not evolve significantly. The angular distribution does not have a lot of structure.



They are all rather flat, contrary to what the model predicts. This indicates that the model is missing something. The flat structure could indicate a significant compound nucleus contribution.

**6.72 MeV/A** The angle integrated cross sections (left column) shows an interesting dip in the  $60^\circ$ - $70^\circ$  bin, clearly indicating some structure. This could be due to the suppression of the  $s$ -waves even though this does not fit with the position from the current calculation. The energy integrated cross sections shows a similar dip in the 3 MeV-4 MeV bin. In general, however, the angular distribution looks more consistent with the model, since all the bins increase as we approach lower angles.

**8.0 MeV/A** The energy integrated bins (right column) looks more structureless. At the higher energy bins, the angular distributions again increase at lower angles, but it does look more flat at low energies. The angle integrated (left column) cross sections looks structurally very similar.

### 13.2.5 Coincidences

The magnitude of the excitation spectrum at 2.68 MeV/A could not be reproduced, and it was suggested that it could be due to the other reaction mechanisms discussed in Section 12. We will explore this by coincident  $p^9\text{Li}$  events. In particular to see to which extent we can understand the contributions from an experimental point of view.

Unfortunately, we only did get a proper measurement of coincidences at 2.68 MeV/A. We look for identified protons that were detected together with one other hit. Assuming that the other hit is a  $^9\text{Li}$ , the missing momentum and energy are calculated and the energy and direction of the neutrons can be deduced. More importantly, however, the correlation between the neutron and the  $^9\text{Li}$  or the neutron and the proton is deduced. We therefore return to the reactions mechanisms discussed in Section 12.3, see Figure 13.11 (A) for a reminder.

Figure 13.11 (B) shows the acceptance corrected spectrum for both singles and coincidences. The coincidences are corrected for acceptance with

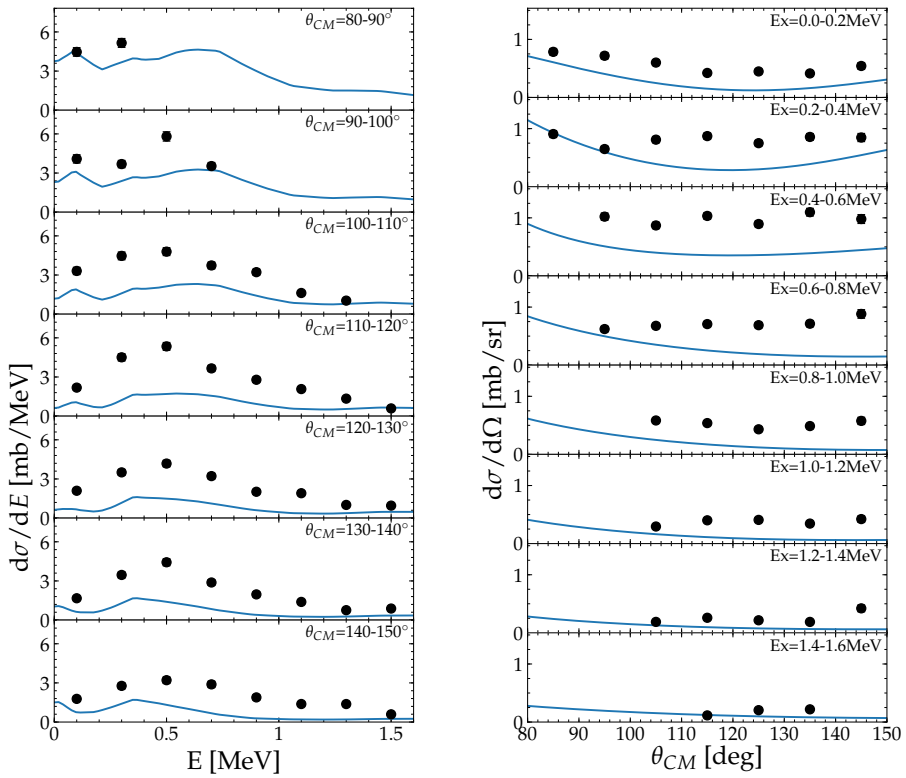


Figure 13.8: Differential cross section for angular (left column) and energy (right column) bins for 2.68 MeV/A.

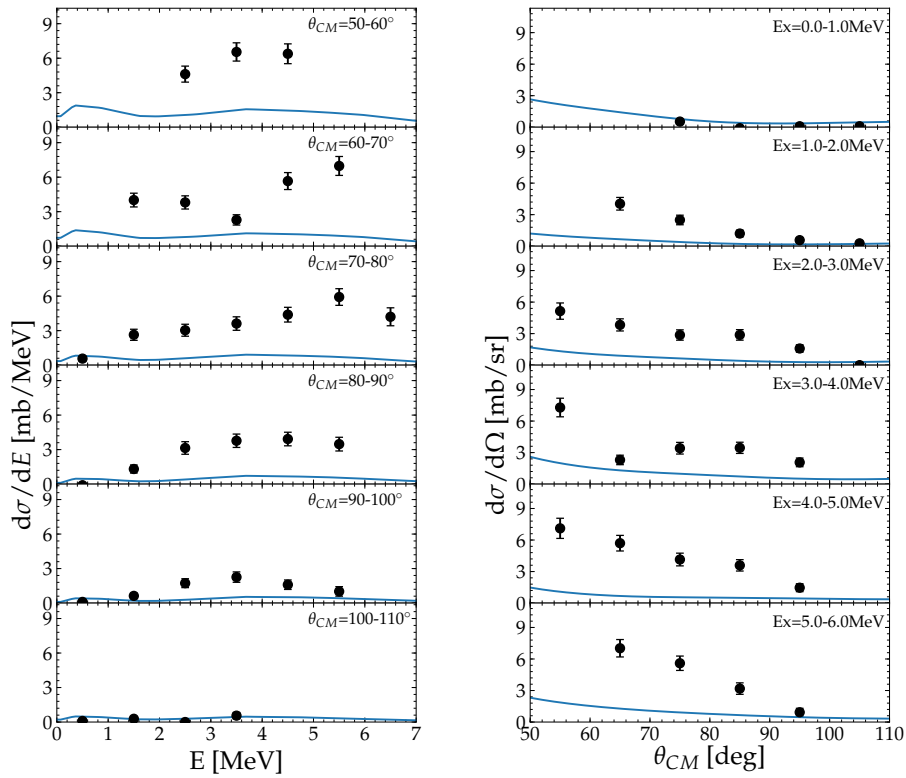


Figure 13.9: Differential cross section for angular (left column) and energy (right column) bins for 6.72 MeV/A.

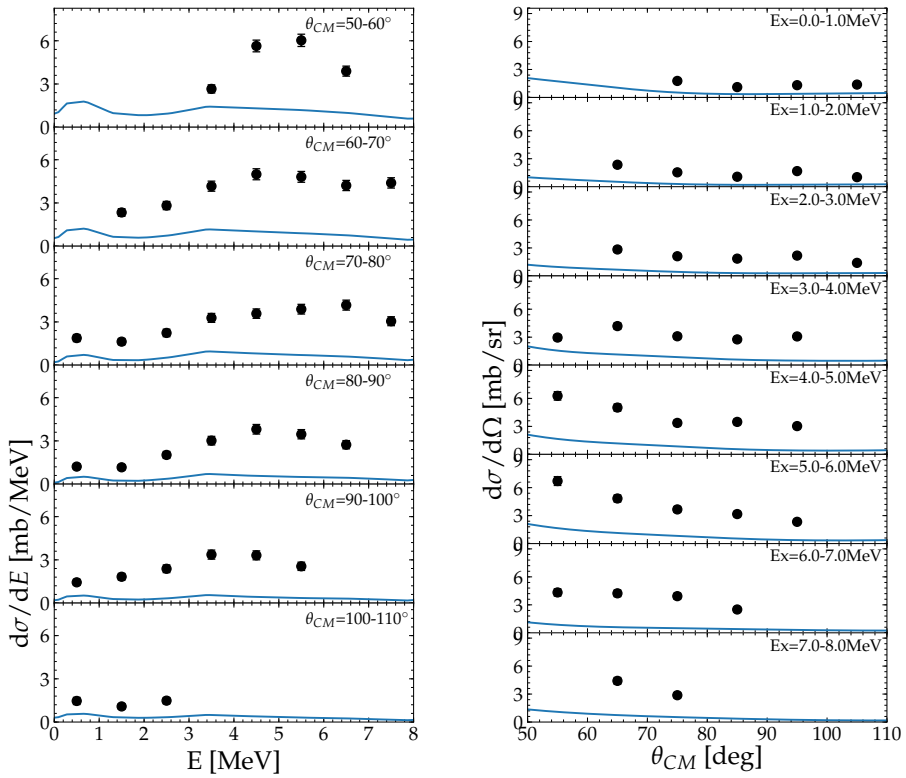


Figure 13.10: Differential cross section for angular (left column) and energy (right column) bins for 8.0 MeV/A.

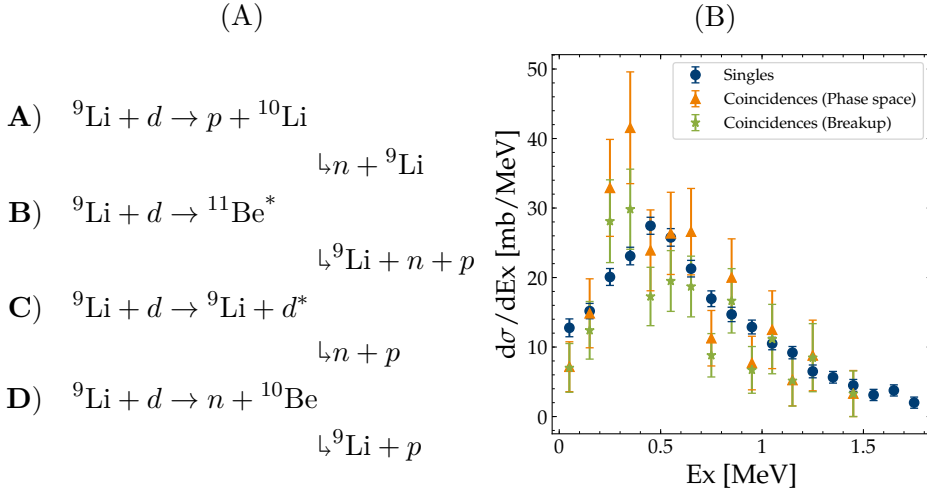


Figure 13.11: **(A)** The different reaction mechanisms discussed in Section 12.3. **(B)** Differential cross section for  $^{10}\text{Li}$  for singles and coincidence measurements are shown in. The singles spectrum is only based on protons. The second dataset (triangles) are coincidences with the acceptance of mechanism **C**. The last dataset (stars) are coincidences but with the acceptance of  $^{10}\text{Li}$  breakup mechanism **A**.

two assumed reaction mechanisms, **B**, and **C**. It should be noted that the acceptance region is the same as for the singles, and the cross sections can, therefore, be compared.

In the case of **A** and **C**, the simulated spectrum is done with two sequential two-body reactions. In the case of **B**, the simulated spectrum is generated with the `TGenPhaseSpace`-class from `ROOT`.

Notice that both magnitude and shape are consistent with each other and with the singles spectrum. This means that the protons observed in the singles spectrum come from the same reaction mechanisms as the ones in the coincidence spectrum. A simulation of **D**, however, showed that the setup can not detect  $p^9\text{Li}$  coincidences with such kinematics. Since there is

no contribution in the coincidence spectrum, there can not be any in the singles either, due to the consistent magnitudes. We can, therefore, rule out **D** (at least within the uncertainties).

To investigate the reaction mechanism further, we can exploit the kinematic differences and therefore the difference in acceptance. We can simulate the three first different situations, uniformly in CM, and analyse the results as



where we detect  ${}^9\text{Li}$  and  $p$  and deduce  $n$ .

The correlation between the deduced neutron as a function of either the proton or  ${}^9\text{Li}$  is shown in Figure 13.12. The first row, corresponding to situation **A**, have a different acceptance region compared to **B** and **C**, which are more similar. In the framework of  ${}^{10}\text{Li}$ , it is easier to think about the proton, since it is ejected opposite in CM (left column). It is striking that the data have the same cut off at  $\approx 100^\circ$  as **A**. Both **B** and **C** does, however, extend to  $\approx 140^\circ$ . To a first approximation, the data is thus mainly compatible with **A**.

The cross section of the deuteron break-up could, however, drop very fast close to  $100^\circ$  for the proton, and thus explain why we do not see it in this correlation plot. It would then still contribute to measurement at lower angles. We do, however, actually have an estimate of this, due to our CDCC calculation of the elastic cross section in Section 13.1. Based on this calculation the cross section does *not* vanish in this region, and we conclude that the deuteron break up have a small contribution.

We can use the same argument for situation **B**. In this case, the angular distribution should be largely flat as the compound nucleus would emit particles with low angular momentum, and we would expect to see a component beyond  $\theta_p > 100^\circ$ , and not a sharp cutoff. Since this is not the case, we also conclude that this mechanism is mostly a small component.

The dominating reaction mechanism for the coincidence measurements is thus **A**, and since both the magnitude and the shape is consistent with

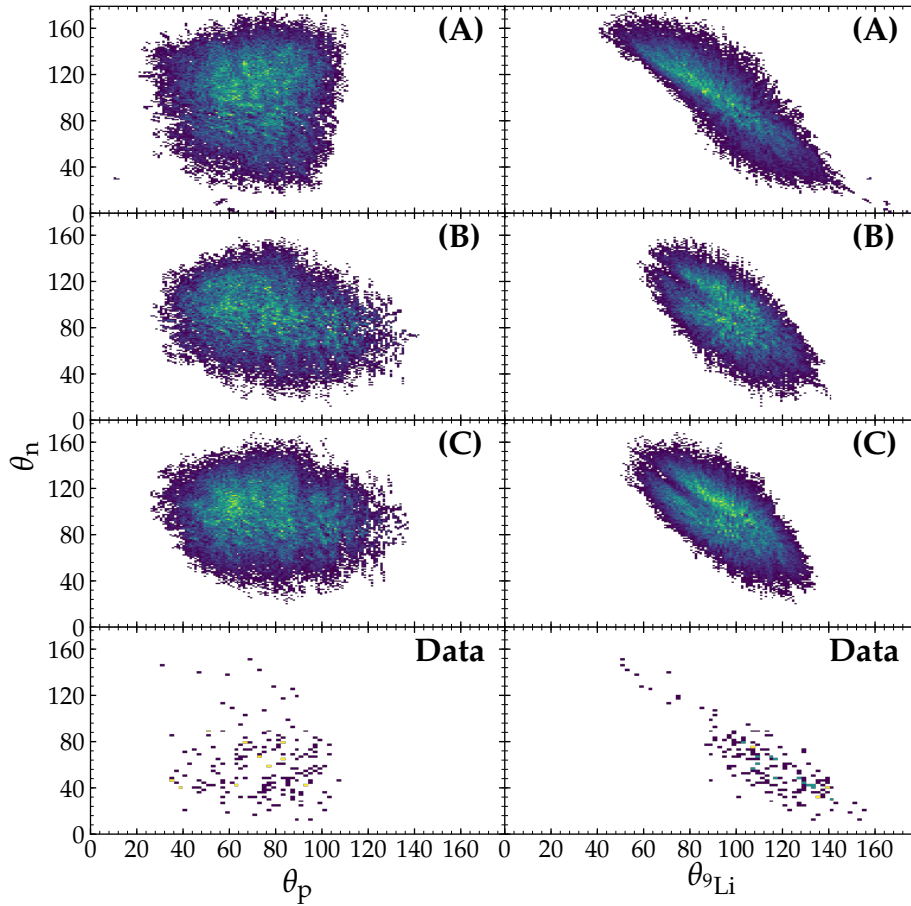


Figure 13.12: Acceptance for angle correlations between the neutron and either the ejected proton or the ejected  $^9\text{Li}$  based on different simulated kinematic situations. The letters correspond to the situations outlined in the text. The left column is the  $\theta_n$  versus  $\theta_p$  and the right columns is  $\theta_n$  versus  $\theta_{^9\text{Li}}$ . All angles are in center of mass.

the singles, we also expect the overall dominating reaction mechanism, in this case, to be **A**.



---

## Summary and outlook

Most nuclear experiment gets us one step closer to a more complete understanding of the complexities of the atomic nucleus. In this thesis, I have presented the result from three different experiments, carried out to study the structure of neutron-rich Li-isotopes, more specifically  $^{10}\text{Li}$ . The experimental method was (d,p) reactions with a  $^9\text{Li}$  beam at 2.68 MeV/A, 6.72 MeV/A and 8.0 MeV/A respectively. The  $^9\text{Li}$  beam was provided by the ISOLDE facility. The experimental results are compared to calculations with the CDCC reaction framework and a novel model for  $^{10}\text{Li}$ .

It is found that the debated *s*-wave contribution is indeed required to explain the data at 2.68 MeV/A. The resonance at 0.5 MeV is nicely described by a *p*-wave contribution. Whether or not there are two resonant *p*-states is still unclear, and therefore also the sequence order. There is extra strength in the region where a *d*-wave contribution has been suggested. This could be an indication for such a contribution, but without coincidences, with  $^9\text{Li}$  it would be very opportunistic to call it evidence.

There is excess strength in the  $^{10}\text{Li}$  excitation spectrum compared to the theoretical predictions. In particular, at 2.68 MeV/A are the data a factor of almost 2 above the calculations. Based on the acceptance of coincidences, however, is it not likely that there are major contributions from other reaction mechanisms. This means that the reaction framework is sound, but the model may be missing some physics.

The attempt to study  $^{11}\text{Li}$  though a (t,p) was unfortunately unsuccessful, but should be attempted in the future. The (t,p) reaction has lower cross sections than the (d,p) and thus requires beam intensities above  $10^6$ pps.

This has been reported by ISOLDE before, but facilities such as Triumph in Canada could also be a candidate. The I in HIE-ISOLDE is *Intensity* meaning that we may hope for higher intensities in the coming years.

Beside the experimental results, the technical challenges of nuclear experiments such as the DAQ and analysis software have also been presented. The data analysis in our group will continuously be based on **ROOT** and **AUSALib**, as it has evolved into a mature and stable library. In the following sections, I will discuss some more concrete insights and possible upgrades for future experiments.

## 14.1 Upgrades to the experimental setup

The experimental setup has undergone developments throughout the experimental campaign. The first setup at low energies could not be done much differently, due to the low energy of backward directions. The new design for the IS561X experiments had both its advantages and its drawbacks.

The highly symmetric coverage at forward angles was essential to understand the beam properties. Having multiple symmetrically placed detectors gave a very good understanding of the beam direction by just looking at the rates. In the subsequent analysis, it was essential to have coverage in the majority of  $\phi = 2\pi$  to constrain the beam parameters.

The position of the downstream detector could, on the other hand, be reevaluated. Given the lack of particle identification, it is most useful for heavy fragments, that are fully stopped. However, due to the kinematic compression, they are ejected close to the beam axis so placing it further downstream would increase our acceptance significantly. The two main practical issues would, however, be the alignment of the beam and setup and Rutherford scattering. A suitable compromise must be found.

It would, however, be desirable to also have particle identification in the downstream. This would require a  $\Delta E - E$  configuration or even a fragment separator.

## 14.2 Better intensity measurements

Elastic scattering is a good tool to calculate the intensity due to the well known Rutherford scattering. However, as the beam energy increases, the grazing angle decreases. Even with a heavy target (Au or Pb) and a relatively light beam, the grazing angle is below  $10^\circ$  at 6 MeV/A. The angular range so close to the beam axis is often not covered, making the intensity estimate difficult.

Besides the decreasing grazing angle, this method does not allow us to measure the intensity while also performing a physics measurement. Instead, we have to resort to the sandwich-method used in IS367.

The best option would be to have a device in the beam dump that could measure the intensity, such as a Faraday cup. However, the intensity of the RIB we use is often too small to be reliably measured with a Faraday Cup, at least quantitatively.

An alternative to the Faraday Cup is an additional reaction site with corresponding detectors within the same experiment.

Consider the setup shown in Figure 14.1. The first four components are identical to the setup used in IS561C, seen from above. We add a second target, a foil of a heavy element just behind the S3 as well as two small silicon detectors downstream. The two additional detectors should be placed below the grazing angle, and be so small that they do not contribute significantly to the DT of the DAQ.

During an experiment, these two detectors will measure elastic scattered beam particles, which follows the Rutherford distribution. If the position and solid angle of these are known, the integrated intensity of the beam can be measured alongside the actual physics experiment. It would also be easy to monitor online, providing a good estimate of the beam intensity.

Having multiple detectors, perhaps four, would provide good consistency checks as well as additional beam diagnostics. The exact position of the additional detectors can be tuned based on the specific beam.

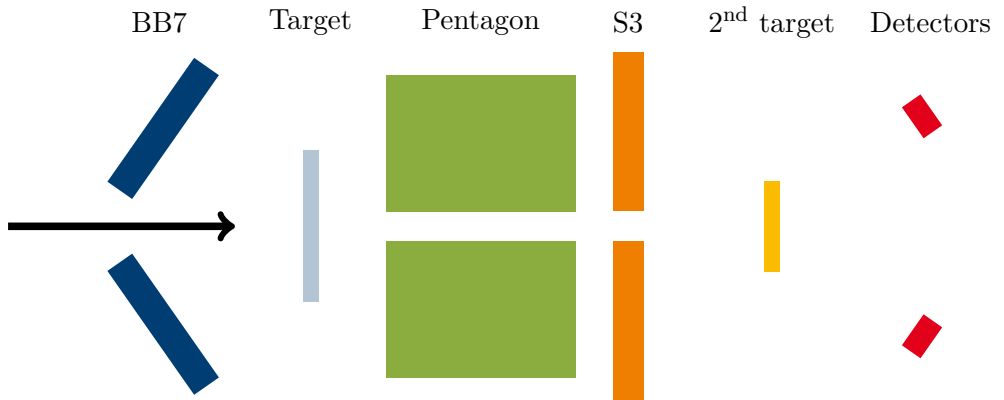


Figure 14.1: Schematics of an additional intensity measurement. The BB7, target, pentagon and S3 are the setup from IS561C. Behind this, an additional measurement setup is placed with a heavy target to measure Rutherford scattering alongside the actual experiment.

### 14.3 Final words

The nuclear chart still contains uncharted territories and probably will for a long time. The future for nuclear research, however, looks bright. The existing RIB facilities are continuously being upgraded and every year we can reach new and more exotic isotopes. I believe, that the currently uncharted aspects of nuclear physics contain great opportunities for technological advancements as well as a better understanding of the quirks of our universe and I look forward to seeing what the future will bring.

---

# Abbreviations

<b>ADC</b>	Analog to Digital Converter
<b>AUSAlib</b>	Aarhus University Subatomic library
<b>AcqC</b>	Acquisition Control
<b>CC</b>	Coupled Channels
<b>CDCC</b>	Continuum Discretized Coupled Channels
<b>CERN</b>	Conseil Européen pour la Recherche Nucléaire
<b>CM</b>	Center-of-Mass
<b>DAQ</b>	Data acquisition
<b>DSSD</b>	Double Sided Silicon Detector
<b>DT</b>	Dead Time
<b>EBIS</b>	Electron Beam Ion Source
<b>FWHM</b>	Full Width at Half Maximum
<b>GPS</b>	General Purpose Separator
<b>GSI</b>	Gesellschaft für Schwerionenforschung
<b>HIE-ISOLDE</b>	High Intensity and Energy ISOLDE
<b>HRS</b>	High Resolution Separator
<b>KD</b>	Koning and Delaroche
<b>LAB</b>	Laboratory
<b>LHS</b>	Left Hand Side
<b>LT</b>	Live Time
<b>MC</b>	Monte Carlo
<b>MS</b>	MASTER START
<b>OM</b>	Optical Model
<b>OP</b>	Optical Potential

<b>RHS</b>	Right Hand Side
<b>RIB</b>	Radioactive Ion Beam
<b>RILIS</b>	Resonance Ionization Laser Ion Source
<b>RSC</b>	Reid-Soft-Core
<b>SBC</b>	Single Board Computer
<b>SEC</b>	Scattering Experiments Chamber
<b>SEMF</b>	Semi-Emperical Mass Formula
<b>TDC</b>	Time to Digital Converter

---

# Bibliography

- [1] G. Aad *et al.* *Physics Letters B* 716 (2012), pp. 1–29. DOI: [10.1016/j.physletb.2012.08.020](https://doi.org/10.1016/j.physletb.2012.08.020).
- [2] S. Chatrchyan *et al.* *Physics Letters B* 716 (2012), pp. 30–61. DOI: <https://doi.org/10.1016/j.physletb.2012.08.021>.
- [3] E. Rutherford. *Philosophical Magazine Series 6* 21 (1911), pp. 669–688. DOI: [10.1080/14786440508637080](https://doi.org/10.1080/14786440508637080).
- [4] J. Chadwick. *Nature* 129 (1932), p. 312. DOI: [10.1038/129312a0](https://doi.org/10.1038/129312a0).
- [5] E. Fermi. *Il Nuovo Cimento (1924-1942)* 11 (1934), p. 1. DOI: [10.1007/BF02959820](https://doi.org/10.1007/BF02959820).
- [6] O. Haxel, H. H. D. Jensen, and H. E. Seuss. *Physical Review* 75 (1949), pp. 1766–1766. DOI: [10.1103/PhysRev.75.1766.2](https://doi.org/10.1103/PhysRev.75.1766.2).
- [7] M. G. Mayer. *Physical Review* 75 (1949), pp. 1969–1970. DOI: [10.1103/PhysRev.75.1969](https://doi.org/10.1103/PhysRev.75.1969).
- [8] A. Ozawa *et al.* *Physical Review Letters* 84 (2000), pp. 5493–5495. DOI: <https://doi.org/10.1103/PhysRevLett.84.5493>.
- [9] E. K. Warburton, J. A. Becker, and B. A. Brown. *Physical Review C* 41 (1990), pp. 1147–1166. DOI: <https://doi.org/10.1103/PhysRevC.41.1147>.
- [10] R. Kruecken (2010). arXiv: [1006.2520](https://arxiv.org/abs/1006.2520).
- [11] Y. Blumenfeld, T. Nilsson, and P. V. Duppen. *Physica Scripta* T152 (2013), p. 14023. DOI: [10.1088/0031-8949/2013/t152/014023](https://doi.org/10.1088/0031-8949/2013/t152/014023).

- [12] A. S. Jensen *et al.* *Reviews of Modern Physics* 76 (2004), pp. 215–261. DOI: [10.1103/RevModPhys.76.215](https://doi.org/10.1103/RevModPhys.76.215).
- [13] B. Jonson. *Physics Reports* 389 (2004), pp. 1–59. DOI: <https://doi.org/10.1016/j.physrep.2003.07.004>.
- [14] M. Wiescher, J. Görres, and H. Schatz. *Journal of Physics G: Nuclear and Particle Physics* 25 (1999), pp. 133–161. DOI: [10.1088/0954-3899/25/6/201](https://doi.org/10.1088/0954-3899/25/6/201).
- [15] O. S. Kirsebom *et al.* *Physical Review C* 84 (2011), p. 049902. DOI: [10.1103/PhysRevC.84.049902](https://doi.org/10.1103/PhysRevC.84.049902).
- [16] I. Tanihata *et al.* *Physical Review Letters* 55 (24 1985), pp. 2676–2679. DOI: [10.1103/PhysRevLett.55.2676](https://doi.org/10.1103/PhysRevLett.55.2676).
- [17] M. Smith *et al.* *Physical Review Letters* 101 (2008), p. 202501. DOI: [10.1103/PhysRevLett.101.202501](https://doi.org/10.1103/PhysRevLett.101.202501).
- [18] N. Shulgina, B. Jonson, and M. Zhukov. *Nuclear Physics A* 825 (2009), pp. 175–199. DOI: [10.1016/J.NUCLPHYSA.2009.04.014](https://doi.org/10.1016/J.NUCLPHYSA.2009.04.014).
- [19] J. H. Kelley *et al.* *Nuclear Physics A* 880 (2012), pp. 88–195. DOI: <http://dx.doi.org/10.1016/j.nuclphysa.2004.09.059>.
- [20] M. J. G. Borge *et al.* *Physical Review C* 55 (1997), R8–R11. DOI: [10.1103/physrevc.55.r8](https://doi.org/10.1103/physrevc.55.r8).
- [21] H. Simon *et al.* *Physical Review Letters* 83 (1999), pp. 496–499. DOI: [10.1103/PhysRevLett.83.496](https://doi.org/10.1103/PhysRevLett.83.496).
- [22] I. Tanihata *et al.* *Physical Review Letters* 100 (2008), pp. 1–5. DOI: [10.1103/PhysRevLett.100.192502](https://doi.org/10.1103/PhysRevLett.100.192502).
- [23] I. Tanihata, H. Savajols, and R. Kanungo. *Progress in Particle and Nuclear Physics* 68 (2013), pp. 215–313. DOI: [10.1016/j.pnpnp.2012.07.001](https://doi.org/10.1016/j.pnpnp.2012.07.001).
- [24] I. Talmi and I. Unna. *Physical Review Letters* 4 (1960), pp. 469–470. DOI: [10.1103/PhysRevLett.4.469](https://doi.org/10.1103/PhysRevLett.4.469).
- [25] D. J. Millener, J. W. Olness, and E. K. Warburton. *Physical Review C* 28 (1983), pp. 497–505. DOI: [10.1103/PhysRevC.28.497](https://doi.org/10.1103/PhysRevC.28.497).



- [26] D. R. Tilley *et al.* *Nuclear Physics A* 745 (2004), pp. 155–362. DOI: [10.1016/j.nuclphysa.2004.09.059](https://doi.org/10.1016/j.nuclphysa.2004.09.059).
- [27] I. J. Thompson and M. Zhukov. *Physical Review C* 49 (1994), pp. 1904–1907. DOI: [10.1103/PhysRevC.49.1904](https://doi.org/10.1103/PhysRevC.49.1904).
- [28] P. Descouvemont. *Nuclear Physics A* 626 (1997), pp. 647–668. DOI: [10.1016/S0375-9474\(97\)00504-6](https://doi.org/10.1016/S0375-9474(97)00504-6).
- [29] M. Zinser *et al.* *Physical Review Letters* 75 (1995), pp. 1719–1722. DOI: [10.1103/PhysRevLett.75.1719](https://doi.org/10.1103/PhysRevLett.75.1719).
- [30] M. Cavallaro *et al.* *Physical Review Letters* 118 (2017), pp. 1–5. DOI: [10.1103/PhysRevLett.118.012701](https://doi.org/10.1103/PhysRevLett.118.012701).
- [31] H. B. Jeppesen *et al.* *Nuclear Physics A* 748 (2005), pp. 374–392. DOI: <https://doi.org/10.1016/j.nuclphysa.2004.11.013>.
- [32] A. M. Moro, J. Casal, and M. Gómez-Ramos. *Physics Letters, Section B: Nuclear, Elementary Particle and High-Energy Physics* 793 (2019), pp. 13–18. DOI: [10.1016/j.physletb.2019.04.015](https://doi.org/10.1016/j.physletb.2019.04.015).
- [33] Y. Aksyutina *et al.* *Physics Letters B* 666 (2008), pp. 430–434. DOI: [10.1016/J.PHYSLETB.2008.07.093](https://doi.org/10.1016/J.PHYSLETB.2008.07.093).
- [34] H. Simon *et al.* *Nuclear Physics A* 791 (2007), pp. 267–302. DOI: [10.1016/j.nuclphysa.2007.04.021](https://doi.org/10.1016/j.nuclphysa.2007.04.021).
- [35] H. B. Jeppesen *et al.* *Physics Letters B* 642 (2006), pp. 449–454. DOI: <https://doi.org/10.1016/j.physletb.2006.09.060>.
- [36] E. Garrido, D. V. Fedorov, and A. S. Jensen. *Nuclear Physics A* 700 (2002), pp. 117–141. DOI: [10.1016/S0375-9474\(01\)01310-0](https://doi.org/10.1016/S0375-9474(01)01310-0).
- [37] F. Barranco *et al.* (2018). arXiv: [arXiv:1812.01761v1](https://arxiv.org/abs/1812.01761v1).
- [38] G. Blanchon *et al.* *Nuclear Physics A* 791 (2007), pp. 303–312. DOI: [10.1016/j.nuclphysa.2007.04.014](https://doi.org/10.1016/j.nuclphysa.2007.04.014).
- [39] K. L. Jones. *Physica Scripta* T152 (2013), p. 014020. DOI: [10.1088/0031-8949/2013/T152/014020](https://doi.org/10.1088/0031-8949/2013/T152/014020).
- [40] W. N. Catford. *The Euroschool on Exotic Beams, Vol. IV*. 2014. Chap. 3, pp. 67–120.

- [41] K. Ieki *et al.* *Physical Review Letters* 70 (1993), pp. 730–733. DOI: [10.1103/PhysRevLett.70.730](https://doi.org/10.1103/PhysRevLett.70.730).
- [42] R. Kanungo *et al.* *Physical Review Letters* 114 (2015), pp. 1–5. DOI: [10.1103/PhysRevLett.114.192502](https://doi.org/10.1103/PhysRevLett.114.192502).
- [43] A. A. Korshennikov *et al.* *Physical Review Letters* 78 (1997), pp. 2317–2320. DOI: [10.1103/PhysRevLett.78.2317](https://doi.org/10.1103/PhysRevLett.78.2317).
- [44] S. Karataglidis *et al.* *Physical Review Letters* 79 (1997), pp. 1447–1450. DOI: [10.1103/PhysRevLett.79.1447](https://doi.org/10.1103/PhysRevLett.79.1447).
- [45] H. B. Jeppesen *et al.* *Physics Letters, Section B: Nuclear, Elementary Particle and High-Energy Physics* 635 (2006), pp. 17–22. DOI: [10.1016/j.physletb.2006.02.034](https://doi.org/10.1016/j.physletb.2006.02.034).
- [46] K. S. Krane. *Introductory nuclear physics*. 1988, pp. 381–385.
- [47] P. E. Hodgson, E. Gadioli, and E. Gadioli Erba. *Introductory Nuclear Physics*. Oxford University Press, 2003. ISBN: 0-19-851897-8.
- [48] L. Schiff. *Quantum Mechanics*. 3rd. New York: McGraw-Hill, 1968.
- [49] *ISOLDE Website*. URL: <http://isolde.web.cern.ch/> (visited on 08/21/2019).
- [50] R. Catherall *et al.* *Journal of Physics G: Nuclear and Particle Physics* 44 (2017), p. 94002. DOI: [10.1088/1361-6471/aa7eba](https://doi.org/10.1088/1361-6471/aa7eba).
- [51] R. Catherall *et al.* *Nuclear Instruments and Methods in Physics Research Section B: Beam Interactions with Materials and Atoms* 317 (2013), pp. 204–207. DOI: [10.1016/J.NIMB.2013.07.030](https://doi.org/10.1016/J.NIMB.2013.07.030).
- [52] Y. Kadi *et al.* *Journal of Physics G: Nuclear and Particle Physics* 44 (2017), p. 084003. DOI: [10.1088/1361-6471/aa78ca](https://doi.org/10.1088/1361-6471/aa78ca).
- [53] W. R. Leo. *Techniques for Nuclear and Particle Physics Experiments: A How-to Approach*. Springer, 1994. ISBN: 3540572805.
- [54] J. G. Johansen *et al.* *Nuclear Instruments and Methods in Physics Research A* 714 (2013), pp. 176–187. DOI: [10.1016/j.nima.2013.02.046](https://doi.org/10.1016/j.nima.2013.02.046).

- [55] M. Munch, J. H. Jensen, and O. S. Kirsebom (2018). DOI: [10.5281/ZENODO.1320121](https://doi.org/10.5281/ZENODO.1320121).
- [56] R. Brun and F. Rademakers. *Nuclear Instruments and Methods in Physics Research A* 389 (1997), pp. 81–86. DOI: [10.1016/S0168-9002\(97\)00048-X](https://doi.org/10.1016/S0168-9002(97)00048-X).
- [57] M. Munch. “A study of 8Be, 12C and 27Al with state-of-the-art detector arrays.” PhD thesis. 2018.
- [58] S. Agostinelli *et al.* *Nuclear Instruments and Methods in Physics Research Section A: Accelerators, Spectrometers, Detectors and Associated Equipment* 506 (2003), pp. 250–303. DOI: [10.1016/S0168-9002\(03\)01368-8](https://doi.org/10.1016/S0168-9002(03)01368-8).
- [59] M. J. Berger *et al.* *Journal of the International Commission on Radiation Units and Measurements* os25 (1993). DOI: [10.1093/jicru/os25.2.Report49](https://doi.org/10.1093/jicru/os25.2.Report49).
- [60] J. Ziegler, M. Ziegler, and J. Biersack. *Nuclear Instruments and Methods in Physics Research B* 268 (2010), pp. 1818–1823. DOI: [10.1016/j.nimb.2010.02.091](https://doi.org/10.1016/j.nimb.2010.02.091).
- [61] H. T. Johansson. *The ucesb unpacker generator*. URL: [http://fy.chalmers.se/~%7B~%7Df96hajo/ucesb/ucesb%7B%5C\\_%7Ddoc.pdf](http://fy.chalmers.se/~%7B~%7Df96hajo/ucesb/ucesb%7B%5C_%7Ddoc.pdf) (visited on 07/04/2017).
- [62] M. Munch and J. H. Jensen. *Calibrator*. URL: <https://git.kern.phys.au.dk/ausa/Calibrator>.
- [63] M. Munch *et al.* *Sorter*. URL: <https://git.kern.phys.au.dk/ausa/Sorter>.
- [64] M. Munch, J. H. Jensen, and O. S. Kirsebom. *Identifier*. URL: <https://git.kern.phys.au.dk/ausa/Identifier>.
- [65] M. Munch *et al.* *IEEE Transactions on Nuclear Science* 66 (2019), pp. 575–584. DOI: [10.1109/TNS.2018.2884979](https://doi.org/10.1109/TNS.2018.2884979).
- [66] M. Munch. “A study of 8Be, 12C and 27Al with state-of-the-art detector arrays.” PhD thesis. 2018.

- [67] J. Hoffman. *VULOM4b data sheet*. 2013.
- [68] H. T. Johansson *et al.* *GSI Scientific Report 2013*. Darmstadt, Germany: GSI, 2014, p. 354. DOI: [10.15120/GR-2014-1-FG-S-FRS-15](https://doi.org/10.15120/GR-2014-1-FG-S-FRS-15).
- [69] *Mod. V785, 16/32 Channel Peak Sensing ADC Technical Information Manual*. CAEN. Feb. 2012.
- [70] *Mesytec ADC data sheet V2.1*. mesytec GmbH & Co. KG. Putzbrunn, Germany.
- [71] *American National Standard for VME64*. Standard. 1994.
- [72] N. Kurz and J. Adamczewski-Musch. *GSI Data Acquisition System MBS Release Notes V6.2*. GSI. Darmstadt, Germany, Apr. 2013.
- [73] H. T. Johansson. *drasi - data acquisition*. 2018. URL: <http://fy.chalmers.se/~f96hajo/drasi/doc/index.html> (visited on 08/12/2019).
- [74] B. Löher *et al.* *GSI Scientific Report 2014*. Darmstadt, Germany: GSI, 2015, p. 192. DOI: [10.15120/GR-2015-1-MU-NUSTAR-NR-08](https://doi.org/10.15120/GR-2015-1-MU-NUSTAR-NR-08).
- [75] *RIO4-8072 User Manual, version 1.0*. CES. Geneva, Switzerland, Nov. 2009.
- [76] G. F. Knoll. *Radiation Detection And Measurement*. 4th ed. Wiley, 2010. ISBN: 9780470131480.
- [77] H. T. Johansson. “The DAQ always runs.” Licentiate Thesis. Chalmers University of Technology, 2006.
- [78] J. Adamczewski *et al.* *IEEE Transactions on Nuclear Science* 51 (2004), pp. 565–570. DOI: [10.1109/TNS.2004.828632](https://doi.org/10.1109/TNS.2004.828632).
- [79] InfluxData. *InfluxDB*. URL: <https://influxdata.com/>.
- [80] Grafana Labs. *Grafana*. URL: <https://grafana.com/>.
- [81] A. Charpy *et al.* *Technical Report for the Design of the NUSTAR Data AcQuisition System*. GSI/FAIR, 2018.
- [82] I. Rusanov *et al.* *GSI Report 2014-1* (2014), p. 374. DOI: [10.15120/GR-2014-1-FG-CS-04](https://doi.org/10.15120/GR-2014-1-FG-CS-04).

- [83] A. Ruben *et al.* *A New, Versatile, High-performance Digital Pulse Processor with Application to Neutron/Gamma-Ray Pulse-Shape Discrimination in Scintillator Detectors*. Tech. rep. 2018.
- [84] *Pixie-16 Data Sheet*. URL: [https://www.xia.com/wp-content/uploads/2018/05/Pixie-16\\_flyer\\_190327.pdf](https://www.xia.com/wp-content/uploads/2018/05/Pixie-16_flyer_190327.pdf).
- [85] S. N. Paneru *et al.* *Physical Review C* 99 (2019), pp. 1–10. DOI: 10.1103/PhysRevC.99.045807. arXiv: arXiv:1902.00417v3.
- [86] P. Bond *et al.* *Physics Letters B* 47 (1973), pp. 231–233. DOI: 10.1016/0370-2693(73)90717-X.
- [87] A. Moro. *Nuclear Reactions - Inelastic, transfer and breakup reactions*. 2018.
- [88] J. G. Camacho and A. M. Moro. *The Euroschool on Exotic Beams, Vol. IV*. 2014. Chap. 2, pp. 39–64.
- [89] I. J. Thompson and F. M. Nunes. *Nuclear Reactions for Astrophysics*. Cambridge University Press, 2009. ISBN: 978-0-521-85635-5.
- [90] P. Capel (2019). arXiv: arXiv:1907.01836v1.
- [91] I. J. Thompson. *Computer Physics Reports* 7 (1988), pp. 167–212. DOI: 10.1016/0167-7977(88)90005-6.
- [92] A. M. Moro. *Private Communications*.
- [93] N. K. Glendenning. *Direct Nuclear Reactions*. Academic Press, Inc., 1983.
- [94] R. Capote *et al.* *Nuclear Data Sheets* 110 (12 2009), pp. 3107–3214. DOI: 10.1016/j.nds.2009.10.004.
- [95] G. H. Rawitscher. *Physical Review C* 9 (1974), pp. 2210–2229. DOI: 10.1103/PhysRevC.9.2210.
- [96] N. Austern *et al.* *Physics Reports* 154 (1987), pp. 125–204. DOI: 10.1016/0370-1573(87)90094-9.
- [97] M. Yahiro *et al.* *Progress of Theoretical Physics Supplement* 89 (1986). DOI: 10.1093/ptpsupp.89.i.

- [98] J. Casal, M. Gómez-Ramos, and A. Moro. *Physics Letters B* 767 (2017), pp. 307–313. DOI: [10.1016/J.PHYSLETB.2017.02.017](https://doi.org/10.1016/J.PHYSLETB.2017.02.017).
- [99] K. Kato, T. Yamada, and K. Ikeda. *Progress of Theoretical Physics* 101 (1999), pp. 119–138. DOI: [10.1143/PTP.101.119](https://doi.org/10.1143/PTP.101.119).
- [100] Y. Zhang, D. Y. Pang, and J. L. Lou. *Physical Review C* 94 (2016), pp. 1–7. DOI: [10.1103/PhysRevC.94.014619](https://doi.org/10.1103/PhysRevC.94.014619).
- [101] D. Powell *et al.* *Nuclear Physics A* 147 (1970), pp. 65–80. DOI: [10.1016/0375-9474\(70\)90510-5](https://doi.org/10.1016/0375-9474(70)90510-5).
- [102] B. A. Watson, P. P. Singh, and R. E. Segel. *Phys. Rev.* 182 (1969), pp. 977–989. DOI: [10.1103/PhysRev.182.977](https://doi.org/10.1103/PhysRev.182.977).
- [103] A. Koning and J. Delaroche. *Nuclear Physics A* 713 (2003), pp. 231–310. DOI: [10.1016/S0375-9474\(02\)01321-0](https://doi.org/10.1016/S0375-9474(02)01321-0).
- [104] R. V. Reid. *Annals of physics* 50 (3 1968), pp. 411–448. DOI: [10.1016/0003-4916\(68\)90126-7](https://doi.org/10.1016/0003-4916(68)90126-7).